SAN FRANCISCO ESTUARY & WATERSHED SCIENCE
Sponsored by the Delta Science Program and the UC Davis John Muir Institute of the Environment

RESEARCH

Erratum to: Evaluation of the Delta Simulation Model-2 in Computing Tidally Driven Flows in the Sacramento-San Joaquin Delta

Vamsi Krishna Sridharan, Stephen G. Monismith, Oliver B. Fringer, Derek A. Fong

Volume 16, Issue 2 | Article 6
https://doi.org/10.15447/sfews.2018v16iss2art6

* Corresponding author: *vamsikrishna.sridharan@ucsc.edu*

We address corrections and criticisms of our manuscript by Drs. Prabhjot Sandhu and Eli Ateljevich at the California Department of Water Resources (CDWR). While our original analysis, inferences, and conclusions do not change significantly, we delve deeper into the model itself and propose several solutions to the model fidelity issues reported in the manuscript as an outcome of these changes. The changes indicate that in most cases DSM2 performs better than we originally reported. We thank Drs. Sandhu and Ateljevich for their comments and Dr. Deanna Sereno at the Contra Costa Water District for guiding us on best data practices.

C1. TIME PERIOD USED TO EVALUATE MODEL PERFORMANCE

CDWR recommended that the summer of 2015 should be used to evaluate the model performance only if challenging circumstances are being highlighted. During 2015, voluntary water withdrawal limitations were in effect and an emergency drought barrier was installed in the Delta that significantly altered tidal behavior in the central Delta. Since the model setup we received from CDWR accounts for the barrier, we did not feel it was necessary to explicitly discuss these special circumstances. However, in the interest of completeness, we acknowledge that the barrier placement and reduced exports were accounted for in the model setup and that the reduced exports add to uncertainty in the modeling of channel depletions and net flow. However, we are justified in evaluating the model performance during this period for two reasons:

i) The extremely low-flow period is a stress-test of model ability to accurately represent the tides.

ii) The altered physical configuration of the Delta tests the ability of the model to reproduce tidal phenomena in a regime that differs from the one in which it was calibrated. The fact that the model needs to be recalibrated when a system change occurs reveals that the model is more phenomenological than mechanistic. We discuss the numerical considerations in DSM2 in Section 5.

C2. MODEL REPRESENTATION

We had incorrectly reported that the bottom friction term in DSM2 is linearized. The correct, nonlinear bottom friction term in the Saint-Vénant equation should be

$$F = -gA\frac{Q|Q|}{K^2} \quad (1)$$

where g is the acceleration due to gravity, A is the channel cross-sectional area, Q is the flow rate, $K = \frac{AR_H^{2/3}}{n}$ is the conveyance, R_H is the hydraulic radius, and n is the Manning's coefficient.

We had also incorrectly noted that when the implicitness parameter is given by $\theta = 1$, the time-marching scheme reverts to the explicit forward Euler time-integration scheme. This should be the implicit backward Euler time-integration scheme.

Based on these errors, we issue the following revisions:

i. the first sentence in *Section 4.1* should read "... quadratic bottom friction ..." instead of "... linearized bottom friction ...",

ii. the paragraph on errors due to the numerical discretization scheme in *Section 6.1* on page 34 should read "... simplifications of the friction term which are common in discretizations of the Saint-Vénant and shallow water equations ..." instead of "... linearization and simplifications in the friction term ...", and

iii. in *Section 6.2*, on page 37, it should read "Incorporating a more accurate friction term ..." instead of "Incorporating a non-linear friction term ..."

C3. BOUNDARY CONDITION RESOLUTION FOR THE STANDARD MODEL SETUP

We had incorrectly reported that the standard configuration in which the DSM2 model is run with a 15-minute time-step size is forced at Martinez with hourly tidal stage from the California Data Exchange Center (CDEC). Instead, the model in its standard configuration is forced with CDWR data over 15-minute intervals at Martinez. For phase-sensitive analysis, CDWR has started recently to recommend that this be the data of record at this station. This data has been recently made publicly available through a data liaison for the Division of Environmental Services (DES) listed on the CDEC web page. In Table 2 in the paper, the boundary condition time-step size should be 15 minutes for the G1T15B1 model configuration. Correspondingly, the resolution condition should be R = 1. In *Section 5.1* on page 20 of the original manuscript, "A possible explanation is that model configurations generally produced the best overall results when R was close to 1." is not the likely explanation to justify the lower aggregate error with the G1T60B1 model configuration. Instead, this is better explained by the fact that the model calibration with a very diffusive value of θ behaves better, as it is more stable, with the larger Courant number condition for the configuration that employs a time-step size of one hour (See Section C5 for additional details).

One of our analyses specifically compared NOAA and CDWR stations at the Martinez Amorco pier. We have revisited our analysis using the QA/QC'd data supplied by CDWR Delta Modeling Section. This data is the same as the DES data cited above, but has received a small amount of screening that affects less than 1% of data points. Comparing data from the two stations shows that the two generally agree reasonably well. Therefore, we acknowledge that the difference between the frequency content in the NOAA data and the CDWR data is smaller than we originally reported, and that much of this difference is contained in the higher than semi-diurnal frequency bands.

Since the model is forced with 15-minute rather than hourly CDEC data at Martinez, the spectrogram of the 15-minute CDEC data (which has been quality controlled by CDWR), as opposed to hourly data as in the original paper is shown in Figure C1.

This figure replaces Figure 5 in the paper. There is still an obvious lack of tidal energy in the CDEC data when compared to the NOAA data that is reflected by a range of 0.1 to 0.7 feet in water level, particularly at frequencies higher than the semidiurnal band. The discrepancy is well above the instrument error and cannot be explained by relative instrument positioning between the NOAA buoy and CDEC data. This indicates that a time-step size of 15 minutes, both in the forcing and in the model, may not adequately resolve higher-frequency mechanisms that drive tidal residual circulation and tidal dispersion.

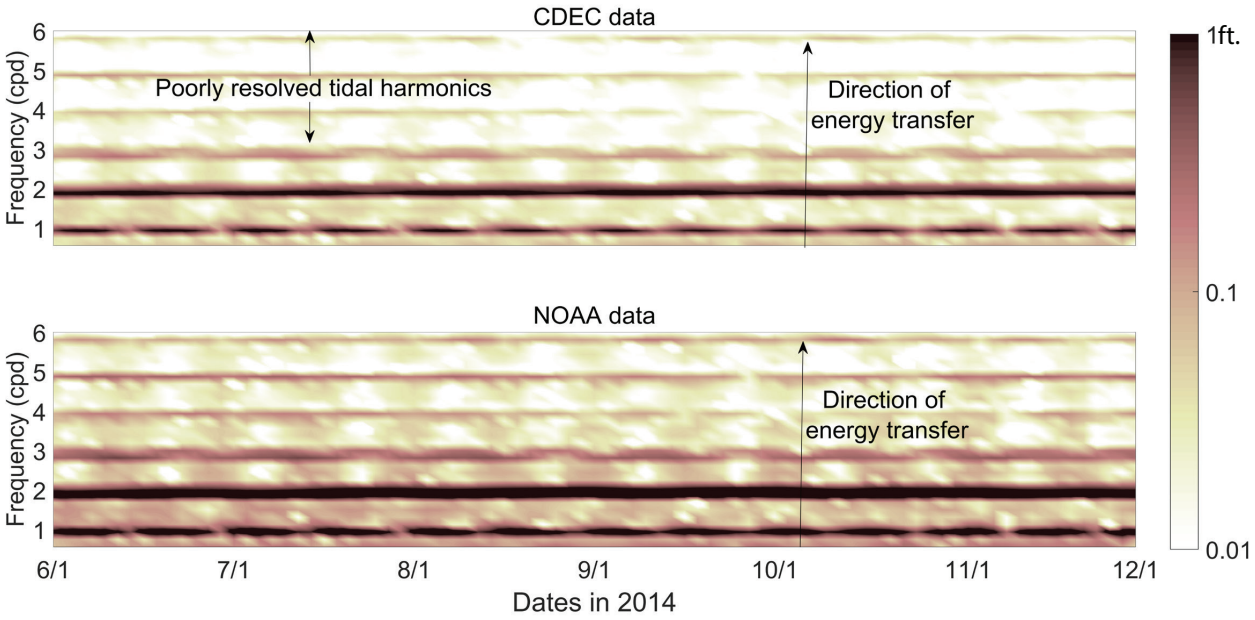

Figure C1 [*Replaces Figure 5*] Spectrograms of the boundary condition time series at Martinez. *Top panel*: 15-minute CDEC data, and *bottom panel*: 6-minute NOAA buoy data. The energy content of various tidal harmonics (equivalent to the contribution of that harmonic to the tide height) is better resolved with the NOAA data set than with the CDEC data set.

Therefore, we recommend that a smaller time-step size be used and that the NOAA data be used to force DSM2's tidal boundary when the model domain ends at Martinez.

C4. TIMESTAMP INCONSISTENCIES

C4.1 Daylight Savings in the CDEC Data

The CDEC stage boundary conditions supplied by CDWR with the DSM2 setup files, as well as the RTC buoy and Amorco Pier NOAA buoy data are all corrected for daylight savings. Therefore, the DSM2 model output is also corrected for daylight savings. However, the data obtained directly from the CDEC website is not corrected for daylight savings. This has been fixed, and new results are presented in Section C4.4. We note that while there are caveats in the CDEC website as to the preliminary nature of the data, there is no documentation indicating daylight savings time is not correctly accounted for in the CDEC data labeled as Pacific Standard Time.

C4.2 Quality Control of Datasets

Based on conversations with Jon Burau of the USGS and Deanna Sereno of the Contra Costa Water District, we discovered that the CDEC data is not quality controlled, i.e., it includes artefacts due to numerical operations on the raw data collected from instruments (discussed below) and does not include censoring of data beyond instrument ranges. Therefore, although it is generally deemed unsuitable for analyzing tidal processes, we performed a very rigorous cleanup of the dataset and subjected our model results to the same filters. Hence, barring the timestamp inconsistency (see Section C4.3), any other data quality issues should not appear in our original analysis. However, to avoid any further confusion, in this corrigendum, we decided to use the original quality controlled data from the USGS (NWIS, 2008) at the stations reported in Table C1.

Stages in the USGS datasets are reported as height above the gauge. At the stations where we do not report the stage, the height of the gauge above the NAVD88 reference datum was unavailable. We estimate the water column depth from the USGS stage data with

https://doi.org/10.15447/sfews.2018v16iss2art6

Table C1 USGS datasets used in the revised tidal effects analysis

USGS Id	CDEC Code	Station	Latitude	Longitude	Data	
11447650	FPT	Sacramento River at Freeport	38.46	−121.50	Flow	Stage
11447890	SDC	Sacramento River above Delta Cross Channel	38.26	−121.52	Flow	Stage
11447905	GES	Sacramento River below Georgiana Slough	38.24	−121.52	Flow	Stage
11455420	SRV	Sacramento River at Rio Vista	38.15	−121.69	Flow	Stage
11447830	SUT	Sutter Slough at Courtland	38.33	−121.58	Flow	Stage
11447850	SSS	Steamboat Slough near Walnut Grove	38.28	−121.59	Flow	Stage
11455165	HWB	Miner Slough at Highway 84 Bridge	38.29	−121.64	Flow	Stage
11455335	DWS	Sacramento Deep Water Shipping channel near Rio Vista	38.26	−121.67	Flow	
11455350	RYI	Cache Slough at Ryer Island	38.21	−121.67	Flow	Stage
11447903	GSS	Georgiana Slough near Sacramento River	38.24	−121.52	Flow	Stage
11336600	DLC	Delta Cross Channel near Walnut Grove1	38.24	−121.51	Flow	Stage
11336930	MOK	Mokelumne River at Andrus Island near Terminous	38.11	−121.57	Flow	
11336680	SMR	South Mokelumne River at New Hope Barrier near Walnut Grove	38.23	−121.49	Flow	Stage
11336790	LPS	Little Potato Slough at Terminous	38.10	−121.50	Flow	
11313433	DSJ	Dutch Slough below Jersey Island Road at Jersey Island	38.01	−121.67	Flow	Stage
11313440	FAL	False River near Oakley2	38.06	−121.67	Flow	
11313452	OSJ	Old River at Frank's Tract near Terminous	38.07	−121.58	Flow	
11313434	ORQ	Old River at Quimby Island near Bethel Island	38.03	−121.57	Flow	
11313431	HOL	Holland Cut near Bethel Island	38.02	−121.59	Flow	
11313405	OBI	Old River at Bacon Island	37.97	−121.57	Flow	Stage
11313315	ORB	Old River near Byron	37.89	−121.57	Flow	Stage
11312968	ODM	Old River near Delta Mendota Canal2	37.81	−121.54	Flow	Stage
11312685	HLT	Middle River near Holt	38.00	−121.52	Flow	
11312676	MDM	Middle River at Middle River	37.94	−121.54	Flow	Stage
11312672	VCU	Victoria Canal near Byron	37.87	−121.54	Flow	
11313240	GLC	Grant Line Canal near Tracy	37.82	−121.55	Flow	Stage
11337190	SJJ	San Joaquin River at Jersey Point	38.05	−121.69	Flow	
11337080	TSL	Three Mile Slough near Rio Vista	38.10	−121.69	Flow	Stage
11313460	PRI	San Joaquin River at Prisoner's Point near Terminous	38.06	−121.56	Flow	
11304810	SJG	San Joaquin River below Garwood Bridge	37.94	−121.33	Flow	Stage
11303500	VNS	San Joaquin River near Vernalis4	37.68	−121.27	Flow	Stage

1 DWR reports that this station was closed in Summer of 2015 and had a flow of near zero.
2 DWR reports that this station was in close proximity to the emergency drought barrier and that the USGS did not rate for its presence.
3 DWR notes that this station is not tidal.

$$d = \text{Gauge depth} + \text{Gauge height above datum} - \text{DSM2 channel bottom elevation} \quad (2)$$

When the gauge depth or gauge height above the datum were reported relative to the NGVD29 datum, we corrected the datum shift using the NOAA orthometric height correction (NGS, 2004). Because of variations in bed depths across the cross-section, this matching of local instrument depths to DSM2 depths provides only a rough placement of the station, accurate to perhaps +/– 4 feet, at locations where the USGS did not directly measure the gage depth but used topographic maps. However, at other stations, the accuracy is +/0.02 feet (personal communication with USGS). This, the uncertainty is of secondary importance when comparing tidal amplitudes.

We have learned that the 15-minute flow data reported by the USGS utilizes the product of a rating curve for the average water velocity as a function of the instrument velocity, and another rating curve for the cross-sectional area as a function of the stage. These rating curves are often quadratic or cubic polynomials and, as a result, are likely to introduce artificial oscillations in flow at the frequencies of the tides and overtides being estimated. This can further complicate the analysis, particularly for nonlinear processes including overtides and residual flow where the signal to noise ratio can be low. We note that this information on how the flow data are reported is not documented clearly, and that model evaluations can only be performed up to the quality of the source data. We also note that we have been careful in the original paper to treat noise in the data conservatively (see Section 4.3 in Appendix A). We urge CDWR to make such information explicitly available to model users.

C4.3 Timestamp Discrepancy in our Analysis

We noticed a timestamp discrepancy in our analysis that was referencing observations from different periods of time than the data to which it was compared. This was causing a significant discrepancy in the paper. For example, in Figure 15 in the paper, we had indicated that in the M_2 component of flow, there was a phase lag between the model and the data at Rio Vista of about 150° corresponding to a time lag of about 4-8 hours. This indicates almost a phase inversion between the model prediction and observations of the M_2 component of the tide. This would also have been evident in the total signal.

In this corrigendum, we correct both the daylight savings and our timestamp assignment error and report the comparisons for the USGS stations in Table C1. While the model fidelity is much better than we had originally reported, there is still a significant error in the amplitudes of the tides and a phase error that increases landward (for instance, the error in both water level and flow increases landward along the Sacramento River in the tidal bands in Tables C2 and C3). We explore the possible reasons for the remaining errors and provide potential solutions in Section C5 below.

C4.4 Revised model evaluation results

Corrections related to the daylight savings inconsistency and timestamp error resulted in changes to the model comparisons in Figures 14 and 15 in the paper and A.6.9 and A.6.10 in Appendix A. We adjust the values reported in these figures in the following tables. We note that we do not expect the summary statistics of the total signals over the entire seven year period we investigated or the subtidal quantities such as the mean flow, Stokes' drift and spring-neap oscillations to deviate from the values we presented in the original paper.

From Tables C2 and C3, we see that the phase error in DSM2 is not as large as we reported in the original paper. However, there is a trend of increasing error in the various tidal constituents as the tide propagates landward. With these new data, there are no significant differences in the errors among the various model configurations, although configurations G1T60B1 and G1T15BB produced the least error over the maximum number of comparisons. These issues are endemic to the model construction, as we discuss in Section C5.

https://doi.org/10.15447/sfews.2018v16iss2art6

Table C2 Difference between measured and modeled harmonic components of water column depth. For each station and harmonic component, the four rows correspond to, respectively, the best performing model, the error in the best performing model, the average error across all models, and the standard deviation in error across all models.

Station‡	Distance inland from Martinez (Km)	K1		M2		MK3		M4	
		Amplitude (%)	Phase (o)	Amplitude (%)	Phase (o)	Amplitude (%)	Phase (o)	Amplitude (%)	Phase (o)
North Delta									
Sacramento River at Rio Vista	48	G2T5B2	G1T15BB	G1T60B1	G1T15BB	G1T60B1	G1T15BB	G1T60B1	G2T5BB
		6.3	−8.1	4.7	−1.4	12.7	5.9	8.7	11.2
		7.9	−2.0	10.1	3.6	23.4	15.2	25.1	26.8
		1.1	3.8	3.7	3.1	4.7	5.9	11.8	9.7
Cache Slough at Ryer Island	55	G2T5B2	G1T15BB	G1T60B1	G1T15BB	G1T60B1	G1T15BB	G1T60B1	G1T15BB
		10.9	−17.2	12.6	−18.7	42.4	−15.4	61.4	−2.8
		12.4	−11.6	19.2	−14.9	63.2	−6.7	115.2	11.9
		1.0	3.5	4.1	2.6	8.7	5.8	25.0	9.6
Steamboat Slough near Walnut Grove	67	G2T5B1	G1T15BB	G1T60B1	G1T15BB	G1T60B1	G1T15BB	G1T60B1	G2T5BB
		8.7	−12.9	4.7	−14.0	3.4	−19.3	12.6	−33.9
		10.7	−6.9	10.6	−10.6	10.2	−11.3	29.3	−18.8
		1.3	3.8	4.4	2.4	3.8	5.4	10.4	9.5
Sacramento River below Georgiana Slough	69	G2T5B1	G1T15BB	G1T60B1	G1T15BB	G1T60B1	G1T15BB	G1T60B1	G2T5BB
		16.0	−14.4	13.4	−13.5	17.9	−16.9	41.6	−30.9
		18.3	−7.8	19.8	−8.4	25.2	−7.8	63.9	−13.4
		1.4	4.1	4.8	3.1	4.1	5.7	13.5	10.8
Sacramento River above Delta Cross Channel	72	G2T5B1	G1T15BB	G2T5B1	G1T15BB	G1T15BB	G1T15BB	G2T5B2	G1T5B2
		13.3	0.1	51.7	13.8	78.0	20.9	159.0	−88.7
		18.7	11.1	71.0	33.5	149.4	37.8	340.2	−41.2
		4.1	7.6	14.8	17.5	71.4	11.8	176.7	50.1
Georgiana Slough near Sacramento River	83	G2T5B1	G1T15BB	G1T60B1	G1T15BB	G1T60B1	G1T15BB	G1T60B1	G2T5BB
		14.7	−15.5	15.3	−15.1	5.4	−18.2	10.3	−32.7
		17.1	−9.1	22.0	−10.2	12.1	−9.3	28.4	−15.5
		1.4	4.0	4.9	3.0	3.6	5.7	11.0	10.5
Delta Cross Channel near Walnut Grove	88	G2T5B1	G1T15BB	G1T60B1	G1T15BB	G1T60B1	G1T15BB	G1T60B1	G2T5BB
		19.6	−4.5	26.9	9.3	24.6	24.8	52.3	23.8
		22.0	3.3	35.9	17.3	33.4	35.4	73.5	47.4
		1.4	4.8	6.3	5.3	4.0	6.4	12.5	15.8
Sacramento River at Freeport	101	G2T5B1	G1T15BB	G1T60B1	G1T15BB	G1T60B1	G1T15BB	G1T60B1	G1T15BB
		12.1	−24.8	−5.9	−36.6	−11.0	−48.9	−13.1	−75.5
		13.7	−17.7	4.7	−32.9	−2.1	−41.6	−8.1	−67.8
		1.5	4.5	7.5	2.7	3.9	5.0	2.1	5.7

Station‡	Distance inland from Martinez (Km)	K1		M2		MK3		M4	
		Amplitude (%)	Phase (o)	Amplitude (%)	Phase (o)	Amplitude (%)	Phase (o)	Amplitude (%)	Phase (o)
South Delta									
Three Mile Slough near Rio Vista	48	G2T5B1	G1T15BB	G1T60B1	G1T15BB	G1T15BB	G2T5BB	G2T5B1	G2T5BB
		6.3	−8.2	2.7	−3.4	23.2	−0.6	11.5	7.2
		8.1	−1.4	6.5	3.0	26.7	9.7	21.6	28.3
		1.1	4.2	3.3	4.2	2.6	6.4	8.0	13.8
Old River at Bacon Island	65	G2T5B1	G1T15BB	G1T60B1	G1T15BB	G1T60B1	G1T15BB	G1T60B1	G1T15BB
		16.0	−18.1	12.3	−21.0	41.4	−26.3	74.6	−15.3
		17.1	−12.0	21.4	−16.3	61.6	−15.8	127.8	−0.3
		0.8	3.8	5.2	3.1	8.4	6.7	30.5	9.2
Middle River at Middle River	83	G2T5B1	G1T15BB	G1T60B1	G1T15BB	G1T60B1	G1T15BB	G2T5B2	G1T15BB
		22.0	−1.2	34.4	14.1	136.0	15.4	555.9	43.1
		23.9	7.1	46.9	25.4	164.3	31.5	707.9	84.4
		1.6	5.3	7.3	8.3	13.5	10.2	129.4	34.2
San Joaquin River below Garwood Bridge	90	G2T5B1	G1T15BB	G1T60B1	G1T15BB	G1T60B1	G1T15BB	G1T60B1	G2T5BB
		17.9	−17.3	10.9	−20.6	27.7	−25.0	22.3	−28.7
		19.0	−11.6	19.3	−16.7	43.5	−15.7	58.3	−13.7
		0.7	3.6	4.8	2.6	6.5	5.9	16.9	9.9
Old River near Delta Mendota Canal	94	G2T5B1	G1T15BB	G2T5B2	G1T15B1	G2T5B1	G2T5B2	G2T5B1	G1T60B1
		−31.7	56.5	−35.3	82.5	264.1	−178.0	474.0	83.5
		−13.1	78.2	25.1	90.2	361.5	76.3	1027.5	113.6
		14.4	14.7	51.9	10.3	77.6	157.1	488.2	25.8
Grant Line Canal near Tracy	106	G1T15BB	G1T15BB	G1T60B1	G1T15BB	G1T60B1	G1T15BB	G1T60B1	G2T5BB
		21.3	−19.9	11.0	−23.6	30.8	−31.9	162.2	−47.3
		22.2	−14.1	21.2	−19.6	56.5	−23.3	329.5	−24.5
		0.7	3.5	4.8	2.6	12.2	6.0	103.8	15.9
San Joaquin River near Vernalis	134	G2T5B2	G1T15BB	G2T5B2	G1T15BB	G1T5B2	G2T5B1	G2T5BB	G2T5B1
		−83.2	38.2	10.7	−149.4	419.6	−154.5	337.2	−90.8
		−16.8	101.7	360.4	−88.1	960.4	−43.2	669.1	−23.0
		84.9	40.4	381.5	42.6	783.1	104.0	205.7	98.6

‡ See footnotes about certain stations in Table 1.

https://doi.org/10.15447/sfews.2018v16iss2art6

Table C3 Difference between measured and modeled harmonic components of flow. For each station and harmonic component, the four rows correspond to, respectively, the best performing model, the error in the best performing model, the average error across all models, and the standard deviation in error across all models.

Station‡	Distance inland from Martinez (Km)	K1		M2		MK3		M4	
		Amplitude (%)	Phase (o)	Amplitude (%)	Phase (o)	Amplitude (%)	Phase (o)	Amplitude (%)	Phase (o)
North Delta									
Sacramento River at Rio Vista	48	G1T60B1	G1T15BB	G1T60B1	G1T15BB	G1T60B1	G1T15BB	G1T60B1	G1T15BB
		-4.3	-8.4	-9.0	-4.9	6.4	-12.0	10.2	-22.0
		-3.1	-2.2	-1.9	0.9	24.0	-1.8	46.1	-4.0
		1.0	3.9	4.1	4.2	7.3	7.5	16.5	12.5
Cache Slough at Ryer Island	55	G2T5B2	G1T15BB	G1T60B1	G1T15BB	G1T60B1	G1T15BB	G1T60B1	G1T15BB
		-6.4	-16.5	-10.6	-13.5	7.5	-24.4	29.5	-29.3
		-5.0	-10.7	-3.7	-8.9	26.4	-14.7	80.2	-14.7
		1.1	3.7	3.6	3.7	7.8	7.3	23.3	10.6
Sacramento Deep Water Shipping channel near Rio Vista	60	G2T5B2	G1T15BB	G1T60B1	G1T15BB	G1T60B1	G2T5BB	G1T60B1	G2T5BB
		-31.3	-14.9	-29.9	-22.1	-14.7	-21.4	-47.9	-13.7
		-29.9	-9.3	-24.8	-17.0	4.0	-9.1	-12.5	4.5
		1.1	3.7	3.1	4.1	7.9	9.6	15.2	15.1
Mokelumne River at Andrus Island near Terminous	60	G2T5B2	G1T15BB	G1T60B1	G1T15BB	G1T60B1	G1T15BB	G1T60B1	G2T5BB
		3.0	-15.6	11.7	-15.5	30.1	-22.8	61.7	-39.4
		5.4	-9.1	19.9	-11.1	41.8	-14.4	86.3	-20.6
		2.1	4.1	6.4	3.4	5.8	6.2	13.0	13.4
Steamboat Slough near Walnut Grove	67	G2T5B2	G1T15BB	G1T60B1	G1T15BB	G1T60B1	G1T15BB	G1T60B1	G1T15BB
		-6.9	-17.3	-7.9	-15.2	4.4	-23.8	29.5	-29.6
		-4.3	-10.2	2.7	-10.3	19.3	-14.7	50.4	-18.4
		2.9	4.5	8.5	3.7	7.4	6.4	11.3	7.8
Sacramento River below Georgiana Slough	69	G2T5B1	G1T15BB	G1T60B1	G1T15BB	G1T60B1	G1T15BB	G1T60B1	G1T15BB
		-3.2	-19.6	0.5	-15.9	8.3	-25.0	18.7	-26.1
		-0.9	-12.2	11.9	-9.8	23.7	-14.6	36.9	-10.8
		1.8	4.7	7.9	4.3	6.8	6.9	8.0	10.1
Little Potato Slough at Terminous	70	G1T60B1	G2T5BB	G1T60B1	G1T15BB	G1T15BB	G2T5BB	G1T60B1	G2T5BB
		-3.0	-9.3	-25.0	-0.2	-60.0	-6.0	-46.7	-16.8
		-2.3	-2.8	-17.0	4.2	-55.7	2.8	-21.0	0.5
		0.3	4.2	3.9	3.8	3.3	8.2	11.2	13.9
Sacramento River above Delta Cross Channel	72	G2T5B1	G1T15BB	G2T5B1	G1T15BB	6	G1T15BB	G2T5B2	G1T15B1
		17.0	-1.8	45.7	22.7	214.4	54.0	361.8	14.4
		22.7	11.1	63.8	43.3	315.9	78.9	1585.3	39.3
		4.3	8.8	12.8	18.3	92.2	18.7	1299.7	24.1
Georgiana Slough near Sacramento River	83	G1T60B1	G1T15BB	G1T60B1	G1T15BB	G1T60B1	G1T15BB	G1T60B1	G1T15BB
		-26.0	-2.4	15.2	-1.2	18.3	-42.0	50.3	-20.1
		-21.3	2.2	35.4	7.5	50.8	-26.8	116.4	-6.2
		2.4	3.2	11.8	6.1	14.5	9.6	35.7	9.5
Delta Cross Channel near Walnut Grove	88	G2T5B1	G1T15BB	G1T60B1	G1T15BB	G1T60B1	G1T15BB	G1T60B1	G1T15BB
		-24.6	-46.7	-22.2	-19.5	42.1	-16.7	93.3	4.7
		-20.3	-37.8	-15.5	-6.5	64.4	0.3	177.9	30.7
		4.4	5.6	5.1	9.3	11.2	11.2	45.4	19.0
Sacramento River at Freeport	101	G2T5B2	G1T15BB	G1T60B1	G1T15BB	G1T60B1	G1T15BB	G1T60B1	G1T15BB
		-9.2	-40.7	-2.7	-47.4	25.6	-58.6	23.6	-77.1
		-6.6	-32.7	13.9	-40.6	55.1	-45.5	71.6	-65.3
		2.0	5.1	11.7	4.7	14.4	8.5	25.5	8.0

Station‡	Distance inland from Martinez (Km)	K1		M2		MK3		M4	
		Amplitude (%)	Phase (o)	Amplitude (%)	Phase (o)	Amplitude (%)	Phase (o)	Amplitude (%)	Phase (o)
South Delta									
San Joaquin River at Jersey Point	43	G2T5B1	G1T15BB	G1T60B1	G1T15BB	G1T60B1	G1T15BB	G1T60B1	G1T15BB
		-10.7	-11.2	-9.8	-9.0	20.4	-13.5	31.9	7.7
		-9.3	-4.6	-2.2	-2.2	38.5	-1.7	73.0	27.7
		0.9	4.2	4.5	4.8	7.5	7.9	20.0	14.2
Three Mile Slough near Rio Vista	48	G2T5B2	G1T15BB	G1T60B1	G1T15BB	G1T60B1	G1T15BB	G1T60B1	G1T15BB
		-9.7	-12.2	-10.9	-4.5	10.1	-3.8	94.5	24.6
		-7.9	-4.7	-3.4	3.5	26.1	10.0	140.1	45.9
		1.1	4.7	4.7	5.7	6.7	8.9	27.3	14.2
Holland Cut near Bethel Island	59	G2T5B1	G1T15BB	G2T5B1	G1T15BB	G1T60B1	G1T15BB	G1T60B1	G1T15BB
		-16.9	-17.3	-3.7	-16.1	-1.6	-18.9	78.6	-37.7
		-12.8	-12.5	5.8	-9.8	21.3	-5.5	138.0	-19.7
		2.4	3.4	6.6	4.6	10.9	9.1	33.8	12.3
Old River at Bacon Island	65	G2T5B1	G1T15BB	G1T60B1	G1T15BB	G1T60B1	G1T15BB	G1T60B1	G1T15BB
		-8.7	-16.5	-11.2	-11.6	5.4	-27.6	173.6	-56.8
		-5.6	-10.6	-1.3	-7.4	28.5	-17.6	328.9	-46.0
		2.2	3.8	5.5	3.5	9.7	7.4	68.9	12.3
Middle River near Holt	73	G2T5B1	G1T15BB	G1T60B1	G1T15B1	G1T60B1	G1T15BB	G1T60B1	G1T15BB
		-83.4	41.2	-77.6	-155.7	-81.7	-52.9	-74.2	40.7
		-82.7	55.3	-59.1	-150.8	-77.8	-43.8	-61.5	69.8
		0.4	11.0	18.4	4.6	1.7	6.6	5.8	20.7
Middle River at Middle River	83	G2T5B1	G1T15BB	G1T60B1	G1T15BB	G1T60B1	G1T15BB	G1T60B1	G1T15BB
		-64.6	-6.5	-59.3	13.5	-41.6	16.4	-14.9	14.2
		-63.3	2.0	-54.8	24.2	-31.2	32.9	57.4	50.3
		1.0	5.6	3.0	8.7	4.3	12.4	41.9	28.1
San Joaquin River below Garwood Bridge	90	G2T5B2	G2T5BB	G1T60B1	G1T15BB	G1T60B1	G1T15BB	G1T60B1	G2T5BB
		-9.6	-15.1	-19.5	-7.0	1.9	-20.7	88.1	15.2
		-6.4	-6.7	-9.3	-2.6	19.6	-11.4	147.5	44.6
		3.1	5.4	8.8	4.0	9.6	7.1	70.8	22.9
Victoria Canal near Byron	93	G1T60B1	G1T15BB	G1T60B1	G1T15BB	G1T60B1	G2T5B2	G1T60B1	G2T5B2
		-35.7	167.2	-31.4	163.2	-11.6	-177.1	39.3	-166.9
		-33.1	174.3	-23.5	165.4	4.5	45.7	81.8	-76.2
		3.7	4.5	5.3	2.6	7.5	182.5	25.4	155.3
Grant Line Canal near Tracy	106	G2T5B1	G1T15BB	G1T60B1	G1T15BB	G1T60B1	G1T15BB	G1T60B1	G2T5BB
		11.9	-7.0	-4.3	-14.4	8.7	-29.5	0.7	-116.2
		18.6	-1.4	7.8	-12.2	25.3	-17.4	24.3	-86.2
		8.8	3.6	10.6	2.8	13.7	9.2	16.2	22.1
San Joaquin River near Vernalis	134	G2T5B2	G1T15B1	G1T5B1	G2T5B2	G1T5B2	G1T15BB	G2T5B2	G1T15BB
		-98.8	-126.4	-27.7	-160.9	-53.1	-104.8	500.6	-71.0
		-87.0	29.8	84.5	-35.9	374.5	-32.3	996.8	-38.1
		19.8	123.6	182.0	87.1	605.8	54.9	523.5	22.5

‡ See footnotes about certain stations in Table 1.

https://doi.org/10.15447/sfews.2018v16iss2art6

C5. DSM2 ERROR ANALYSIS AND RECOMMENDATIONS

Linear stability theory dictates that the FourPt scheme used in DSM2 is unconditionally stable when the implicitness parameter satisfies $\theta \geq 0.5$. Ideally, one would employ a value of $\theta = 0.5$ since this ensures no numerical damping and leads to second-order accuracy in time. However, unless they are damped with $\theta > 0.5$ (DeLong et al., 1997), nonlinear effects lead to high-frequency, spurious oscillations due to the inherent dispersive error of the FourPt scheme. The dispersive error leading to the spurious oscillations is a function of the Courant number

$$C = \frac{c_0 \Delta t}{\Delta x} \tag{3}$$

where Δx is the grid resolution, Δt is the time-step size, and c_0 is the shallow-water wave speed, and the wave resolution factor,

$$\mathrm{WRF} = \mathrm{k} \Delta x \tag{4}$$

where k is the wavenumber of the process of interest. The Courant number can be thought of as a ratio of the time-step size, Δt, to the shortest time scale on the grid, $\Delta x / c_0$, while WRF is the analog to the Courant number in space, since it is a measure of the ratio of the grid resolution, Δx, to the length scale of the process of interest, k^{-1}. Interestingly, the ratio of the time-step size to the time scale of the process of interest, ω_0^{-1}, is given by $\omega_0 \Delta t = C(k \Delta x)$ after noting that the dispersion relation implies $\omega_0 = c_0 k$. Therefore, resolution in time depends both on a small Courant number and WRF. In DSM2, a typical Courant number is $C = 6$ based on a shallow-water wave speed of $c_0 \approx 10\,\mathrm{ms}^{-1}$ (assuming a depth of 10 m), and time-step size of $\Delta t = 15$ minutes $= 900$ s, and a grid resolution of $\Delta x \approx 1500$ m. Depending on the process (discussed below), WRF can range between a small number and the Nyquist limit (the resolution limit of at least two grid cells spanning each wave) or maximum value of WRF = O(1). Despite relatively large values of the Courant number and WRF, which limit accuracy and stability on reach-length waves between junctions, DSM2 is reported to be stable with values of $\theta = 0.50625$ (based on conversations with Drs. Prabhjot Sandhu and Eli Ateljevich). However, there are potential scenarios associated with floods or sudden discontinuities due to man-made structures where instabilities can arise with such low values of θ. As a result, use of large values of the Courant number and WRF lead to spurious oscillations that must be damped with a relatively large value of $\theta = 0.6$ as suggested in DSM2. While stable, this large value leads to excessive damping of the tides as exhibited by the increased error in the tidal constituents moving landward, as indicated in Tables C2 and C3. The need to damp the FourPt scheme with a large value of θ is not surprising given that the unsteadiness associated with the tides is not accurately resolved when the Courant number and WRF are of O(1).

The potential effect of WRF on the dispersive error in DSM2 can be quantified if we consider a typical M_4 tide with period $T = 6.21$ hours propagating with wave speed $c_0 = 10\,\mathrm{ms}^{-1}$. This tide has a wavelength $\lambda = c_0 T = 224$ km and a wavenumber $k = 2\pi/\lambda = 2.8 \times 10^{-5}\,\mathrm{m}^{-1}$, giving WRF $= 0.04 \ll$ (assuming $\Delta x = 1500$ m). Such a small WRF implies that this wave is accurately resolved by DSM2, as it should given that its dynamics are linear and it is long relative to the grid spacing. However, as such waves propagate through the Delta they encounter multiple junctions with length scales of O(10 km), producing waves that are created and destroyed between these junctions, as described by Schwartz (2015) and sketched in Figure C2. These waves have wavelengths of O(10 km), giving WRF ≈ 1, which is close to the Nyquist WRF. The result is that these junction-scale waves are not being resolved in DSM2 and are likely one of the main reasons the model requires a large value of θ to be stabilized. We note that weakly nonlinear effects lead to higher harmonics and short wavelength waves throughout the Delta, and these waves are likely to be propagated with less accuracy than the main tidal constituents. Therefore, we should not expect processes that depend on weakly nonlinear effects, such as tidal residual flows, to be as accurately resolved in DSM2.

Given that errors in DSM2 depend on both the Courant number and WRF, one might expect the results to improve with a decreased time-step size on the same grid. However, tests show no significant

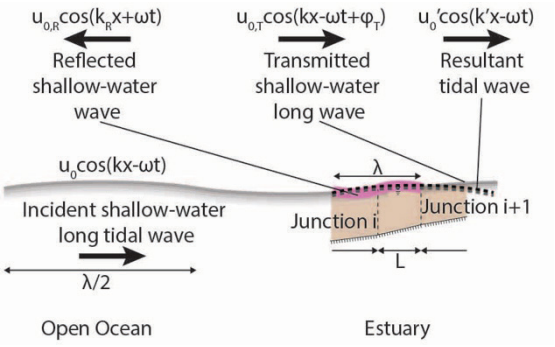

Figure C2 Schematic of the formation of junction-trapped waves due to the different impedances between different reaches of an estuary. The resulting reflected junction-tapped waves typically have wavelengths equal to twice the junction separation and identical phase as the incident wave (Schwartz, 2015).

differences in model results for the phase and amplitude of the M_2 and S_2 constituents with time step sizes of 60 min, 15 min, and 5 min. This suggests that errors associated with the larger reach-scale WRF and $\theta = 0.6$, or associated with other more routine model accuracy limiters (bathymetry and calibration) dominate the solution, preventing it from improving with decreased time-step size. It is important to note that, with decreased time-step size, the temporal resolution of boundary forcing should also increase. One alternative is to use 6-minute NOAA Amorco Pier buoy data.

It would be relatively straightforward to reduce the errors associated with computing the tides in DSM2 simply because these errors depend so heavily on the Courant number and WRF and not on any inherent deficiency associated with DSM2. On the contrary, the FourPt scheme and the other numerical methods in DSM2 are well suited to simulate tidal flows in the Delta. We suggest running DSM2 with a resolution of ~200 m, giving an average junction-scale WRF = $O(0.1)$. The corresponding time step needed to ensure $C = O(0.1)$would require $\Delta t \approx 20\,s$. Incorporating higher resolution would have the additional advantage of necessitating updated, higher-resolution bathymetry. We note that this time and space refinement together represent an increase in the computational burden for DSM2 of roughly two orders of magnitude (45 times as many time steps and 8 times as many grid cells) which may limit its usability on small personal computers. However, DSM2 with this resolution would still represent a significant performance gain over multidimensional models on desktop or parallel computers. Finally, data sources with higher temporal resolution would be needed at the boundaries. Ultimately, higher resolution and a smaller Courant number would then enable use of a smaller implicitness parameter, thus preventing the FourPt scheme from overdamping the tides.

REFERENCES

DeLong LL, Lewis L, Thompson DB, Lee JK. 1997. The computer program FourPt (Version 95.01): A model for simulating one-dimensional, unsteady, open-channel flow. Branch of Information Services: United States Geological Survey. Water-Resources Investigation Report 97-4016. [Internet]. [cited 2018 October 15]; 67 p. Available from: *https://pubs.er.usgs.gov/publication/wri974016*

Hirt CW. 1968. Heuristic stability theory for finite-difference equations. J Comp Phys [Internet]. [cited 2018 October 15];2(4):339-355. Available from: *https://www.sciencedirect.com/science/article/pii/0021999168900417* doi: *https://doi.org/10.1016/0021-9991(68)90041-7*

[NGS] National Geodetic Survey [Internet]. c2004. Silver Spring (MD): VERTCON—North American vertical datum conversion. [updated 2017 May 16; cited 2018 January 25]. Available from: *https://www.ngs.noaa.gov/TOOLS/ Vertcon/vertcon.html*

Schwartz M. 2015. Reflection, transmission and impedence. Harvard University. Lecture notes [Internet]. [cited 2018 October 15]; 10 p. Available from: *http://users.physics.harvard.edu/~schwartz/15cFiles/Lecture9-Impedance.pdf*

[NWIS] National Water Information System [Internet]. C2008. Reston (VA): ISGS surface water data for the nation; [updated 2018 October 15; cited 2018 October 15]. Available from: *https://waterdata.usgs.gov/nwis/sw*

https://doi.org/10.15447/sfews.2018v16iss2art6

AUGUST 2018

SAN FRANCISCO ESTUARY & WATERSHED SCIENCE

Sponsored by the Delta Science Program and the UC Davis John Muir Institute of the Environment

RESEARCH

Evaluation of the Delta Simulation Model-2 in Computing Tidally Driven Flows in the Sacramento–San Joaquin Delta

Vamsi K. Sridharan[1,2], Stephen G. Monimsith[2], Oliver B. Fringer[2], and Derek A. Fong[2]

Volume 16, Issue 2 | Article 6
https://doi.org/10.15447/sfews.2018v16iss2art6

* Corresponding author: *vamsikrishna.sridharan@ucsc.edu*

1 Institute of Marine Sciences
University of California, Santa Cruz,
affiliated with: Fisheries Ecology Division, Southwest Fisheries Science Center, National Marine Fisheries Service, National Oceanic and Atmospheric Administration
Santa Cruz, CA 95060 USA

2 Environmental Fluid Mechanics Laboratory,
Department of Civil and Environmental Engineering
Stanford University
Stanford, CA 94305 USA

ABSTRACT

We investigate the fidelity of the Delta Simulation Model-2 (DSM2), a one-dimensional branched network hydrodynamics solver, which is used to model water quality and ecology in the Sacramento–San Joaquin Delta estuary. We find that while DSM2 reproduces the total flows well, it does not accurately represent the harmonic components of the tides and tidal modulation of subtidal flow. The inaccurate representation of tidal dynamics affects prediction of subtidal flows, flow splits at key junctions, and salinity. These deviations are the result of coarse spatial and temporal representation of tides as well as unrepresented estuarine physical processes. We propose and evaluate two types of schemes intended to improve fidelity: modifying the model domain and specifying fine grid and boundary conditions, and incorporating and parameterizing more complex physical processes into the 1-D model. We also develop a comprehensive protocol to evaluate the model in which we assess the fidelity of model results. In this protocol, we also include a decomposition of the model error into a systematic component because of model representation, and an unsystematic component, which includes errors from both unmodeled physical processes and data precision. Our analysis reveals that these recommendations would be effective provided they can be incorporated with model recalibration. Both our proposed schemes and the model evaluation process will be useful in analyzing models of networked surface water systems such as the Delta in which the distribution of observations is spatially inhomogeneous.

KEY WORDS

Tides, estuarine dynamics, shallow water wave equations, numerical modeling, Delta Simulation Model II, DSM2, error analysis, model performance evaluation, San Francisco Bay–Delta.

1. INTRODUCTION

The success of water management and ecosystem restoration efforts in the Sacramento–San Joaquin Delta (hereafter, the Delta) depend on correctly understanding the system-scale scalar transport and fate dynamics (Cloern 2007). Often, this understanding is gained through the use of numerical models. The California Department of Water Resources' (CDWR) one-dimensional (1-D) Delta Simulation Model II (DSM2)—the primary hydrodynamic model used for planning and management purposes in the Delta (e.g, Liang et al. 2011; Rose et al. 2013; Tu 2012; Smith 2014)—predominantly reproduces only instantaneous total flows and water levels with high accuracy (see Sridharan 2015). However, it does not represent four aspects of the tidal dynamics of the system well (see the Appendix A for a description of the terms used herein): (1) the *subtidal* or riverine component of the flow; (2) *astronomical tidal harmonic components* (such as K_1, M_2, etc.) as well as *overtides* (e.g, M_4) and *compound tides* (e.g, MK_3) (Nidzieko 2010); (3) *modulation of the subtidal flows* by tides (MacCready 1999), and (4) variability in the water column depths and flows over the fortnightly *spring–neap* lunar cycle (Monismith 2016). (Hereafter, we refer to (1)–(4) collectively as *tidal effects*). Inaccurate representation of the tidal effects affects the fidelity of the model solution. This limitation in representing the tidal effects, previously unreported in both the DSM2 methods literature (e.g, CH2MHill 2009), as well as the applications literature (e.g., Kimmerer and Nobriga 2008; Perry et al. 2015), may have significant implications for water management in the Delta.

In this paper, we evaluate DSM2's hydrodynamic and water quality solvers, so that appropriate inferences may be drawn from its results. Specifically, we investigated its reproduction of (1) instantaneous hydrodynamic and water quality fields, (2) tidal effects, and (3) key regulatory flow parameters. The latter is important because Delta water managers routinely use DSM2 as a decision support tool (Fleenor and Bombardelli 2013).

To perform this investigation, we developed a comprehensive model-evaluation protocol in which we incorporated (1) robust aggregate metrics of overall performance; (2) a decomposition of the spatially localized Root Mean Squared (RMS) errors between model results and observations into *systematic* or model representation-induced components (biases), and *unsystematic* (rather than non-systematic or purely random noise [Taylor 1997]) or unmodeled physical processes-induced components (biases) and data precision errors (random noise) (Willmott 1981); and (3) succinct target diagrams (Jolliff et al. 2009) and field difference maps between observed and modeled quantities that describe spatial and temporal trends.

Given the continued utility of simple 1-D models (e.g., Savenije 2005; Savenije et al. 2008), maximizing the likely accuracy of models such as *DSM2* is worthwhile. To this end, we proposed a suite of improvements based on a review of the literature on more complex as well as better-performing models, and evaluated these improvements using the protocol we described above. The first set of these recommendations improve model fidelity; the second set are useful for informing management actions. These recommendations, which we implemented without recalibrating the model, significantly improved the model's error response characteristics. This indicates that with proper recalibration, these recommendations would improve the fidelity of the model, as well. We briefly describe these recommendations below.

First, it is good modeling practice to meet a Courant–Freidrichs–Lewy (CFL) condition of about 1 (Ferziger and Perić 1997), and to match the temporal resolution of the tidal boundary conditions and the model time-step size (hereafter, the *resolution criterion, R*) (Sobey 2001; Fringer et al. 2006). For information propagating at speed u in a time-step of size Δt through a grid of resolution Δx from a boundary condition with resolution Δt_{BC}, these conditions are

$$CFL = \frac{u\Delta t}{\Delta x} \leq 1$$
$$R = \frac{\Delta t_{BC}}{\Delta t} \approx 1 \quad (1)$$

In the Delta, as a typical tidal wave propagates at a speed of $c \approx \sqrt{gH} \approx 10 ms^{-1}$ (for a typical water column depth of 10 m; e.g., see Kundu and Cohen 2002), and in 15 minutes, the typical time-step size

in DSM2, it moves about 10 km inland, a significant portion of the Delta. Therefore, a smaller model time-step size is required to resolve the tide adequately.

Second, the addition of an idealized representation of San Francisco Bay (hereafter, the Bay) to allow tidal information to radiate past Martinez is advisable in systems such as the Delta (Sobey 2001). An idealized Bay would also be expected to allow the model to respond to spring–neap oscillations in the sea-level of the coastal ocean more accurately, particularly when the model is being used as a forecasting tool. We also propose some ad hoc parameterizations to represent unmodeled physical processes: viz, flows in shoal–channel systems and intertidal mudflats, and wind- and density-driven flows. Finally, we also propose simple modifications in the numerical approximations in the model. These recommendations, as well as the model evaluation protocol, would be useful for evaluating and improving 1-D models in general.

This paper is organized as follows: in Section 2, we describe the Delta and its hydrology; in Section 3, we provide a brief overview of estuarine hydrodynamics; in Section 4, we describe the DSM2 model and outline the scope of our evaluation of the model; in Sections 5 through 7, we present the results, synthesize them, and report findings that apply to future applications of this model as well as to other 1-D shallow-water models.

2. SACRAMENTO–SAN JOAQUIN DELTA

The Delta is a critical component of water management for agriculture, fisheries, ecosystems, transport, industry, and recreation in California. Historic land use patterns and water operations have resulted in the ongoing advection of sediment and dissolution of various compounds in the Delta (Barnard et al. 2013). It features diverse ecosystems (Lucas et al. 2002) that are home to several native as well as invasive species (Feyrer and Healey 2003). More urgently, aging infrastructure in the Central Valley (Mount and Twiss 2005) and rising sea levels resulting from climate change (Barnard et al. 2013) are serious concerns. The combination of these hydrological, ecological, and social factors has made this one of the most extensively studied surface water systems in the world.

2.1 Delta Geography and Morphology

The Delta is an inverted fan estuary at the confluence of the predominantly rain-fed Sacramento River and the snowmelt-fed San Joaquin River, and smaller rivers such as the Mokelumne in the east (Fleenor et al. 2010) (Figure 1). The Delta converges at Martinez in the Carquinez Strait, which links to the Bay and then the Pacific Ocean via the mouth of the estuary at the Golden Gate. The average daily river flow ranges from about 150–2,200 m^3s^{-1}. While flows in both the Sacramento and San Joaquin rivers are heavily regulated, the Sacramento River contributes almost 90% of the inflow to the Delta (Kimmerer 2004). The tides are semi-diurnal in nature (Monsen 2000) with a net tidal flow at Martinez of about 5,000–13,000 m^3s^{-1} and a mean tidal range of 1.8 m (Kimmerer 2004). Both the tidal signal and subtidal transport attenuate rapidly eastward into the Delta (Monsen 2000; Sridharan 2015).

The Delta is morphologically complex, with numerous shallow and wide channels (Monismith et al. 2009) and leveed and submerged islands (Monsen 2000), and confluences at its oceanward end into a shallow embayment (Suisun Bay), which is bordered by an intertidal brackish wetland (Suisun Marsh). In the northwest, the Yolo Bypass floodplain is maintained to divert water from the Sacramento River when it floods and overtops a series of weirs upstream of the Delta (Sommer et al. 2011). The Sacramento River bifurcates into its mainstem, and three sloughs—Sutter, Steamboat, and Georgiana—in the North Delta. The San Joaquin River bifurcates into its mainstem and the Old and Middle rivers (OMR) in the South Delta (Figure 1). The Old and Middle rivers are linked by a series of canals that divert water to the pumps (Figure 1). This region is known as the OMR corridor (Fleenor et al. 2010).

Flow, sediment, salt, and biota are channeled through several critical flow-course junctions. Various species of endangered fish migrate through these junctions via different routes; rigorous quantitative evidence is available through numerous studies of the migration patterns of Chinook salmon (e.g., Perry et al. 2010; Newman and Brandes 2010; Buchanan et al. 2013; Perry et al. 2013). These include the bifurcation of the Old River from the San Joaquin River near Mossdale (Brandes and McLain 2000),

https://doi.org/10.15447/sfews.2018v16iss2art6

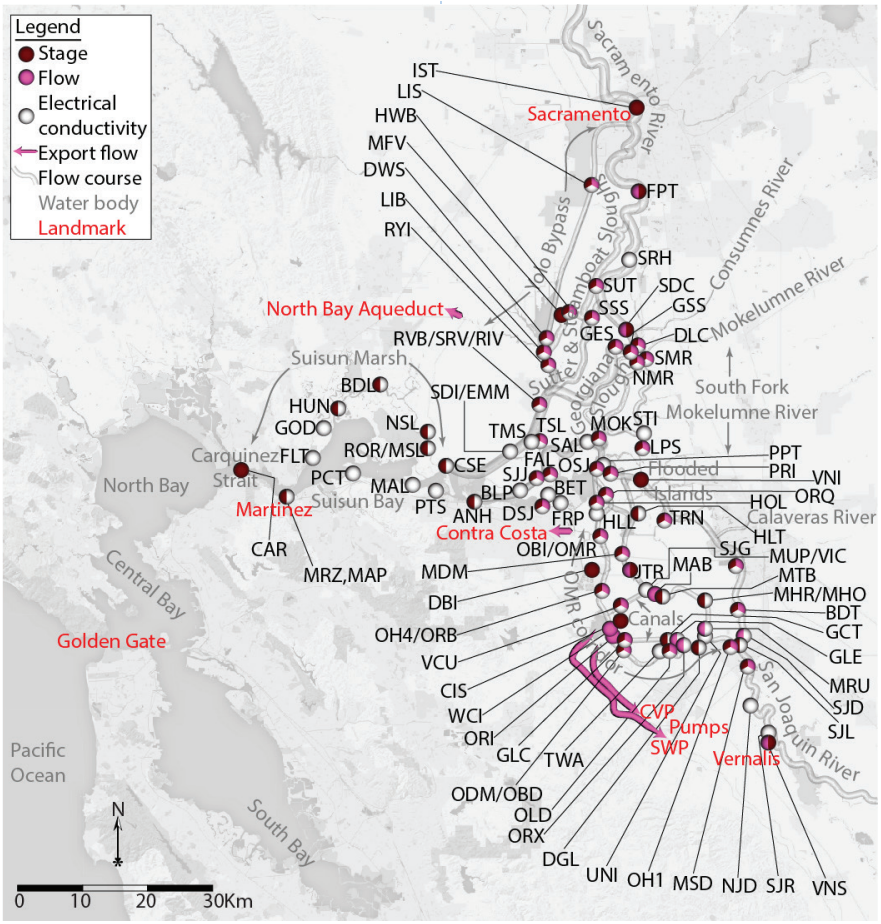

Figure 1 The Sacramento–San Joaquin Delta study site. The locations where we obtained data from the CDEC data base are indicated by filled pies in which different colors correspond to the types of data that is available. Rivers, flow courses, geographic regions, boundary conditions, and important landmarks are indicated.

and the bifurcations of the Sutter, Steamboat, and Georgiana sloughs from the Sacramento River (Perry et al. 2013). Moreover, the phasing of the tides between the Sacramento River and the San Joaquin River at Threemile Slough has implications for the local transfer of sediments between the two rivers (Wright and Schoellhammer 2005), as well as system-scale scalar transport (Sridharan 2015). This relative phasing of the tides also governs the tide-phase-dependent migration patterns of the endangered Delta Smelt (Bennett and Burau 2015).

Water is managed within the Delta through (1) the Delta Cross Channel (DCC), which is opened to supply freshwater from the Sacramento River to the South Delta; (2) the Central Valley Project (CVP) and State Water Project (SWP) export pumps in the South Delta, and, at much lower levels, the Contra Costa Water District (CCWD c2018) and North Bay Aqueduct (SCWA c2018) exports, which supply drinking water to parts of central and northern California; and (3) a gate system, which is operated to prevent salinity intrusion into Suisun Marsh (Monsen 2000) (Figure 2). Several temporary barriers are also erected at various locations in the Delta to aid salmon passage (at the head of Old River) and to maintain water levels to facilitate agricultural diversions (Monsen 2000; Kimmerer 2004; Monsen et al. 2007; Kimmerer 2008) (Figure 2). In addition, there are nearly 2,000 uncharted private water withdrawals, which are not well quantified (Figure 2). These operations significantly alter the flow patterns in the Delta.

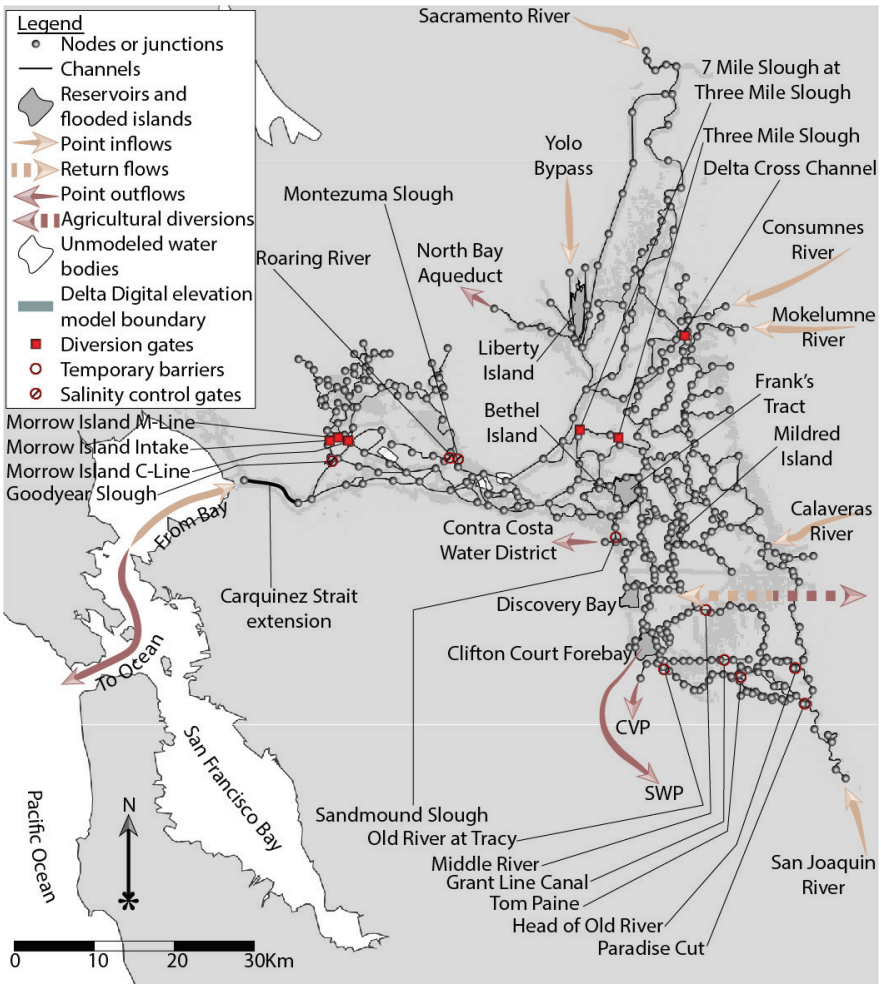

Figure 2 The DSM2 grid. For clarity, in this map we show 1-D DSM2 channels that follow the true centerlines of the flow courses. We indicate the Carquinez Strait extension by a heavy line. The actual channels in DSM2 are straight links between nodes with a sinuosity factor to account for the true lengths of the flow courses (BDO c2002). The agricultural diversions and return flows into the system are distributed over all the DSM2 nodes.

2.2 Delta Hydrology, Water Quality, and Operations

In this study, we simulated the hydrodynamics and water quality in the Delta between October 1, 2008 and October 1, 2015: a period spanning the relatively wet years of 2010 and 2011, and the drought years of 2013 to 2015 (CDWR c2017) (Figure 3). During this period, high-resolution tidal water-level data was available at Martinez. In addition, the calibration window of the most recent version of *DSM2* overlaps this period (CDWR c2014). We chose the duration of the data sets so as to include seasonal variations between the low inflow summer and autumn months and the high inflow winter months, as well as inter-annual variability in the hydrology.

In these 7 years, the flow in the Sacramento River compared to that in the San Joaquin River was nearly three to seven times higher in the wet years, and nearly ten to fifteen times higher in the critically dry years. The total annual inflow ranged between 6.7 and 29.6 million acre feet (maf) with periodic high-flow events in the winter months. The flow was minimal in Yolo Bypass except in April 2011 (CDEC c2016) (Figure 3A).

The mean water level at Martinez above the North American Vertical Datum of 1988 (NAVD88; see

https://doi.org/10.15447/sfews.2018v16iss2art6

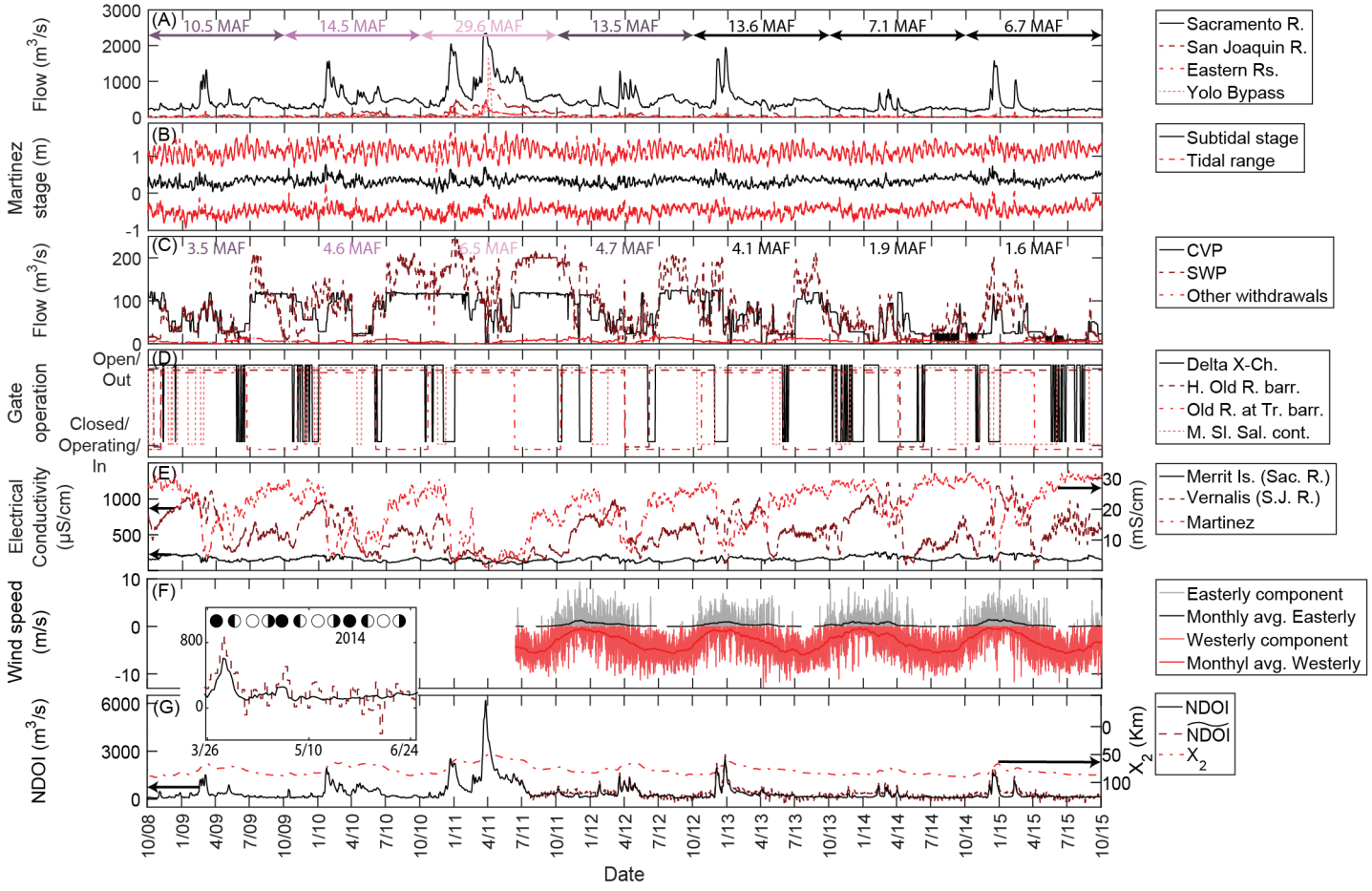

Figure 3 Mean daily Delta hydrology during the study period: (**A**) inflows, (**B**) tidal water levels and range at Martinez, (**C**) exports, (**D**) gate (closed/open for the Delta Cross Channel, and operating/open for the Salinity control gate) and barrier (in/out) operations, (**E**) electrical conductivity, (**F**) East–West winds at Pittsburg, and (**G**) the Net Delta Outflow Index (NDOI) and X_2. In (**A**) and (**C**), we demarcate water years and total annual inflow or exports as critical, dry, below normal, above normal, and wet (dark to light). For clarity, in (D) we slightly shifted each operation policy vertically. In (**E**), we indicate the electrical conductivities in the Sacramento and San Joaquin rivers on the left axis, and the electrical conductivity at Martinez on the right axis. In (**G**), we indicate NDOI on the right axis, and X_2 on the left axis. We show $\widehat{NDOI}$ and NDOI in 2014 with the moon phases, i.e, full moon (*filled circle*), waning (*left filled circle*), new moon (*circle*), or waxing (*right filled circle*) in the inset.

NGS c2004) was 0.33 m, and the daily tidal range fluctuated between 1 m and 2.3 m (CDEC c2016) (Figure 3B). Both the mean water level and tidal range had relatively stationary statistics during this period.

The pumps exported about 20–35% of the total inflow during this period, with typically higher exports in the wet years than in the dry years. Export flows generally peaked during summer to late autumn (CDEC c2016) (Figure 3C). The export flows strongly influenced the net subtidal flow in the OMR corridor—known as the OMR flow—and even reversed the prevailing flow direction when they exceed the river flow (Kimmerer 2011).

To aid salmon passage during this period, the DCC was typically closed intermittently in the summers and late autumns, and every December between 2009 and 2015 (USBR c2018). The salmon passage barrier

at the head of Old River was typically closed in the spring and autumn of each year, except in 2009, 2010, and 2013, when experiments were conducted with non-physical barriers such as strobe lights, noise-makers, and bubble curtains to discourage salmon in the San Joaquin River from swimming into the Old River (BDO c2018). Temporary barriers to aid agricultural water withdrawals were typically installed in the summers and late autumns every year (BDO c2018). The salinity control gates in Montezuma Slough were typically operated in autumn and winter every year (CDWR c2018) (Figure 3D).

The mean daily electrical conductivity in the South Delta was about 555 μScm^{-1}, and peaked periodically to about 1,300 μScm^{-1} between late autumn and spring each year during this period. In the North Delta, it was lower (165 μScm^{-1}) and less variable. The oceanic electrical conductivity at Martinez ranged between 1,150 μScm^{-1} and 32,000 μScm^{-1} with a mean of 20,700 μScm^{-1}. There was a significant dip in Delta salinity coincidental with the extreme high flow event in February and March of 2011 (CDEC c2016) (Figure 3E).

The east–west wind patterns at Pittsburg (Figure 1) are representative of atmospheric conditions in the whole Delta (Monismith 2016). Generally, easterly winds prevailed in the winter months, and westerly winds prevailed the rest of the year. On average, the easterlies were about one-fifth the strength of the westerlies. These westerlies typically sustained for longer than the easterlies (Figure 3F).

The total observed and predicted subtidal outflow from the Delta, using the CDWR's water balance analysis, DAYFLOW (CDWR c2016), is called the Net Delta Outflow Index (NDOI). This water account uses the gauged flow in rivers upstream of the Delta, estimates of minor ungauged flows, flows at the pumping facilities in the southern Delta, and within-Delta precipitation measurements and consumptive use estimates to arrive at the at Chipps Island (Monismith et al. 2002). The NDOI closely follows trends in Delta inflow (Figure 3G). X_2, the distance from the ocean to the location where the salinity is 2 psu, is a measure of salinity intrusion, and varies inversely to the NDOI between downstream of Carquinez Strait (<60 km), and upstream of Rio Vista (>90 km) (Figure 3G).

3. HYDRODYNAMIC MODELING IN THE DELTA

Estuaries are surface water systems in which complex physical mechanisms interact with one another. In this section, we briefly survey the literature on the challenges of modeling a system such as the Delta and the typical modeling effort expended. We particularly focus on processes that can potentially be incorporated into DSM2. Kimmerer (2004) provides a more thorough review of the hydrodynamic processes occurring in the Bay–Delta system.

3.1 Physical Processes Involving Tides in Estuaries

Tidal effects in estuaries must be modeled accurately to reproduce the propagation (e.g., Buschman et al. 2010) and dissipation/intensification (e.g., Zhong and Li 2006) of the harmonic components of the tides, and to recover the spatial patterns of the tidal energy dynamics (e.g., Kowalik and Proshutinsky 1993). These patterns affect various transport and mixing processes such as *tidal excursion* (Fischer et al. 1979), *tidal pumping* (Becherer et al. 2016), *trapping* (Smith and Stoner 1993; Sassi et al. 2011), and the *tidal random walk* (Ridderinkhof and Zimmerman 1992) (see Appendix A for a review of these processes).

In the Delta, in addition to the transport and mixing processes described in Appendix A, subtidal *wind-driven flow* and *gravitation circulation* (salinity gradient-driven flow), which adjust the river flow (henceforth referred to as *subtidal adjustment flows*), are also important (see Appendix A).

The water surface set-up caused by wind shear in the western Delta is important in the fortnightly oscillatory exchange flow in the Delta (Monismith 2016). The spring–neap water level change within the Delta, in part, drives this flow (the moon-phases in the inset in Figure 3G indicate that spring tides [full and new moons] correspond roughly to the filling of the Delta while the neap tides [quarter moons] correspond roughly to its emptying). In addition, the water surface set-up by the wind (Monismith 2016), and the response of the water surface to the coastal ocean also, in part, drive this flow. We approximate

https://doi.org/10.15447/sfews.2018v16iss2art6

this as a daily exchange flow based on Monismith's (2016) analysis (see page 3 of Appendix A) as,

$$Q_W \approx \left\{\frac{C_{D,W}}{10}\Sigma_{i=1}^{M}\left[Fr_{W,i+1}^2 - Fr_{W,i-1}^2\right]\right\}\frac{A_{SB}L_{SB}}{\Delta t} \qquad (2)$$

where $Fr_W = \sqrt{\frac{\langle |U_W| U_W \rangle}{\left(\frac{\rho_0}{\rho_A}\right) g \langle H \rangle}}$ is a water surface set-up Froude number, which is the ratio of the turbulent kinetic energy supplied by the wind and the potential energy of the wind-driven surface set-up, computed at times $i+1$ and $i-1$, in which $\langle H \rangle$ is the subtidal water column depth of about 12 m (Monismith 2016), $\rho_0 = 1{,}000$ kgm^{-3} and $\rho_A = 1$ kgm^{-3} are, respectively, the background density of water and air, $C_{D,W} \approx 1.3 \times 10^{-3}$ is the drag coefficient at the air–water interface (Fischer et al. 1979), U_W is the instantaneous wind speed 10 m above the water surface at Pittsburg (Figure 1), $A_{SB} \approx 2 \times 10^8$ m^2 and $L_{SB} \approx 20$ km are, respectively, the surface area and length of Suisun Bay (Monismith 2016), and is the number of time-steps of duration Δt in 1 day. Written in this form, Equation 2 simply states that the wind induces an exchange flow, which is just the volume of water dragged by the wind with a body force. This force is amplified because virtually all the work done by the wind is used to move the water rather than to mix the air into the water. After substitution of the numerical values, Equation 2 becomes

$$Q_W \approx 5.2 \times 10^8 \times \frac{\Sigma_{i=1}^{M}\left[Fr_{W,i=1}^2 - Fr_{W,i-1}^2\right]}{\Delta t} \qquad (3)$$

in which the coefficient has units of m^3. With the time-series of U_W at Pittsburg, we can estimate this flow.

The net subtidal flow out of the Delta induced by gravitational circulation is of regulatory interest, because an estimate of this flow may prove useful in controlling X_2 (Monismith et al. 2002). Moreover, although Monismith (2016) showed that the effect of gravitational circulation on the subtidal adjustment flow was small, his analysis was conducted for relatively dry months during which the Delta could be reasonably expected to be well-mixed (Geyer and MacCready 2014; s to Equation A-2.7 on page 4 of Appendix A). In wet months, however, the Delta is likely to encounter strong periodic stratification (see to Equation A-2.8 on page 4 of Appendix A). A simple, but effective estimate for the salinity-induced subtidal flow is the fraction of the subtidal flow that a transient response in the longitudinal salinity field induces, i.e.,

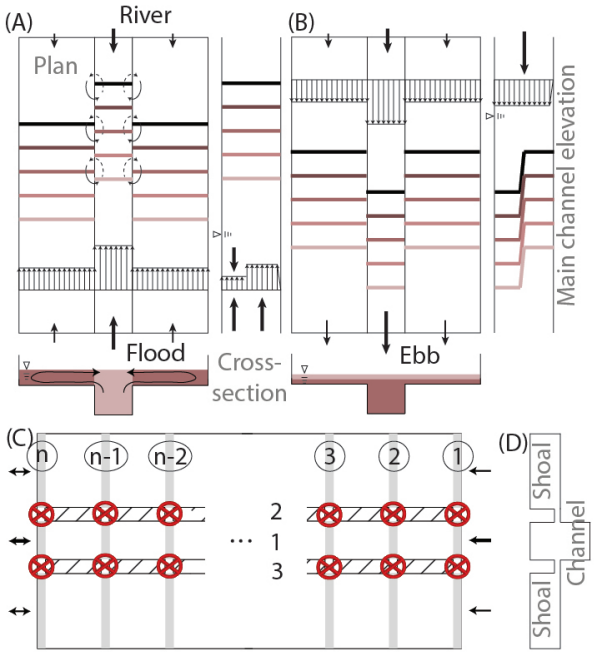

Figure 4 Conceptual representation of flow and salinity indicating the plan, front, and side elevations during the (**A**) flood and (**B**) ebb phase of the tide in a partially-mixed estuary, and (**C**) and (**D**) its idealized representation with interlinked 1-D channels. In (**A**) and (**B**), *bars* indicate the isopycnals (salinity decreases from light to dark); *arrows* indicate flows; *arrow combs* indicate the simplified velocity profiles; *colored regions* and *curved arrows* in the cross-sections indicate salinity levels and circulation patterns, respectively; and *solid* and *dashed curved arrows* in the plans indicate surface and bottom exchanges between the shoals and channel. In (**C**) and (**D**), we idealized the system by three parallel channels which are periodically linked (*hatched regions* indicate channel separations) at nodes (*solid grey boxes* in [**C**]). The caissons (*crossed circles*) close automatically when the water column depth in the shoals falls below a nominal threshold, which simulates wetting and drying.

$$Q_S \approx Q(t) - Q_R(t) = \left(\frac{X_2(t) - 0.919X_2(t-1)}{13.57}\right)^{-7} - \left(\frac{X_2(t)}{167}\right)^{-7} \quad (4)$$

where Q_S is the gravitational circulation-induced flow, t is the current day, and we have applied the expressions for $Q(t)$ and $Q_R(t)$ by rearranging the steady-state version of the auto-regressive X_2 model [Equation 9 in Monismith et al. (2002)]. We argue here that the gravitational circulation-induced flow would account for the difference between the flow that changes the salinity gradient, $Q(t)$, and the mean river flow, $Q_R(t)$. In Equation 4, we can obtain the daily value of X_2 from the DAYFLOW program based on the auto-regressive lag model of Jassby et al. (1995), a model similar to that of Monismith et al. (2002).

In addition to these flows, flood and ebb variations in water column depth and velocity produce a net subtidal landward flux of water known as *Stokes' drift* (Longuet–Higgins 1969). Channel junctions may asymmetrically distribute the flow from Stokes' drift. Stokes' drift also modifies the river flow in open channels and flow splits at junctions (Sassi et al. 2011). These effects cause tide-induced variation in the subtidal flow between the ebb and flood phases of the tide. With the assumption that the channel width is constant, we can write the Stokes' drift as (Monsen 2000; Sridharan 2015) (see "Derivations of Subtidal Adjustment Process Expressions" on page 3 in Appendix A),

$$\begin{aligned} Q_{SD} &= -A\left\langle u'_\eta \right\rangle \\ \left\langle u'_\eta \right\rangle &= \frac{1}{\sqrt{2}} \times 1.1429 \times \frac{\left\langle U'\eta' \right\rangle}{H+\eta} \\ \overline{U'} &= \overline{U} - \left\langle \overline{U} \right\rangle \end{aligned} \quad (5)$$

where, Q_{SD} is the compensatory oceanward subtidal flow from Stokes' drift transport, $A \approx W(H+\eta)$ is the cross-sectional area for a water surface fluctuation η' about its tidally averaged value, W is the width of the channel, u'_η is the subtidal average of the tidal velocity at the water surface, $\langle \overline{U} \rangle$ is the tidally- and cross-sectionally-averaged streamwise velocity, and $\overline{U}'$ is the tidal fluctuation about $\langle \overline{U} \rangle$.

The non-linear interaction between *tidal straining* (or the difference in vertical shear between the flood and ebb phases of the tide) and subtidal adjustment causes *periodic stratification and de-stratification*, which can change the turbulent cross-sectional mixing between the ebb and flood phases of the tide by several orders of magnitude (Simpson et al. 1990). We discuss the case of the partially-mixed estuary, because it involves the most complicated interaction of physical processes, and also because a well-mixed estuary is subsumed within it, while a stratified salt-wedge estuary suppresses turbulent mixing. In Figures 4A and 4B, fresh river water and ocean salinity interact to establish a prevailing longitudinal salinity gradient. In Figure 4A, during the flood phase of the tide, saline ocean water flows through the channel much faster than on the shoals, and establishes a lateral salinity gradient and a flow phase difference. The flow of fresh river water over saline ocean water establishes a vertical shear. The lateral density gradient between the channel and the shoals drives a secondary flow toward the shoals at the bottom, which is balanced by a return flow of freshwater from the shoals into the channel near the water surface (Ralston and Stacey 2005). In Figure 4B, during the ebb phase of the tide, the water column becomes strongly stratified and lateral mixing is suppressed, and water flows out of the system with an almost uniform vertical velocity profile and high frictional retardation in the shoals (Ralston and Stacey 2005). Moreover, if the ebb tide is sufficiently energetic, water surface drawdown can cause the shoals to dry during the ebb phase (Gourgue et al. 2009).

Modeling the tidal dynamics accurately is a precursor to reproducing the transport and mixing mechanisms discussed above and in Appendix A (e.g., Geyer et al. 2000), and the movement and fate of physical and biological scalars such as sediments and fish (e.g., Smith and Stoner 1993). We discuss the literature regarding various modeling approaches to resolve the tidal effects in estuaries below.

3.2 One-Dimensional Modeling

One-dimensional hydrodynamic models are used extensively to model tidal estuaries for a variety of applications such as analyzing estuarine physical processes (e.g., de Brye et al. 2010), shoal–channel interactions (e.g., D'alpaos and Defina 2007), wetting and drying in intertidal flats (e.g., Gourgue et al.

https://doi.org/10.15447/sfews.2018v16iss2art6

2009), sediment transport (e.g., see the review of models by Papanicolaou et al. 2008), dam-breaks and flood routing (e.g., see the review of models by Hunter et al. 2007), water quality (e.g., Zou et al. 2006), transport of pollutants (e.g., Wu et al. 2005), habitats and ecosystems (e.g., Benjankar et al. 2015), aquatic organism movement and fate (e.g., Kimmerer and Nobriga 2008), and the effects of climate change on estuaries (e.g., Zhou et al. 2015).

Predominantly, models such as DSM2 solve the cross-sectionally-averaged Saint–Vénant equations (or shallow-water wave equations), to estimate the flows and water column depths (e.g., DeLong et al. 1997) in estuarine systems (e.g., MIKE11 [Patro et al. 2009] or HECRAS [Brunner 1995]), before coupling the hydrodynamic results to other transport models (e.g., Mike Eco lab [Ma et al. 2011] or DSM2-Qual and Particle Tracking Model [PTM] [SFBDEP 1998]).

One-dimensional models, in general, accurately capture the streamwise propagation of the characteristics of tidal waves, i.e., the landward and oceanward propagation of information resulting from a disturbance in the water level (Kundu and Cohen 2002). However, although 1-D models can resolve the cross-sectionally-averaged tidal pumping, they cannot resolve the wind-driven circulation (Smith 1987) and gravitational circulation.

Another class of 1-D models resolves the vertical dimension while averaging over the lateral and streamwise directions (e.g., MacCready 2004; Ralston et al. 2008). This is only applicable near the mouths of estuaries where gravitational circulation is the dominant hydrodynamic process. We have only included references to such models here for completeness.

The attractiveness of 1-D models is that they have significantly shorter run times than do multi-dimensional models, and so entire-system scale simulations over very long periods (multi-year) are possible (e.g., Sridharan et al. 2018). However, these models sacrifice hydrodynamic fidelity for speed (Fleenor et al. 2010). This trade-off is acceptable so long as either the critical physical processes being studied are incorporated (e.g., the dead zone transport and mixing model described in Atkinson and Davis [2000]), or if the results are interpreted within the limitations of the model. Two-dimensional and 3-D models are the preferred choice when more complex sub-daily physical processes have to be represented.

3.3 Two- and Three-Dimensional Modeling

When more complex physical processes (see Section 3.1 and Appendix A) have to be represented, or the spatial variability in hydrodynamic fields is to be resolved (see the guide to model selection by Robson et al. 2008), 2-D and 3-D Saint–Vénant equation solvers are invoked. These are used primarily as research tools, or as high-resolution numerical laboratories (e.g., Nam 2018, unreferenced, see "Notes"), because their deployment for long-period studies is extremely resource-intensive.

Efforts to resolve the tidal effects using Saint–Vénant equation solvers have focused on either 3-D finite element (e.g., Dawson et al. 2006) or finite difference/volume models (e.g., Louaked and Hanich 1998). Of these, finite element models are theoretically superior in resolving different harmonic components for variable bathymetries and arbitrary domain shapes (Grotkop 1973). Because of the conflicting requirements of modeling different harmonic components, they are often modeled one by one (e.g., Walters et al. 2013). However, the interactions between the components cannot be captured with this approach; therefore, such results would not be very useful from a management perspective. Alternately, accurate resolution of the total tide involves additional effort such as solving the wave continuity equation (Kolar et al. 1994).

Successfully modeling tidal effects requires accurate numerical solution techniques and robust calibration processes in 3-D models. Typically, previous studies have utilized high-resolution spatial advection schemes such as total variance diminishing (e.g., Louaked and Hanich 1998), and more sophisticated spatial and temporal interpolations that are consistent with the advection scheme used (e.g., Wolfram and Fringer 2013). Recently, some investigations have incorporated shoal–channel processes such as intertidal wetting and drying (e.g., Chua and Fringer 2011; MacWilliams et al, 2015). Many studies have incorporated planwise staggered grids (e.g., Garcia and Kahawita 1986; Wolfram and Fringer 2013) to produce more accurate flow and water column depth estimates. Most modeling efforts have used constant

Table 1 Description of input data and information for hydro

Data	Number of nodes	Data type	Time-step size
Flow boundary nodes	7	Time-series	1 day
Water level boundary node	1	Time-series	15 minutes
Delta inland consumptive use	257	Time-series	1 month
Weirs and culverts	10	Geometry and discharge coefficient	NA
Operated gates	7	Discharge coefficient	1 day-1 month

or spatially varying bottom drag with linearized or quadratic bottom friction as tuning parameters (e.g., Chua and Fringer 2011). A few studies have utilized non-linear forms of the friction term with a harmonic component-dependent vertical dissipation rate in addition to the bottom drag (e.g., Kolar et al. 1994; Moftakhari et al. 2013) or temporally-variable bottom drag (e.g., Freidrichs and Aubrey 1994).

As a comparatively inexpensive alternative to 3-D models, planar 2-D models such as HECRAS 5.0 (Brunner 2016), RMA, RMA2 (RMA 2013), TELEMAC-2D (Galland et al. 1991), FaSTMECH (Nelson et al. 2003), and SRH-2D (Lai 2009) are often used to model estuarine hydrodynamics. Such models rely on the relative unimportance of vertical mixing of momentum compared with its horizontal balance. The philosophy underlying these models is that the geographic resolution of hydraulic features, rather than the representation of complex physical processes, is sufficient to explain most of the observed spatial and temporal variations in the hydrodynamic quantities. These models, consequently, do not fully represent the effects of baroclinic circulations, such as shoal–channel lateral exchange flows in which the isobars and isopycnals are not aligned (MacCready and Geyer 2010). They instead focus on solving the 2-D Saint–Vénant equations with finely-resolved domain bathymetry and bottom friction, finite element (e.g., TELEMAC-2D, FaSTMECH, and RMA2), finite difference (SRH-2D), or finite volume (e.g., HECRAS 5.0) approaches.

In the Delta, apart from DSM2, both 2-D and 3-D modeling approaches are routinely adopted. Two-dimensional representations include RMA and RMA2 (RMA 2013). Three-dimensional representations include the TRIM structured grid (Gross et al. 1999) and SUNTANS (Chua and Fringer 2011), UnTRIM (MacWilliams et al. 2015), and DELFT-3D (Martyr-Koller et al. 2017) unstructured grid finite volume; and the SCHISM unstructured grid finite element (Chao et al. 2017) models.

4. MATERIALS AND METHODS

We used the most recent version of DSM2, v8.1.2, to model the hydrodynamics and electrical conductivity in the Delta (Sections 4.1 and 4.2). We compared the model results with both the standard configuration and our recommendations with observations (Sections 4.3 and 4.4) from continuous monitoring stations throughout the Delta (Figure 1; see Section 4.4). For this comparison, we developed a comprehensive model-evaluation protocol (see Section 4.5).

4.1 Model

DSM2-Hydro, described in detail by Anderson and Mierzwa (2002) (see also Sridharan 2015) solves the cross-sectionally-averaged Saint–Vénant equations (Sobey 2001) on a network of 1-D channels, each with cross-sectional area A, hydraulic radius R_H, quadratic bottom friction represented by a Manning's n and conveyance K, flow Q, water level η, and lateral seepage and drainage flows q, as (Kimmerer et al. 2008)

$$\frac{\partial A}{\partial t}+\frac{\partial Q}{\partial x}-q=0$$
$$\frac{\partial Q}{\partial t}+\frac{\partial\left(Q^2/A\right)}{\partial x}=-gA\frac{Q|Q|}{K^2} \quad (6)$$
$$K\approx\frac{AR_H^{2/3}}{n}$$

Equation 6 is solved on the FourPt stencil with two adjacent spatial nodes and two time-steps (DeLong et al. 1997). The numerical scheme allows a range of settings from first-order upwinding to second-order

https://doi.org/10.15447/sfews.2018v16iss2art6

quadrature spatial interpolation and Forward Euler to Crank–Nicolson time-stepping (Venutelli 2002). Simulations are performed centered in space and with slightly more diffusive time-stepping than Crank–Nicolson for stability (Anderson and Mierzwa 2002).

In the DSM2 grid, the waterways of the Delta are represented as 1-D channels, and grid cell ends as well as river junctions as nodes (Figure 2). The grid also includes water management structures (Table 1) (Anderson and Mierzwa 2002). Cross-sections at each node are represented by subgrid bathymetry—coarse grid cells that have the same cross-sectional area and hydraulic properties as the fine-scale bathymetry (Casulli 2009). These are implemented as elevation-width-wetted perimeter-area look-up tables (Anderson and Mierzwa 2002). Flooded islands are treated as continuously stirred tank reactors or "reservoirs." Boundary flows are generated using DAYFLOW (Anderson and Mierzwa 2002), and CDWR supplies time-series of gate operations (CDWR c2014). Lateral seepage and drainage flows at several nodes (Kadir 2006) are also incorporated in DSM2 as mass balances on a monthly time-scale.

DSM2-Qual (hereafter, Qual), described in detail by Liu and Ateljevich (2011), is typically used to model electrical conductivity as a proxy for salinity in the Delta. The ionic composition of water changes from sulfates of leached metals from soils caused by agricultural runoff in the south and central Delta, to light metal halides and bicarbonates in the North Delta, to chlorides and bromides from oceanic influence in the western Delta (Harader et al. 2007). As a result, salinity itself is a non-conservative tracer in the Delta, which makes its direct computation challenging.

Qual extends the Branched Lagrangian Transport Model (BLTM) of Jobson and Schoellhammer (1993), a 1-D finite volume water quality model in which a parcel of water with a specified concentration of a water quality constituent enters a channel and occupies a reach of length $\frac{|Q|}{A}\Delta t$ (set by the time-step size, flow rate, and channel cross-section area). This parcel is then followed over time as the constituent within it is mixed with its upstream and downstream neighboring parcels. The extension in Qual involves reformulating the original discretization scheme for the flux of constituents between parcels. The original scheme specified flux in terms of the concentration difference between neighboring parcels, which introduced spurious numerical diffusion in long parcels and reduced mixing in short parcels. The new discretization scheme specifies flux in terms of the gradients of the constituents, thereby altogether eliminating the dependence of mixing on the parcel length. The advection–dispersion equation being solved is (Liu and Ateljevich 2011)

$$\frac{\partial C}{\partial t}+\frac{Q}{A}\frac{\partial C}{\partial x}=\frac{1}{A}\frac{\partial}{\partial x}\left(l_1|Q|\frac{\partial C}{\partial x}\right) \tag{7}$$

in which l_1—called the "dispersion coefficient" for a given channel in DSM2—is actually the integral mixing length scale (Fischer et al. 1979), i.e.,

$$l_I=\frac{K_x}{U}=0.011\frac{1.486}{n}\frac{W^2R_H^{1/6}}{H\sqrt{g}} \tag{8}$$

based on Fischer's approximation for the shear flow dispersion coefficient and Manning's formula for the mean river velocity (Liu and Ateljevich 2011).

A third model, DSM2-PTM, included in the DSM2 suite, is intended to stochastically simulate the movement of passive particles and aquatic organisms such as fish, fish eggs, and larvae within the Delta (Hutton 1995). Many studies have analyzed the performance of the PTM (Kimmerer and Nobriga 2008; Gross et al. 2010; Sridharan 2015; Sridharan et al. 2018), and we do not discuss this model further here.

We note that as we prepare this manuscript, CDWR is extending DSM2 to include the General Transport Model (GTM). CDWR proposes to incorporate real-time coupling between the momentum and transport equations in the GTM (Hsu et al. 2016). This has the potential to incorporate cross-sectionally-averaged effects of subtidal adjustment into the hydrodynamic solution as well. We also note that CDWR is currently improving its model of lateral seepage and drainage flows through the Delta Channel Depletion Model (DCDM) to include hyporheic flows with electrical conductivities that are associated with agricultural runoff, as well as to provide daily estimates of lateral sources and sinks into DSM2's models (Liang 2018, unreferenced, see "Notes"). The implementation of this model is also expected to improve DSM2's fidelity.

4.2 Calibration and Validation Status

DSM2 has been extensively calibrated and tested over 2 decades (CDWR c2011). It has been tested with a suite of simple conceptual set-ups (Zhou 2013) for model consistency. In these tests, Hydro and Qual have recovered expected solutions.

DSM2 has also undergone regular recalibration to reflect the current hydrologic and geomorphological state of the Delta (CDWR c2011). These efforts have typically involved (1) minor modifications to the DSM2 grid such as the addition or deletion of nodes and reservoirs (CH2M Hill 2009), (2) updating the hydraulic parameters (CH2M Hill 2009), and (3) modifying the mixing length scale parameter (Liu and Sandhu 2012). The subgrid look-up tables for the different model cross-sections represented in the model grid were updated in 2000 for most of the Delta. The upstream boundary in the Sacramento River, and the subgrid look-up tables between Freeport and Sutter Slough were updated in 2009 to reflect current bathymetry (CH2M Hill 2009). During this recalibration, Liberty Island (Figure 2) was added as an additional reservoir in the model grid, and the representation of the Sacramento River was extended to allow the radiation of the landward wave characteristic (CH2M Hill 2009).

In version 8.1.2, the formulation of the subgrid hydraulic look-up table and Hydro's standard usage of the spatial quadrature were modified to avoid spurious water level changes resulting from the incorporation of local bathymetric features into the channel bottom slopes (Liu et al. 2013). In addition, the definition of l_I was updated in Qual (Liu and Ateljevich 2011). These model changes necessitated the most recent recalibration effort, which was undertaken between 2009 and 2011 (Liu et al. 2012).

Hydro has been calibrated to the instantaneous water level referenced to NAVD88 and flow at 42 locations within the Delta (CDWR c2014). CDWR performed the calibration for the periods of October 1, 2001 to October 1, 2002 and October 1, 2002 to October 1, 2008, and performed the calibration for the periods between October 1, 2006 to October 1, 2007 and October 1, 2009 to October 1, 2010 (Liu and Sandu 2013). Qual has been calibrated to the daily averaged electrical conductivity at 31 locations within the Delta (CDWR c2014). CDWR performed the calibration for the period of October 1, 2001 to October 1, 2008 (CH2M Hill 2009), and rescaled the mixing length scale for all channels by a factor of 1425 (Liu and Sandhu 2013). We briefly discuss the validation results in CDWR (c2014) subsequently.

Generally, DSM2 predicted water levels very accurately, with R^2s in excess of 0.95 and phase lags between the model results and the observations of less than 20 minutes almost everywhere in the Delta. The longest phase lags of about 1 hour occurred in Sutter and Steamboat sloughs. The primary shortcoming was that the low–low water levels throughout the Delta were under-predicted.

In the case of flows, the model's primary shortcoming was predicting smaller peak floods. In the San Joaquin River and the south and central Delta, R^2s typically worsened to between 0.3 and 0.9, and phase lags increased to between 20 minutes and 80 minutes. The primary shortcomings in these locations were under-prediction of peak floods, amplitude damping, and incorrect phase predictions.

In general, DSM2 predicted electrical conductivities reasonably well, with typical R^2s of about 0.8 to 0.9. The primary mismatch was that the model missed high-salinity events associated with low river inflows.

CDWR achieved an optimal trade-off among accuracy, storage requirements, and run time for Hydro with the standard grid with a time-step of 15 minutes (Liu and Sandhu 2012). The difference in accuracy between model runs with time-steps of 15 minutes and 5 minutes was typically about 1–2% (Liu and Sandhu 2013). Similarly, for Qual, the difference in overall accuracy between model runs with time-steps of 15 minutes, 5 minutes, 3 minutes, and 1 minute was typically less than 1% (Liu and Sandhu 2014). For these reasons, the standard time-step size prescribed for Qual is also 15 minutes (Liu and Sandhu 2014).

4.3 Description of Experiments

We implemented several proposals both to improve model representation, and to incorporate some of the unmodeled physical processes. In the former category, we increased the spatial resolution of the model grid, increased the temporal resolution of the tidal boundary conditions, and reduced the time-

https://doi.org/10.15447/sfews.2018v16iss2art6

step size so as to adhere to CFL and *R* values of about 1. It is also important to extend the model domain to allow for the radiation of the oceanward-propagating tidal wave characteristic, as well as to improve the modeled water level response to oceanic water level variability. However, because complex 2-D circulation processes occur in the Bay, it is very difficult to incorporate an extension up to the Golden Gate (Figure 1) without extensive calibration. We therefore extended the domain to include Carquinez Strait (thick line in Figure 2). In the latter category, we parameterized shoal–channel interactions and wetting and drying processes to capture important unmodeled physical processes. We describe these configurations below.

To evaluate the model's performance for typically used configurations and to evaluate our proposals, we ran Hydro with multiple time-step sizes and grid resolutions, and with tidal boundary conditions of varying temporal resolution (Table 2) (V.K. Sridharan, unpublished data, see "Notes"). We performed all the analysis using MATLAB (The MathWorks, Inc. 2016).

We first represented the typical configurations with which DSM2 is used in three runs (model configurations G1T*B1). We forced these runs with the California Data Exchange Center (CDEC) data at Martinez (CDEC c2016). Of these, we only ran the G1T15B1 configuration over the water years between 2009 and 2015 to analyze DSM2's response to inter-annual hydrologic variation. We ran the two other configurations for the water years between 2013 and 2015 to compare the results with those obtained using fine-resolution boundary conditions. In setting the duration of these runs, we were restricted by the availability of high-resolution data at Martinez (see "Data Processing" later in the text).

Table 2 Description of DSM2 runs

Run ID [a]	DSM2 modules run	Description	Grid resolution	Time step size	Boundary condition time step size	Boundary data source	Duration	CFL	Resolution criterion
G1T60B1	Hydro, Qual	Coarse run	Original	1 hour	1 hour	CDEC	Oct 1 2013 to Oct 1 2015	7.0	1
G1T15B1	Hydro, Qual	Standard run	Original	15 minutes	1 hour	CDEC	Oct 1 2008 to Oct 1 2015	1.8	4
G1T5B1	Hydro, Qual	Fine run	Original	5 minutes	1 hour	CDEC	Oct 1 2013 to Oct 1 2015	0.6	12
G2T5B1	Hydro, Qual	Fine run on dense grid	2x	5 minutes	1 hour	CDEC	Oct 1 2013 to Oct 1 2015	1.2	12
G1T5B2	Hydro, Qual	Fine run with hi-res boundary	Original	5 minutes	6 minutes	NOAA-TC [b]	Oct 1 2013 to Sep 1 2015	0.6	1.2
G2T5B2	Hydro, Qual	Fine run on dense grid with hi-res boundary	2x	5 minutes	6 minutes	NOAA-TC [b]	Oct 1 2013 to Sep 1 2015	1.2	1.2
G1T15BB	Hydro	Standard run with Carquinez Strait extension	Original	15 minutes	6 minutes	RTC [c]	Oct 1 2009 to Sep 1 2015	1.8	0.4
G2T5BB	Hydro	Fine run on dense grid with Carquinez Strait extension	2x	5 minutes	6 minutes	RTC [c]	Oct 1 2009 to Sep 1 2015	1.2	1.2
GtT15BtSC1	Hydro, Qual	Toy grid to investigate shoal-channel circulation	Toy grid	15 minutes	15 minutes	Simulated small M2 tide	3months	2.7	1
GtT1BtSC2	Hydro	Toy grid to investigate shoal-channel wetting and drying	Toy grid	1 minutes	15 minutes	Simulated large M2 tide	3 months	0.2	15

a. Nomenclature GiTjBk is defined as grid (*G*) of resolution *i*, with time step size (*T*) of *j*, and boundary condition type (*B*) of *k*.
b. NOAA-TC Martinez Amorco Pier buoy data.
c. RTC Carquinez Strait buoy data.

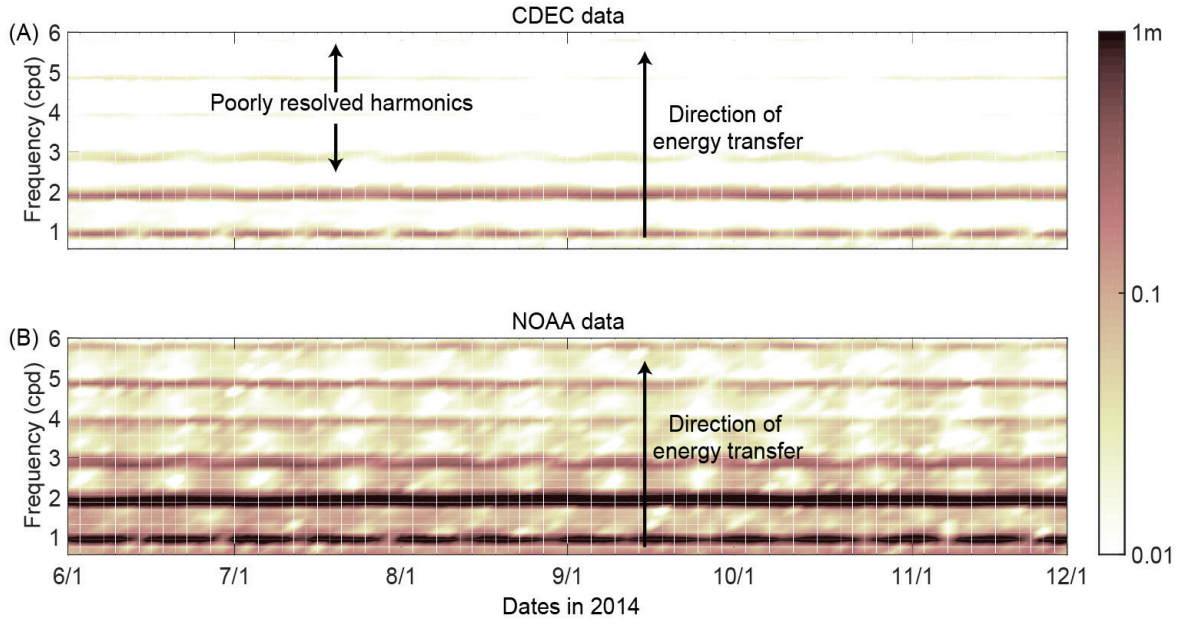

Figure 5 Spectrograms of the boundary condition time-series at Martinez: (**A**) hourly CDEC data, and (**B**) 6-minute NOAA buoy data. The energy content of various tidal harmonics (equivalent to the contribution of that harmonic to the tide height) is much better resolved in the NOAA data set than in the CDEC data set. In each plot, the arrows indicate the prevailing direction of energy transfer between the tidal harmonics. In each case, we generated the spectrogram with 64 frequencies and a 15-day moving Hamming window (parameters $\alpha = 0.54, \beta = 0.46$) with a 50-hour overlap.

In the next three runs (model configurations G*T5B*), we evaluated the model for several grid sizes and boundary condition resolutions. We forced DSM2 with a fine temporal resolution tidal boundary using National Buoy Data Center's Amorco Pier tide gauge buoy data at Martinez, available from the National Oceanic and Atmospheric Administration–Tides and Currents (NOAA–TC) database (NOAA–TC c2013). The buoy data resolved the energy transfers to the higher than semi-diurnal frequencies significantly better than the CDEC data (Figure 5). We ran these configurations for the water years between 2013 and 2015 as well.

We varied the grid resolution from the standard DSM2 grid by adding one new piecewise trapezoidal cross-section at the midpoint between existing cross-sections in each channel (Figure 6), provided the new cross-sections were at least 762 m (2,500 ft) away from either existing cross-section (see "Prescriptions for Model Recommendations" on page 5 of Appendix A). Using these new cross-sections, we generated a grid that was twice as fine as the original grid. We interpolated the hydraulic properties of

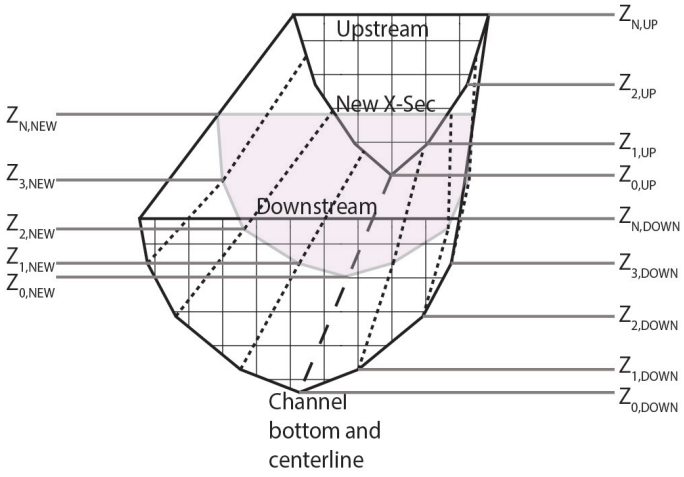

Figure 6 Interpolating cross-sections on finer-resolution DSM2 grid. Dashed line is the channel bottom and centerline. Dotted lines are the linear interpolating functions. $Z_{i,UP}$s represent elevations in original upstream cross-hatched cross-section. $Z_{i,DOWN}$s represent elevations in original downstream cross-hatched cross-section. $Z_{i,NEW}$s represent elevations in interpolated shaded cross-section.

https://doi.org/10.15447/sfews.2018v16iss2art6

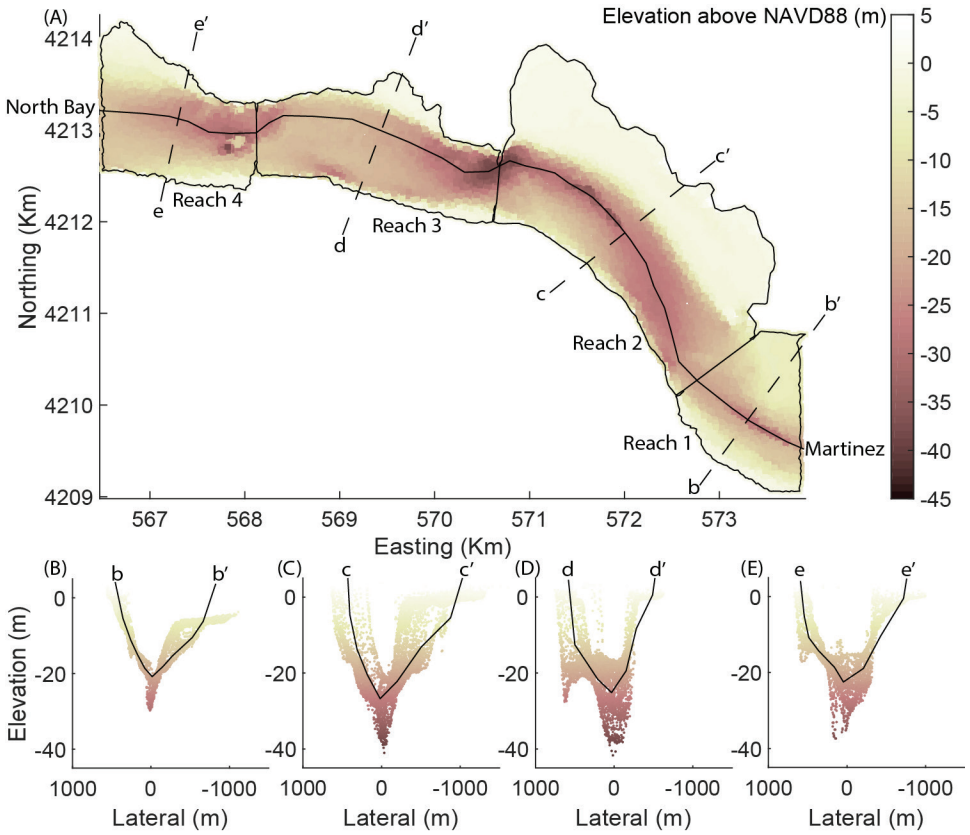

Figure 7 Extension of the DSM2 grid to include Carquinez Strait: (**A**) bathymetry referenced to the NAVD88 datum, the thalweg (*solid black line*), DSM2 digitization into four reaches (*black polygons*); and model cross-sections (*dashed black lines*); and (**B-E**) elevation of bathymetric points in each reach and average cross-sectional profiles (*solid black lines*).

the new sections linearly from the existing sections, proceeding from the highest elevation downward, with the number of elevations in the new cross-section equal to the number of elevations in its downstream cross-section (Figure 6). This method of refining the grid is the best practice possible, because DSM2 has been calibrated such that model cross-sections often do not match true bathymetry (Smith and Enright 1995). Furthermore, Liu et al. (2012) applied a similar interpolation scheme to insert new computational sections within Hydro, so that the method adopted here of resolving the grid is consistent. In addition to these runs, we performed several simulations—described subsequently—to explore some of our proposed model improvements (see Section 6.2).

We also performed two runs in which we extended the grid to include the Carquinez Strait (Figure 7; see "Prescriptions for Model Recommendations" on page 5 of Appendix A) as a surrogate for San Francisco Bay (model configuration G*T*BB). For these runs, we used the Romburg Tiburon Center (RTC) buoy data in Carquinez Strait (RTC c2017) to force the model in the water years between 2010 and 2015. In these runs, we did not rigorously calibrate the hydraulic parameters of the channel that represented Carquinez Strait; such an effort was well beyond the scope of this work. However, we did account implicitly in a spatially-averaged sense for the natural sill in Carquinez Strait; the cross-section $c-c'$ is 4.87 m deeper than the cross-section $b-b'$ in Figure 7, though the actual elevation differential at this sill is about 7 m (Schoellhamer 2001). We also did not run Qual with these configurations, because we did not expect to get useful water quality results with an uncalibrated model. Here, we demonstrate only the value of the approach.

We then performed two "toy" runs of 3 months' duration in which we simulated an artificial M_2 tide forcing a shoal–channel system (model configurations GtT*BtSC*). The model grid for these runs was a simplified representation of the TRIM-3D circulation model of the Central Bay in Ralston and Stacey (2005) comprising a deep main channel and two connecting, wide, shallow side channels (Figures 4C and 4D; see "Prescriptions for Model Recommendations" on page 5 in Appendix A). This approach has been adopted earlier in HEC-RAS by prescribing wide shoal channels with large Manning's $n \sim 0[(10\text{-}100) \times n_{Main\ channel}]$ corresponding to a floodplain parallel to the main channel (Brunner 2003). This implementation also necessitated incorporating a wetting and drying scheme for the shoals. A wetting and drying scheme in the Suisun Bay region of the grid would allow for better representation of the retardation of tides by friction. In reaches of a channel where the cross-sectional area fluctuates markedly, DSM2 rather unrealistically restricts these fluctuations. Instead, wetting and drying can add realism here, too. However, while a wetting and drying scheme such as the one adopted by Chua and Fringer (2011) would require a significant rewrite of the code, here we proposed a very simple alternative (see "Prescriptions for Model Recommendations" on page 5 in Appendix A). We operated a series of numerical caissons, or buoyant radial gates, in the shoals, which closed off the flow when the water column depth fell below a 3-cm threshold (Figure 4C).

In each run, we began the simulation on June 1 at midnight, to allow the model to spin-up over a period of 4 months. We also note that because of a restriction on the minimum length of a parcel of water entering a channel in DSM2 (Liu and Ateljevich 2011), the maximum time-step size Qual could be run with is 15 minutes. Therefore, we ran Qual with a time-step size of $\max(\Delta t_{Hydro}, 15 \text{ minutes})$.

4.4 Data Processing

To force the model, as well as to assess its fidelity, we obtained hourly flow, water level, and electrical conductivity data at different locations within the Delta and Carquinez Strait from the CDEC website (CDEC c2016). We compared model results with field observations of flow at 46 locations (and one aggregate subtidal flow record called "OMR"); water levels at 60 locations; and electrical conductivity at 77 locations (Figure 1, Table 3, and Tables A-4.1 through A-4.12 in Appendix A). We used the MATLAB-based KATANA data clean-up toolbox (Sridharan 2018, unreferenced, see "Notes") to quality control the data (see Appendix A).

Table 3 Description of observations in the Sacramento River

Region	Geographic extent and description	Number of stations	Reference to tables in Appendix A[a]
Sacramento River	Mainstem lower Sacramento River in the North to West Delta	8	A-4.1
Sutter and Steamboat sloughs	Forks of the Sacramento River in the North Delta west of Sacramento River	6	A-4.2
Georgiana Slough	North Delta downstream of the Delta Cross Channel	3	A-4.3
South Fork Mokelumne River	Northeast Delta mouth of the Mokelumne River	5	A-4.4
Yolo Bypass	Northwestern floodplain fed by flows overtopping the Fremont and Sacramento weirs	2	A-4.5
Suisun Bay	Western shallow embayment	2	A-4.6
Suisun Marsh	Western intertidal sloughs and marsh	6	A-4.7
Carquinez Strait	Western strait linking Delta with San Francisco Bay	3	A-4.8
Flooded islands	Submerged and leveed agricultural islands in the Central Delta	6	A-4.9
Canals	Transfer structures between the San Joaquin, Old and Middle rivers to the CVP and SWP pumps in the southern Delta	6	A-4.10
Old and Middle rivers	Tributaries of the San Joaquin River subject to tidal and CVP and SWP export flow influences in the South and Central Delta	27	A-4.11
San Joaquin River	Mainstem lower San Joaquin River in the South to Central and western Delta	18	A-4.12

a. Refer to Figure 1 and Tables A-4.1 through A-4.12 in Appendix A for a detailed list of observation locations. and footnotes.

https://doi.org/10.15447/sfews.2018v16iss2art6

Because we wanted to investigate the effect of the temporal resolution of the tidal boundary condition on fidelity in many of these runs, we utilized both the coarse- and fine-resolution data sets described previously. In all cases, we used 15-minute tidal water levels interpolated with a cubic spline from the original data. Although the CDEC and RTC data sets were available for all water years between 2009 and 2015, the NOAA-TC data was available only from May 1, 2013.

To align the NOAA-TC data set with the CDEC data set, we advanced the NOAA-TC data by 0.086 hours and removed the difference in mean water levels between the CDEC data and the NOAA-TC data from the NOAA-TC data. To consistently align the RTC data set with the CDEC data set, we advanced the RTC data by 0.46 hours and removed the height of the tide gauge above the NAVD88 datum from the RTC buoy data.

To estimate the wind-driven circulation, we utilized quality-controlled wind speed and direction data available from between June 15, 2011 and October 1, 2015 at Pittsburg from the San Francisco Physical Oceanographic Real-Time System (NOAA c2013) at station 9415115 following Monismith (2016). To estimate the gravitational circulation, we obtained DAYFLOW estimates of the NDOI and X2 location (CDWR c2016).

4.5 Performance Analysis

We subsequently present an analysis of the following model results: (1) the instantaneous water column depths and flows and the daily averaged electrical conductivities; (2) the tidal effects including the subtidal flows, the harmonic components of the tidal water levels and flows, and the modulations of the subtidal flows by the tidal harmonics; and (3) a comparison of regulatory flow parameters such as the DSM2 estimate of NDOI with the DAYFLOW estimate modified by the subtidal adjustment,

$$\widetilde{\mathrm{NDOI}} = \mathrm{NDOI} - \left(Q_W + Q_S\right) \tag{9}$$

(see Appendix A), and the subtidal OMR flow,

$$Q_{OMR} = \left\langle Q_{OH4} + Q_{MDM} \right\rangle \tag{10}$$

where Q_{OH4} and Q_{MDM} are, respectively, the flows in the Old River at Highway 4 and in the Middle River. We analyze these results for all but the shoal–channel model configurations in Section 5. The results of the shoal–channel process models are primarily proofs-of-concepts, and we discuss these in Section 6.

To study the tidal effects, we performed Short Term Harmonic Analysis (STHA) on the observations and model results using the package T_TIDE (Pawlowicz et al. 2002). STHA (Kukulka and Jay 2003) can account for the non-stationary propagation of tides in rivers that result from variable freshwater flows (Matte et al. 2013). Here, we partitioned the data sets into 3-month-long boxcar windows and performed STHA on the smaller time-series as recommended by Guo et al. (2015). We only analyzed a subset of the principal components of the tides in north San Francisco Bay with periods shorter than 1 fortnight, which were decomposed by *T_TIDE* with a signal to noise ratio ≥2 (Pawlowicz et al. 2002). Of these, we only report the K_1 (23.9-h period), M_2 (12.4-h period), MK_3 (8.2-h period), and M_4 (6.2-h period) components, because the other components behave similarly. We estimated the subtidal hydrodynamic quantities by low-pass filtering the total quantities with a 4th order Butterworth filter with a cut-off period of 50 hours (using zero-phase filtering with MATLAB's *filtfilt* tool). We also report the mean difference in tidal range between the fortnightly spring and neap tides (14.7-day period) by computing the mean of the difference between the peaks and troughs of the range of the envelope of the tidal signal.

Quantifying model accuracy with standard aggregate metrics is challenging, particularly when observations of different quantities are distributed non-uniformly in space (Ganju et al. 2016). As an alternative, we developed two simple aggregate metrics based on the cumulative RMS error (Chua and Fringer 2011) in modeling flow and water level at multiple locations (Figure 8A): the aggregate model error, ε_Σ, and the aggregate skill score, MSS_Σ as (see Appendix A),

$$\varepsilon_{\Sigma,p} = \Sigma_{\phi\in\{H,Q\}}\left[\frac{\sqrt{\sum_{i=1}^{N_\phi}\left(\frac{\varepsilon_{\phi,p,i}^2}{N_{\phi,i}}\right)}}{\sqrt{\sum_{i=1}^{N_\phi}\left(\frac{\phi_{0,i}^2}{N_{\phi,i}}\right)}}\right] \tag{11}$$

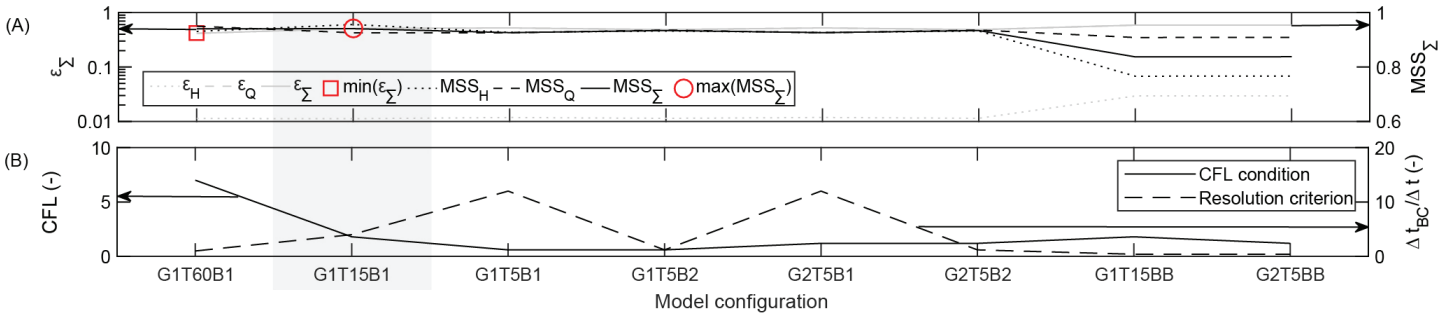

Figure 8 Overall performance of Hydro for various model configurations: (**A**) aggregate model RMS error and skill in estimating the combination of flow and depth, and (**B**) the CFL condition and resolution criterion. In (**A**), the *red shapes* indicate the best-performing model configuration for each criterion, and we reference the aggregate error to the left-hand side ordinate axis, and the aggregate skill to the right-hand side ordinate axis. In (**A**), in addition to the combined aggregate metrics, ε_Σ and MSS_Σ, we also indicate the aggregate measures of performance for flow (ε_Q and MSS_Q) and depth (ε_H and MSS_H). In (**B**), we reference the CFL condition to the left-hand side ordinate axis, and the resolution criterion to the right-hand side ordinate axis. Both CFL and resolution criterion should ideally be about 1. The *shaded box* indicates DWR's recommended model configuration.

$$MSS_{\Sigma,p} = 1 - \frac{1}{2}\Sigma_{\phi\in\{H,Q\}}\left[\frac{\sqrt{\Sigma_{i=1}^{N_\phi}\left(\frac{\varepsilon_{\phi,p,i}^2}{N_{\phi,i}}\right)}}{\sqrt{\Sigma_{i=1}^{N_\phi}\left(\frac{PE_{\phi,p,i}^2}{N_{\phi,i}}\right)}}\right] \quad (12)$$

where, for a model configuration, p, we weight the contributions to the cumulative squared error, $\varepsilon_{\phi,p}^2$, in ϕ by a location, i, by the reciprocal of the number of locations at which observations are correlated with those at this location, $N_{\phi,i}$, and then sum these over all locations where such measurements of ϕ are made. We finally divide the overall weighted RMS error by the overall weighted RMS value of the quantity ϕ, and aggregate the RMS errors over both the water column depth and flow. We compute the $MSS_{\Sigma,p}$ in a similar manner, but here we divide the overall weighted mean squared error by the overall weighted mean squared potential error, $PE_{\phi,p}$, and equipartition the skill between the water column depth and the flow. For simplicity, we chose $N_{\phi,i}$ simply as the number of stations in each region specified in Table 3. An alternative for a more rigorous specification of $N_{\phi,i}$ is to weigh the contribution of each location by the number of locations within the range of the semivariogram for the river-course within which that location is found (Curran 1988).

While such aggregate metrics provide an overview of modeling accuracy, analysis of the local RMS error at each location can reveal insights about the model's strengths and weaknesses, as well as the limits of possible improvements to the model. The cumulative RMS error at a location is

$$\varepsilon_\phi = \sqrt{\frac{1}{N}\Sigma_{i=1}^{N}\left(\phi_{M,i} - \phi_{o,i}\right)^2} \quad (13)$$

where ϕ_M and ϕ_O are, respectively, the modeled and observed quantities at time i.

A close to ideal model would capture all the important physical processes, and hence ε_ϕ should arise largely from the observation precision. For such a model, ε_ϕ in the water column depth and flow should be independently and randomly distributed. To understand the nature of the error for different model configurations in greater detail, we decomposed ε_ϕ in Equation 13 at each location into a systematic component and an unsystematic component (see Section 1 and "Prescriptions for Comparison with Data and Inter-Model Comparison" on page 16 of Appendix A) (Willmott 1981).

We also utilized various metrics to quantify the quality of the spatial and temporal hydrodynamic landscapes predicted by the different model configurations. These include the *coefficient of determination*, R^2, difference maps of the hydrodynamic and water-quality fields between the models and the observations, and succinct target diagrams (Jolliff et al. 2009). We used this multi-

https://doi.org/10.15447/sfews.2018v16iss2art6

pronged approach to analyze different aspects of the model results.

The R^2 of the observations and the model results shifted appropriately by the lead or lag between the two data sets (RMA 2005) measures the similarity in the means and variances of the two data sets. Target diagrams provide a comparison between two related metrics (Jolliff et al. 2009). We applied target diagrams to represent the *unbiased RMS difference (UBRMSD)* and the *bias* (*b*) (Jolliff et al. 2009), between the observed and modeled instantaneous flow. The *UBRMSD* and *b* (Equation A-5.9 in Appendix A) are, respectively, the variances of the modeled and observed time-series and the biasedness of the model predictions (MacWilliams et al. 2015). In these diagrams, we represent on the abscissa and on the ordinate, and include circles of increasing radii centered at the origin that indicate poorer model fits (MacWilliams et al. 2015). In addition to these diagrams, the target diagrams we developed (see "Prescriptions for Comparison with Data and Inter-Model Comparison" on page 16 in Appendix A) provide a comparison between the amplitudes and phase differences of the modeled (respectively, ζ_M and ψ_M) and observed (respectively, ζ_O and ψ_O) harmonic components (MacWilliams et al. 2015). In these diagrams, we represent the fraction of amplitude difference of the observed amplitude, $\frac{(\zeta_M - \zeta_O)}{\zeta_O}$, on the abscissa, and the phase difference normalized by 180°, $\frac{(\psi_M - \psi_O)}{\pi}$, on the ordinate, and include circles of increasing radii centered at the origin that indicate poorer model fits. We intended these latter target diagrams only for tidal harmonic components that are relatively stationary over the time windows considered. Following MacWilliams et al. (2015), we deemed model configurations in which a large fraction of points fell within the radius-1 circle as having predicted the quantities of interest with acceptable fidelity.

Because model accuracy can only be evaluated up to the precision in the data, we ensured that all model results that fell within the observational precision (see "Data Sources and Quality Control" on page 8 in Appendix A) were deemed to have accurately represented the true hydrodynamics. We discuss the results of our analyses below.

5. RESULTS

In this section, we first report on the overall fidelity of DSM2, and then its prediction of the subtidal hydrodynamics and tidal effects. Last, we analyze its prediction of the Delta's key regulatory parameters. We present only the results of the G1T60B1, G1T15B1, G2T5B2, and G2T5BB model configurations here and in Section 6. We present comprehensive results in "Comprehensive Model Evaluation" on page 18 in Appendix A. Since there is no stochasticity in the DSM2 results beyond machine precision (see Sridharan 2015), we cannot discuss the statistical significance of our results. To eliminate any skew because of the hydrologic conditions of the Delta, we used only the model results in the water years between 2013 and 2015 when reporting overall performance for all model configurations.

5.1 Overall Model Fidelity

The overall fidelity was best in model runs with the standard configurations (G1T60B1 and G1T15B1). The aggregate error was smallest with the G1T60B1 configuration; the aggregate skill was highest with the G1T15B1 configuration (Figure 8A). However, the results with the other model configurations without domain extension did not significantly differ from these two configurations. Model results with CDWR's recommended configuration, G1T15B1, had an aggregate error that was about 20% larger than those with the G1T60B1 configuration. A possible explanation is that model configurations generally produced the best overall results when *R* was close to 1. The aggregate skill typically improved by about 1% when the CFL condition approached 1, compared to larger CFL condition values (Figure 8B). Although it is generally preferable to have both the CFL condition and *R* be O(1), the *R* criterion is the more important of the two. The model configurations with the extension to Carquinez Strait (G*T*BB) performed worst (Figure 8A); more rigorous calibration is required in these cases. However, the extension did reduce the systematic error in the model from the reflection of oceanward wave characteristic.

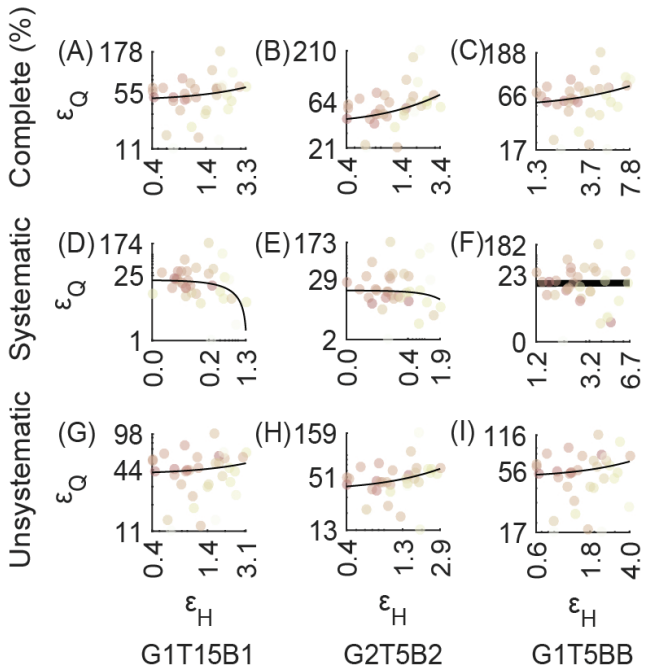

Figure 9 Phase diagrams errors in flow and depth for each location at which observations are available for different model configurations: (**A**–**C**) RMS error, (**D**–**F**) systematic or modeled component of RMS error, and (**G**–**I**) unsystematic or unrepresented physical processes-induced component of RMS error. The scales are logarithmic, the points are *color-coded* by the distances of the locations at Martinez (landward points are lighter), and the lines indicate the Theil–Sen robust linear least squares regression (Ohlson and Kim 2015). In (**B**), the *thick line* indicates de-correlated ε_H and ε_Q.

For all model configurations, at different locations within the Delta, we found correlations between the cumulative RMS errors in flow and water column depth that increased landward (Figures 9A–C and A-6.1). Through error decomposition analysis (Willmott 1981), we found that the systematic error in the flow was correlated inversely with that in the stage, and that this correlation decreased (regression lines in Figures 9D–E) landward (lighter colored points in Figure 9D–E) for all model configurations except the ones with the domain extensions (Figure 9F). In these latter configurations, decreasing the energy of the spuriously reflected oceanward wave characteristic de-correlated these errors (Figures 9F and A-6.1). As expected for a 1-D model, the unsystematic error (Figure 9G–I) was comparable in magnitude to the systematic error (Figures 9D–F and A-6.1). We discuss the implications of these issues in Sections 5.2 to 5.4 below.

5.2 Predictions of Instantaneous Hydrodynamics

To evaluate DSM2's results during various hydrologic and water operations scenarios, we analyzed model results in two scenarios: a wet period with high freshwater inflow (winter of 2014-2015), and a dry period with low freshwater inflow (summer of 2015). For clear visualization, in the scatter plots in Figures 10–12, we equipartitioned the data versus model results space into 100 squares, and plotted boxes colored by the mean instantaneous inflows into the system (light to dark representing low to high flows) in all the records of the time-series that occurred within each square, and sized by the number of records occurring within each square. The model typically achieved higher fidelity when the freshwater inflow was high than when it was low (darker points versus lighter points in the scatter plots in Figures 10 and 11), because of the lower importance of the more complex tidal signal relative to the comparably steady freshwater signal. In addition, as we expected, the model worked best when $R \approx 1$.

DSM2 predicted the instantaneous water column depths and flows at various locations in the Delta reasonably accurately ($R^2 \approx 0.9$), with the coarsest grid, time-step size, and water level boundary condition (Figures 10, 11, A-6.5, and A-6.6). It performed very similarly with other model configurations as well, with a ~2% reduction in R^2 values between the observed and modeled water levels and flows in all configurations. This indicates that the subgrid cross-sectional geometries and Manning's n values in DSM2 have been very well calibrated for the standard configuration, and that any significant improvement would require finer streamwise resolution of the system hydraulics with significant recalibration.

DSM2 predicted daily averaged electrical conductivity with lower accuracy (0.3–0.5) than the water column depths and flows, particularly when the freshwater inflow was very small (Figures 12 and A-6.7). However, electrical conductivity measurements in the central Delta can themselves be quite error-prone, so a comparison between observed and modeled conductivity is limited by data uncertainty as well

https://doi.org/10.15447/sfews.2018v16iss2art6

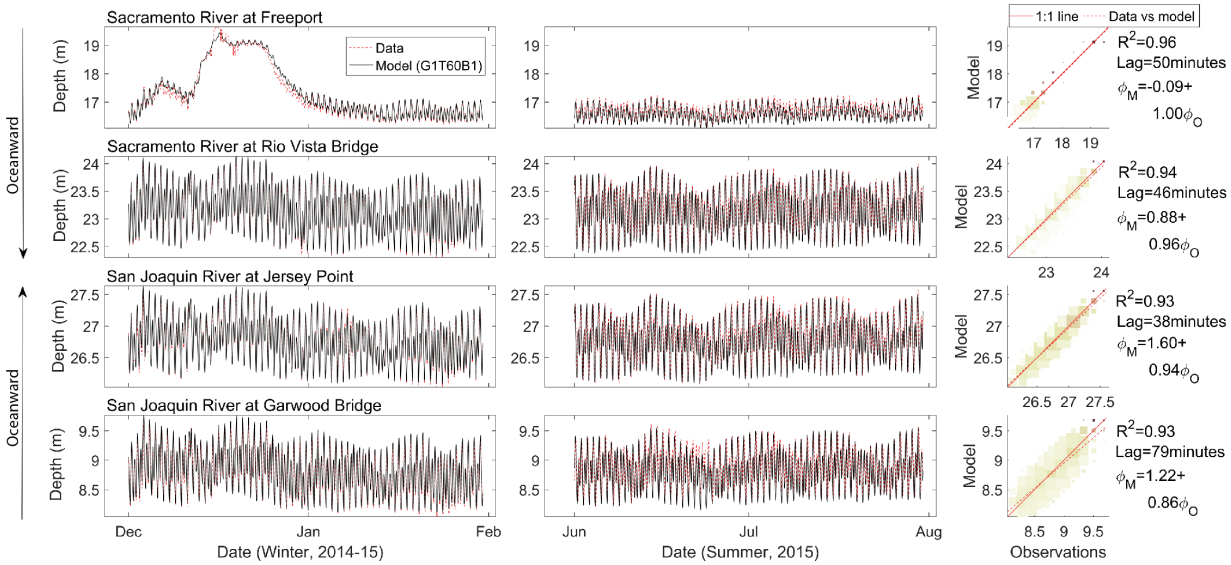

Figure 10 Validation of DSM2 for instantaneous total water level at representative locations in the Sacramento and San Joaquin rivers. For each location, we compare a wet period (December 2014 to February 2015) and a dry period (Jun to August 2015). For clear visualization, in the scatter plots, we equipartition the data versus model results space into 100 squares and plot boxes colored by the mean instantaneous inflows into the system (*light to dark* representing low to high flows) in all the records of the time-series occurring within each square, and sized by the number of records occurring within each square. We indicate the 1:1 correspondence, linear regression of the phase-corrected model results with the observations, the correlation coefficient, and lag. In all the plots, we represent the model configuration, G1T60B1, with least overall RMS error.

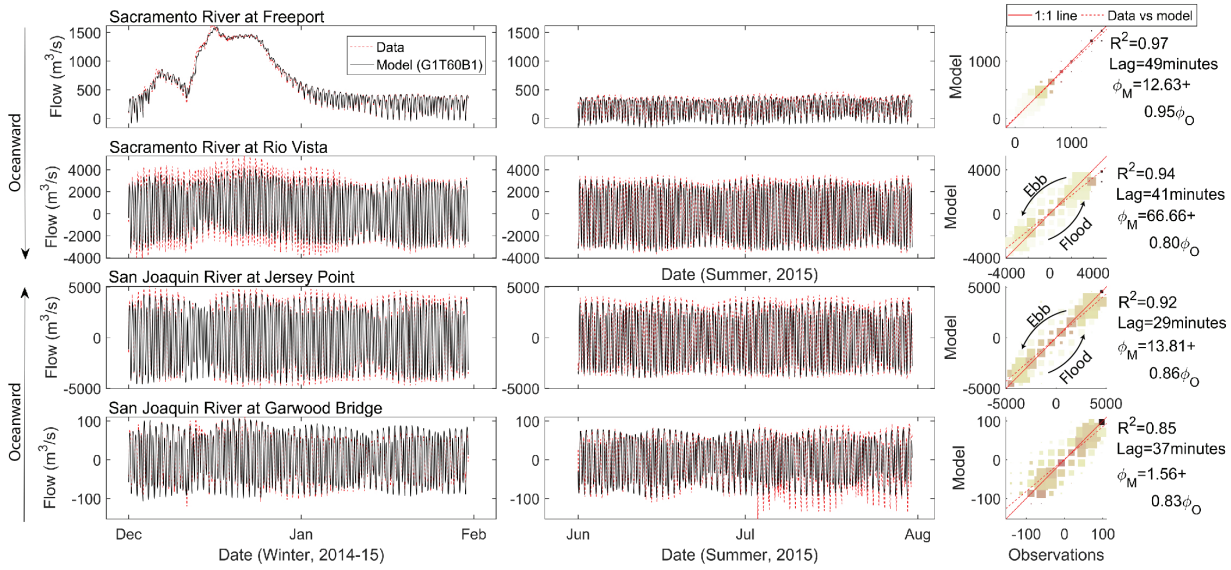

Figure 11 Validation of DSM2 for instantaneous total flow at representative locations in the north and South Delta. For each location, we compare a wet period (December 2014 to February 2015) and a dry period (June to August 2015). For clear visualization, in the scatter plots, we equipartition the data versus model results space into 100 squares and plot boxes colored by the mean instantaneous inflows into the system (*light to dark* representing low to high flows) in all the records of the time-series occurring within each square, and sized by the number of records occurring within each square. We indicate the 1:1 correspondence (solid line), linear regression of the phase-corrected model results with the observations (dashed line), the correlation coefficient, and lag. For the Sacramento River at Rio Vista and the San Joaquin River at Jersey Island, we also indicate the deviations from the observations in the model results by arrows. In all the plots, we represent the model configuration, G1T60B1, with least overall RMS error.

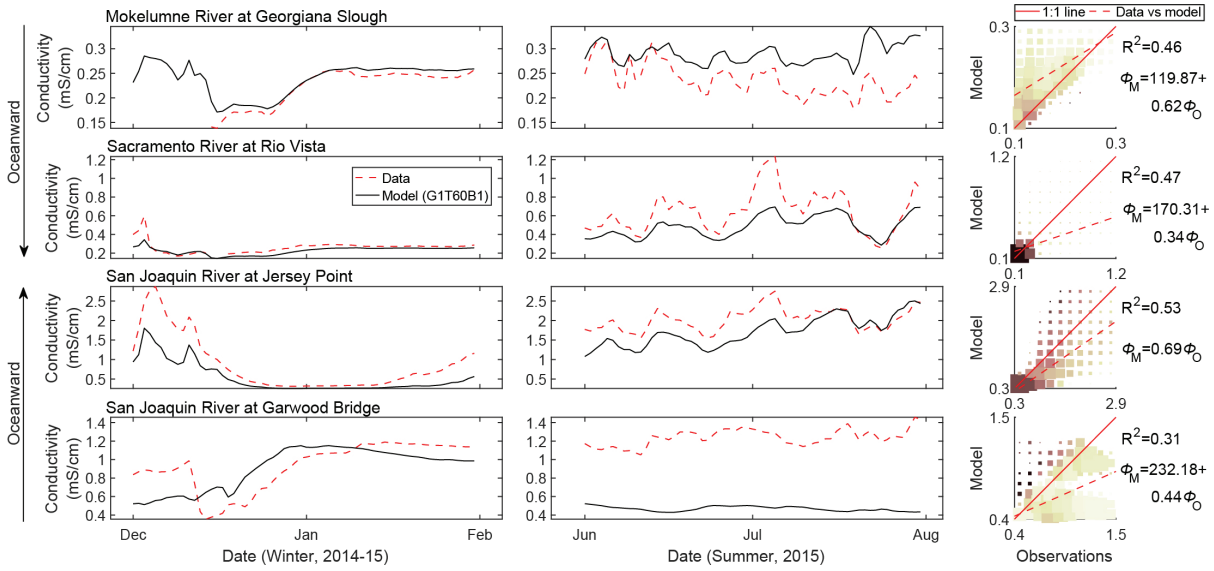

Figure 12 Validation of DSM2 for daily averaged electrical conductivity at representative locations in the north and South Delta. For each location, we compare a wet period (December 2014 to February 2015) and a dry period (June to August 2015). For clear visualization, in the scatter plots, we equipartition the data versus model results space into 100 squares and plot boxes colored by the mean daily averaged inflows into the system (*light to dark* representing low to high flows) in all the records of the time-series occurring within each square, and sized by the number of records occurring within each square. We indicate the 1:1 correspondence (solid line), linear regression of the phase-corrected model results with the observations (dashed line), the correlation coefficient, and lag. In all the plots, we represent the model configuration, G1T60B1, with least overall RMS error.

(2018 in-person conversation between E. Ateljevich and V.K. Sridharan, unreferenced, see "Notes"). The daily averaged electrical conductivity fields in four different hydrologic and water operation scenarios—viz, spring 2011 with high freshwater inflow and low export:inflow ratio; summer 2011 with high freshwater inflow and high export:inflow ratio; winter 2015 with low freshwater inflow and high export:inflow ratio; and summer 2015 with low freshwater inflow and low export:inflow ratio (Figure 3)—indicate that the Delta was relatively fresh during high inflow periods (Figure 13A), and that the western Delta became more brackish during low inflow periods (Figures 13B–D). The entrainment of saline water by the export pumps increased electrical conductivity in the OMR corridor and South Delta as well during low inflow periods (Figures 13C–D). All the model configurations produced almost identical daily averaged electrical conductivity fields (Figure A-6.8). The deviation between the observed and modeled electrical conductivity field was nearly 20–50% during the low inflow periods, and this difference occurred predominantly in the West and South Delta regions (Figures 13B–D).

Fidelity to hydrodynamics was generally better in the western Delta close to the water level boundary where the tidal signal dominates the total water level and flow (e.g., Antioch), or in the north and South Delta where the tidal signal attenuates (e.g., Freeport). Fidelity was low where there was strong coupling between the mean river flow and tidal signal, such as at Rio Vista, or where the export flows interacted with the tidal signal, such as in the OMR corridor (Figures 10, 11, and A-6.5 and A-6.6). As the tide propagated inland and dissipated, the lag between the modeled and observed water levels also increased from about 40 minutes to about 50 minutes in the Sacramento River, and from about 30 minutes to almost 90 minutes in the San Joaquin River (Figures 10 and A-6.5). These trends in the solution accuracy and lag resulted from the increasing numerical dispersion away from the tidal boundary condition (Sobey 2001). A slightly different trend existed in the prediction of flow, in which the

https://doi.org/10.15447/sfews.2018v16iss2art6

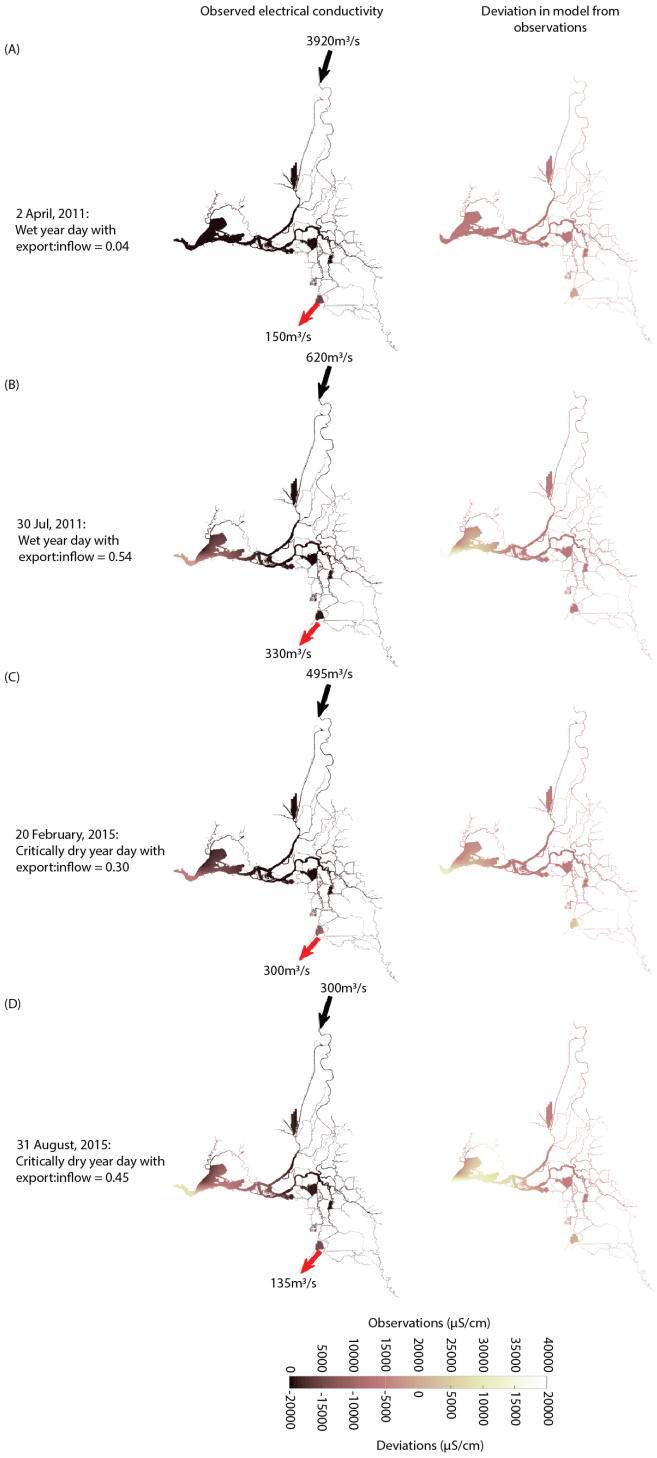

Figure 13 Observed daily averaged electrical conductivity and difference between modeled and observed electrical conductivities for a representative day in various hydrologic and water operations scenarios: (**A**) wet year with a small export flow to inflow ratio, (**B**) wet year with a large export flow to inflow ratio, (**C**) critically dry year with a typical export flow to inflow ratio, and (**D**) critically dry year with a large export flow to inflow ratio. In the maps on the left, we have bilinearly interpolated the electrical conductivity measured at different locations over the entire domain. In the maps on the right, we have subtracted the bilinearly interpolated observations from the bilinearly interpolated modeled electrical conductivities. In each figure, *arrows* on the Sacramento River and near the pumps indicate the average inflow and exports on that day. In the maps on the right, we indicate modeled electrical conductivities greater than those observed by *lighter colors*, and modeled electrical conductivities lower than those observed by *darker colors*. In all the plots, we represent the model configuration, G1T15B1, with best overall predictive skill.

lag between modeled and observed flows peaked away from the boundaries (Figures 11 and A-6.6). In the flow predictions, significant hysteresis occurred due to the poor prediction of the modulation of tidal amplitude by the river flow, which caused over- and under-predictions of the tidal signal in the interior Delta locations (represented by the elliptical annuli, or more scattered ellipses, respectively, in the correlation plots in Figures 11 and A-6.6). As we demonstrate in Section 5.3, this representation of tidal water level and flow with low fidelity is a direct consequence of the model's inaccurate representation of tidal effects.

5.3 Predictions of Tidal Effects

The primary purpose of DSM2 is to reproduce subtidal flow fields accurately to model the hydrodynamic transport of scalars and aquatic organisms of interest (Hutton 1995). As we discussed in Section 3.1 and in Appendix A, tidal effects are crucial to subtidal flow. The decomposition of total instantaneous flow and water levels into their tidal and subtidal components comprises tidal effects. We discuss (1) harmonic components and the spring–neap tidal range in water levels (Figures 14 and A-6.9) and flows (Figures 15 and A-6.10), and (2)

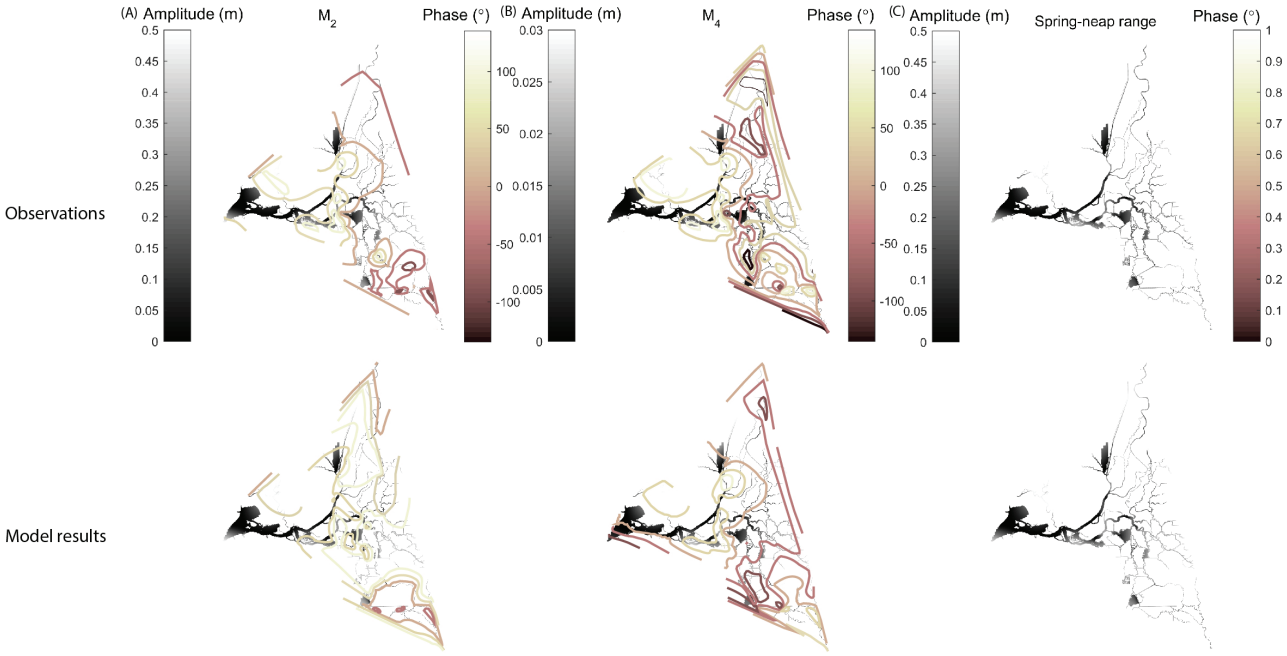

Figure 14 Observed and modeled average tidal decomposition of water column depth in the summer of a critically dry year (July to September 2015, with an average daily inflow of 275 m^3s^{-1} and an average export:inflow ratio of 0.15): tidal harmonic component amplitudes for (**A**) M_2, and (**B**) M_4, and (**C**) range in the spring–neap cycle. In each figure, the *gray levels* in the heat-maps indicate the water column depth; the *pink levels* in the contour lines indicate the tidal phase. The *scale bars* apply to both the top and bottom maps. Note that we have not reported the phase of the spring–neap oscillation, because the difference in tidal range was not estimated through harmonic analysis. In all the plots, we represent the model configuration, G1T15B1, with best overall predictive skill.

subtidal flow and Stokes' drift (Figures 15-17, and A-6.10, A-6.11).

We report on the subtidal flow field in the four hydrologic and water operation scenarios as we did for the electrical conductivity field in Section 5.2, as well as an additional period in winter 2014, which had low freshwater inflow and a typical export:inflow ratio (Figure 3). We report only the model's performance in predicting tidal components of hydrodynamic quantities in the summer of 2015, because the low inflow conditions represent the most stressful period for such models (e.g., Warner et al. 2005).

To evaluate tidal components of hydrodynamic quantities, we define amplitude interchangeably, depending on the context as that of either the water level or the flow. We also report the Greenwich phase of either quantity in degrees, to represent the effect of frictional retardation on wave propagation. For instance, an M_2 tide with a phase difference of 180° between two points indicates a 6-hour lag.

5.3.1 Tidal Water Levels

Although DSM2 qualitatively represented general tidal oscillatory patterns, there were inconsistencies in predictions at various locations within the Delta.

The observed dominant diurnal (K_1) and semi-diurnal (M_2) bands of astronomical components of water levels decayed rapidly landward (Figure 14A and A-6.9), while the overtides and compound tides spawned near the mouth of the Delta and intensified within the Delta (Figure 14B and A-6.9). These overtides and compound tides also intensified toward the eastern extent of the central Delta, but attenuated in the South Delta (Figure 14B and A-6.9). Moreover, propagation of the overtides and compound tides through the system became very complex (Figure 14B and A-6.9).

https://doi.org/10.15447/sfews.2018v16iss2art6

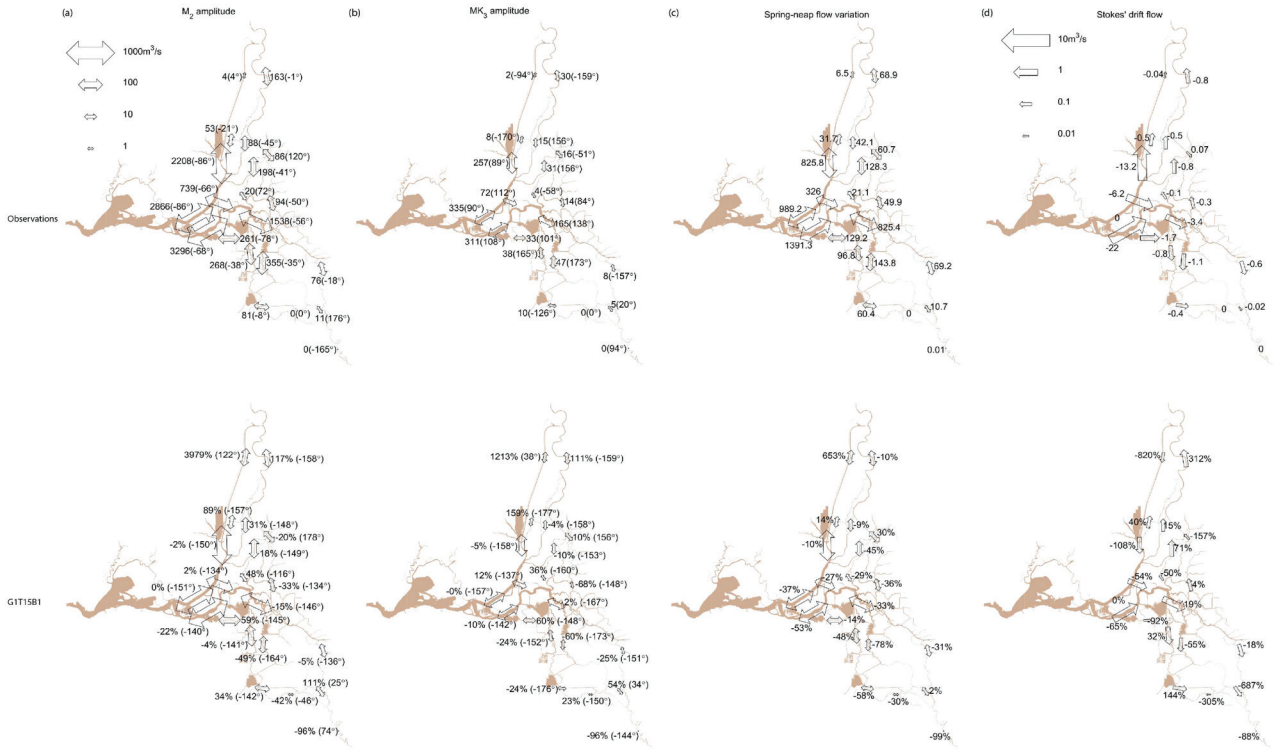

Figure 15 Observed and modeled tidal components of flow in a critically dry year (July to September, 2015, average daily inflow = 275 m^3s^{-1} and average export:inflow ratio = 0.15): (**A**) M_2, and (**B**) MK_3 harmonic components, (**C**) spring–neap cycle range, and (**D**) Stokes' drift. In the top row, arrow sizes correspond to observed amplitudes, and we indicate the amplitudes and Greenwich phases (within parentheses). In the bottom row, *arrow sizes* correspond to modeled amplitudes, and values indicate percentage differences between the modeled and observed amplitudes, and absolute difference in the Greenwich phase (within parentheses). We have sized the *arrows* on a logistic scale, and because the Stokes' drift is very small compared to the tidal harmonic amplitudes it is on a different scale. We represent the model configuration, G1T15B1, with best overall predictive skill.

The diurnal (semi-diurnal) components were retarded by almost 12 hours (6 hours) to 24 hours (12 hours) as the tides propagated into the North Delta, though they propagated without significant retardation in the central and South Delta (Figure A-6.9). This was a direct consequence of the higher inflow in the Sacramento River, and also because of lower friction in the deeper, dredged San Joaquin River. The higher-frequency, lower-wavenumber overtides also propagated faster into the Delta, because their phase velocities ($c = \frac{\omega}{k}$ where ω is the frequency of the constituent, and k is its wavenumber) are much higher than the phase velocities of the astronomical components (see Figure A-6.9).

The G1T15B1 model configuration was able to reproduce propagation patterns of the tidal harmonic components with highest fidelity (Figure 14 and A-6.9). However, the configurations with the Carquinez Strait extension were also able to match the observed patterns in the K_1 component reasonably well. All model configurations under-predicted the attenuation and retardation of the astronomical components from the tidal boundary into the system, and over-predicted the intensification and phase speed of the overtides and compound tides. This indicates a systematic bias toward under-damped wave motions.

The spring–neap oscillations in the tidal envelope were typically 0.3 to 0.5 m in the South Delta, while they were negligible in the North Delta (Figure 14C and Figure A-6.9). Only the G1T15B1, G1T15BB, and G2T5BB configurations at least qualitatively recovered this pattern (Figure A-6.10).

5.3.2 Tidal Flows

The amplitudes of the K_1 and M_2 components, respectively, decayed inland from about 1,000 m^3s^{-1} and 3,000 m^3s^{-1} to smaller than 100 m^3s^{-1} in the Sacramento and San Joaquin rivers (Figure 15A). The overtides and compound tides, which had about one-tenth the amplitude of the astronomical components, also decayed inland (Figure 15B). There was an approximately 15- to 45-minute phase lag in the Sacramento River compared to the San Joaquin River near Threemile Slough in all tidal components. The tidal range of the spring–neap variation in flow was comparable in magnitude to the K_1 amplitude (Figures 15C and A-6.10).

Although all the model configurations produced qualitatively identical results, the configurations with the domain extension predicted more accurate amplitudes and phasing of the astronomical tides than the other configurations in the western and central Delta (Figures 15 and A-6.10). In all the model configurations, the deviation in predicting the tidal harmonics and spring–neap variations increased inland (Figures 15C and A-6.10). The component flow estimates were the worst in the South Delta and in the Yolo Bypass, where the river flow influence is weak compared to the North Delta (Figures 15 and A-6.10). We could not draw any conclusions about the differences in predictive power between astronomical components and overtides and compound tides.

At critical junctions such as the DCC, the Head of Old River, and Threemile Slough, none of the model configurations predicted tidal flows accurately. This could have potential implications for predictions of transport and mixing, particularly by the PTM module. At the DCC, there was about 20–50% error in prediction of the amplitude of the M_2 component, and about 8–12 hours' lag in the prediction of its tidal phase (Figures 15B and A-6.10). Although the model predicted tidal flows in Threemile Slough with much higher fidelity (typically lower than 20% error), the phasing of flows in the Sacramento and San Joaquin rivers was often incorrect by 6–8 hours (Figures 15B and A-6.10). There was between 100% and 450% error in the prediction of the amplitude of the M_2 component, depending on the model configuration at the Head of Old River, and phase leads or lags of 4–10 hours occurred between the model results and observations (Figures 15B and A-6.10).

5.3.3 Subtidal Flows

The subtidal flow in the Sacramento and San Joaquin rivers was typically high in the high inflow periods, as expected (Figures 16A and A-6.11). There was a small, O (10 m^3s^{-1}), subtidal oceanward flow in the OMR corridor in the high-inflow period, which reversed during the other periods (Figure 16). The Stokes' drift flow was only about one-hundredth to one-tenth of the subtidal flow everywhere, and decayed rapidly in the landward direction (Figures 15D, 16, A-6.10, and A-6.11). Qualitatively, all the model configurations recovered these patterns. However, when the subtidal flows were small, the errors in predicting both the subtidal flows and the Stokes' drift were very large, sometimes exceeding a factor of ten. This trend was exacerbated in regions near the Stockton and Sacramento River deep water shipping channels, because of sudden bathymetric changes (Figures 15D and 16D).

In general, the model reproduced subtidal flow patterns, except in locations such as Jersey Point, Rio Vista, Garwood Bride, and in the OMR corridor. In these locations, the modification of the subtidal flow by tidal effects was strong, with significant deviation between modeled and observed subtidal flows (Figure 17). The fidelity at Garwood Bridge was particularly low because of a sudden rise in the channel bottom between the Stockton shipping channel and the San Joaquin River. This discontinuity, of about 9 m, caused almost a hundred-fold increase in frictional retardation of the propagating tidal wave, and reflected a significant portion of the energy contained on the progressive tidal wave into the shipping channel. These trends are consistent with the difference maps in Figures 16 and A-6.11. The poor predictions of subtidal flow near junctions with complicated tidal phasing such as Threemile Slough, the OMR corridor and near the DCC indicate that the likely source of the errors at such locations is the unmodeled complexity involved in tidal modification of subtidal flow from tidal asymmetries between ebb and flood dominant channels. This inference is supported by the

https://doi.org/10.15447/sfews.2018v16iss2art6

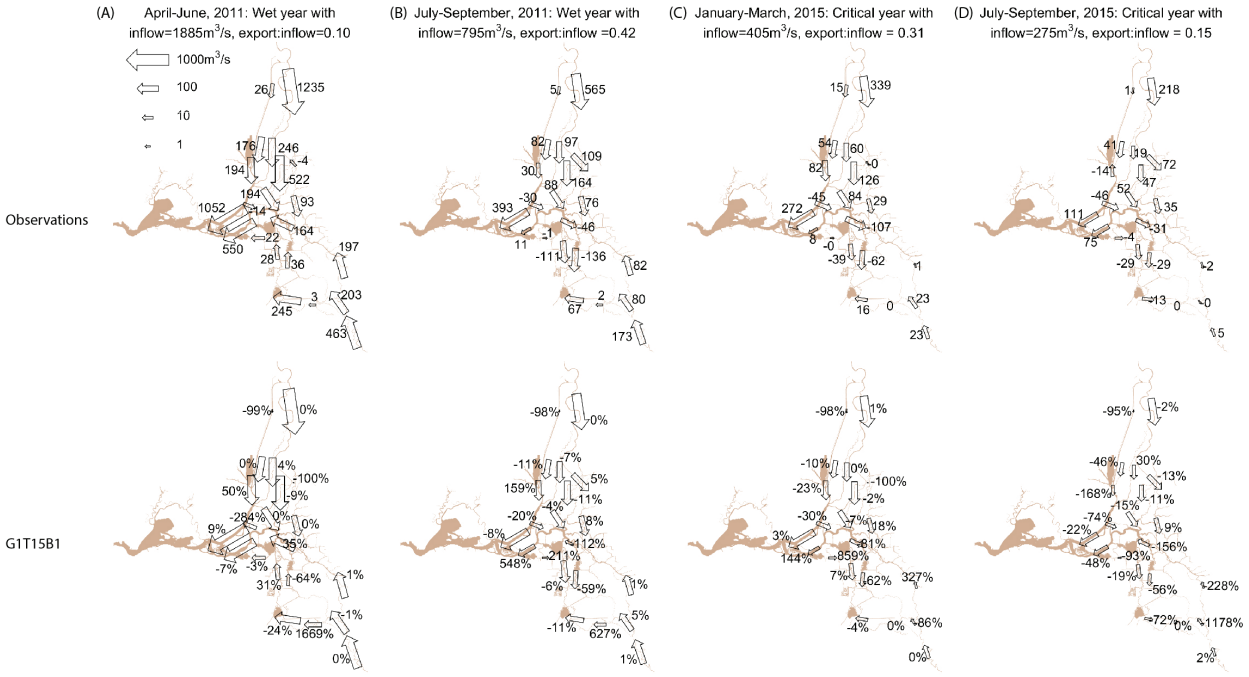

Figure 16 Observed average subtidal flow and difference between modeled and observed subtidal flow in various hydrologic scenarios: (**A**) spring in a wet year, (**B**) summer in a wet year, (**C**) winter in a critically dry year, and (**D**) summer in a critically dry year. In each season, we indicate the average daily inflow and the ratio of total export flows to total inflow. In the *top row*, we indicate the observed flows by *numbers and arrows*. In the *bottom row*, arrows sizes correspond to modeled flows, and values indicate percentage differences between the modeled and observed flows. We have sized the *arrows* on a logistic scale. We represent the model configuration, G1T15B1, with best overall predictive skill.

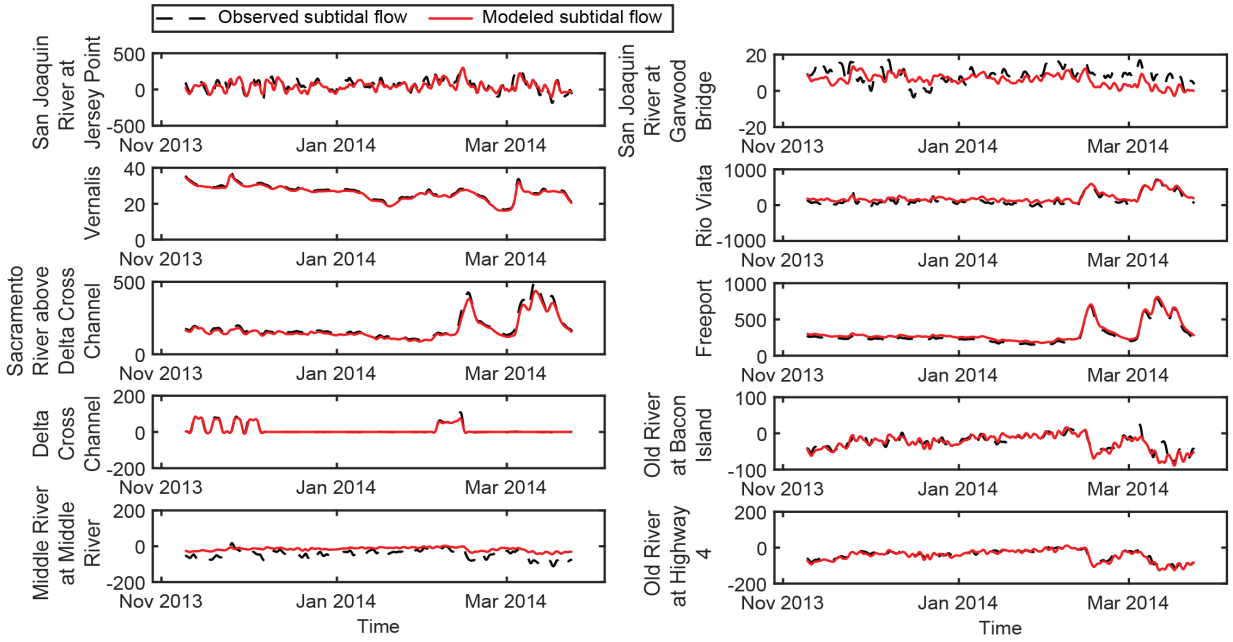

Figure 17 Comparison of observed and modeled subtidal flows (in m^3s^{-1}) at different locations. We show the results of the G1T60B1 model configuration with lowest aggregate error.

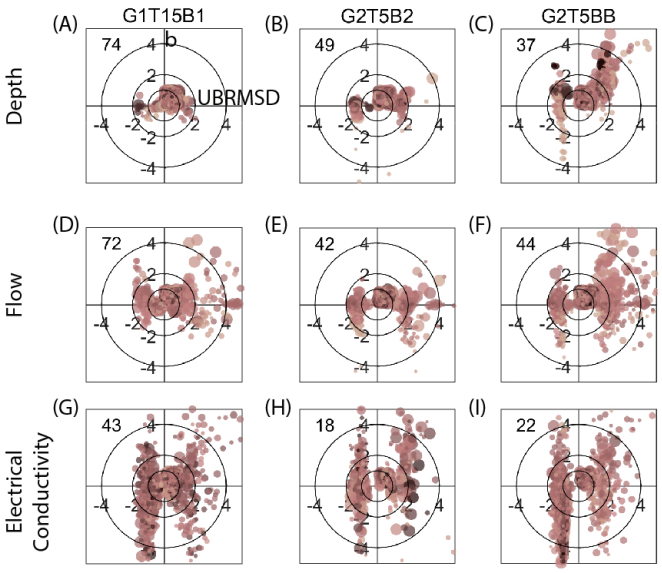

Figure 18 Unbiased RMS difference and bias between model results and observations for various model configurations in (**A–C**) instantaneous water column depth, (**D–F**) flow, and (**G–I**) daily averaged electrical conductivity. In each plot, we represent the unbiased RMS difference on the abscissa and the bias on the ordinate axes, colors lighter landward, and points bigger with increasing total inflow into the system. We also indicate circles of dimensionless radii 1, 2, and 4. The numbers indicate the percent of points that fall within the radius-1 circle. Note that the G1T15B1 and G2T5BB model configurations are favorably skewed by the wet years. For better readability, we have jittered points with model predictions within the data precision inside the radius-1 circle.

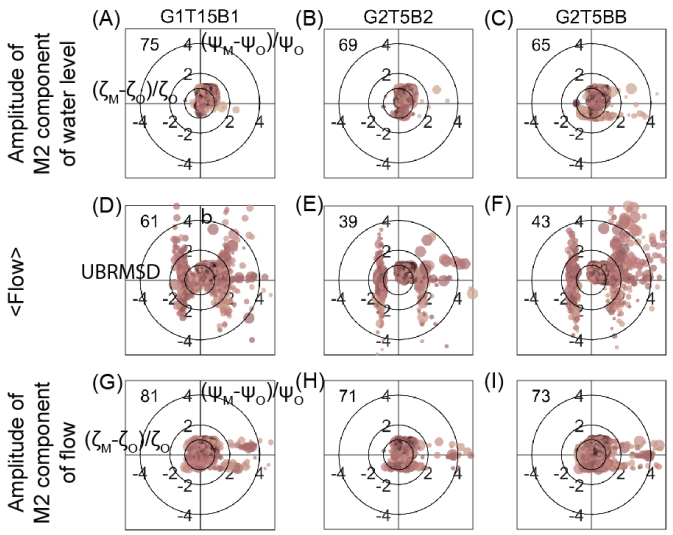

Figure 19 (**A–C**) Errors in amplitudes and phases of the M_2 component of water column depth and (**D–F**) flow, and (**G–I**) unbiased RMS difference and bias between model results and observations in the subtidal flow, for various model configurations. In each plot, we represent the unbiased RMS difference or error in amplitudes on the abscissa and the bias or error in phases on the ordinate axes, colors lighter landward, and points bigger with increasing total inflow into the system. We also indicate circles of dimensionless radii 1, 2, and 4. The numbers indicate the percent of points that fall within the radius-1 circle. Note that the G1T15B1 and G2T5BB model configurations are favorably skewed by the wet years. For better readability, we have jittered points with model predictions within the data precision inside the radius-1 circle.

importance of the Stokes' drift in this region, which was 30% of subtidal flow (Figures 15D and 16D).

These results indicate that DSM2 is reasonably well suited for predicting the subtidal flow, provided that the complex bathymetry at important junctions such as Threemile Slough, Georgiana Slough, Stockton shipping channel, and junctions in the OMR corridor are well resolved.

5.4 Target Diagrams

We display target diagrams of model performance for instantaneous quantities (Figures 18 and A-6.2 in Appendix A) and tidal and subtidal quantities (Figures 19 and A-6.3). In these diagrams, the points displayed indicate the performance in the phase space of either the RMS error and bias for instantaneous quantities, or the amplitude and phase errors for tidal quantities during various 3-month periods.

In Figures 18 and A-6.2, the model did not predict instantaneous water column depth and flow predictions well in the central Delta and OMR corridor. In the western Delta, the model predicted these quantities reasonably well. The model generally predicted electrical conductivity better in the rivers than in the brackish parts of the Delta. Moreover, points corresponding to periods of high freshwater inflow were generally associated with lower prediction errors. Based on these diagrams, the G1T15B1 model performed best, with almost 75% of the water column depths, 70% of the flows, and 45% of the electrical conductivities falling with the

https://doi.org/10.15447/sfews.2018v16iss2art6

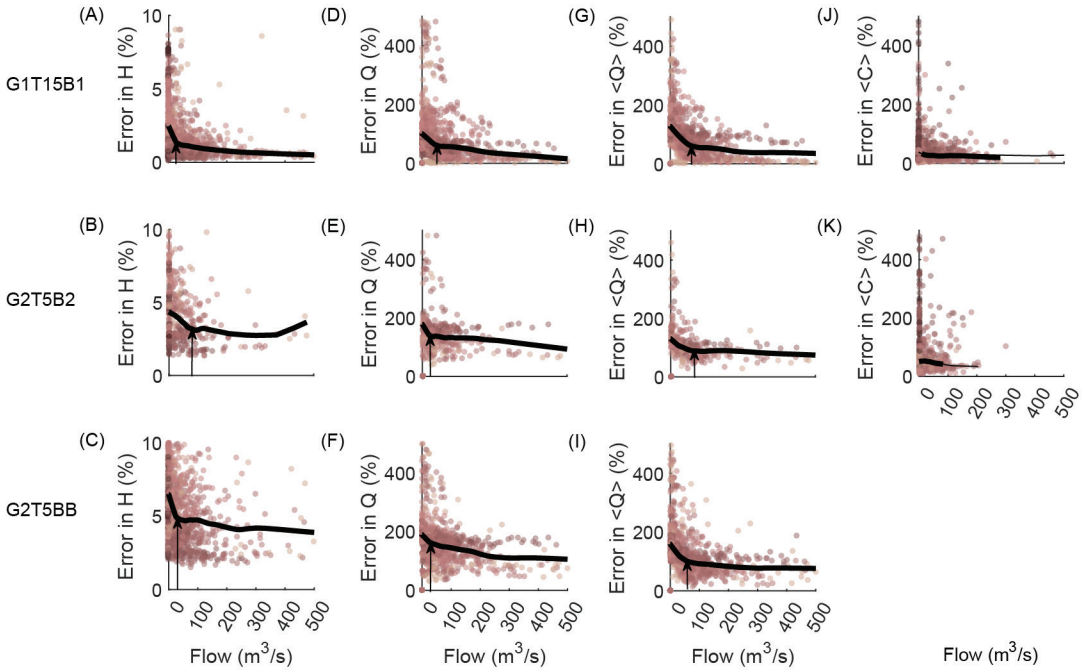

Figure 20 RMS error in (**A–C**) instantaneous water column depth and (**D–F**) flow, (**G–I**) subtidal flow and (**J–K**) daily averaged electrical conductivity as a fraction of the RMS values of these quantities versus the subtidal flow magnitude at various locations for different mode configurations. In each plot, we have colored the points lighter landward. We have also included a LOWESS regression with a bisquare interpolation and smoothing parameter of 0.6 to indicate the trends in the errors (*black line*). *Thick regions* of this line indicate statistically significant fits; *thin regions* indicate insignificant fits. In each figure, the *arrows* indicate the inflow at which the trend in model error flattens. Note that the G1T15B1 and G2T5BB model configurations are skewed by points that occur in wet years.

radius-1 circle. The models with the Carquinez Strait extension performed comparably with the other configurations.

In Figures 19 and A-6.3, the model generally predicted tidal and subtidal components of water column depth well in the western Delta, but not in the riverine regions. In addition, increasing freshwater flow resulted in better predictions of tidal and subtidal components of flow. Model configurations with the domain extension did not perform as poorly as we expected; a well-calibrated domain extension would, therefore, likely be valuable.

We show the trends in prediction errors with freshwater inflows into the system through LOWESS regression fits (Cleveland 1979) in Figure 20 using the MATLAB toolbox *lowess* (Burke 2012). In these fits, we deemed the fits to be statistically significant when the bootstrapped 95% credible intervals of the LOWESS estimate did not include the grand mean of the errors. The errors in predictions of water column depth and tidal and subtidal flows decreased sharply for all model configurations with increasing freshwater inflow into the Delta until about 50-100 m^3s^{-1} and then more gradually (Figures 20A–20H). The increase in error in flow predictions at very high inflows for model configuration G2T5B2 (Figure 20B) is an artifact of the small number of records during these conditions. Although there was a statistically significant decrease in errors in the prediction of daily averaged electrical conductivities with increasing flow, this relationship was much weaker than for water column depth and flow. We show these general trends for other model configurations as well in Figure A-6.4. The standard configuration as well as the finer-resolution grids and domain extensions produced similar error patterns with inflow (Figure 20).

From the target diagrams (Figures 18 and 19) and error response to freshwater inflow (Figure 20), it

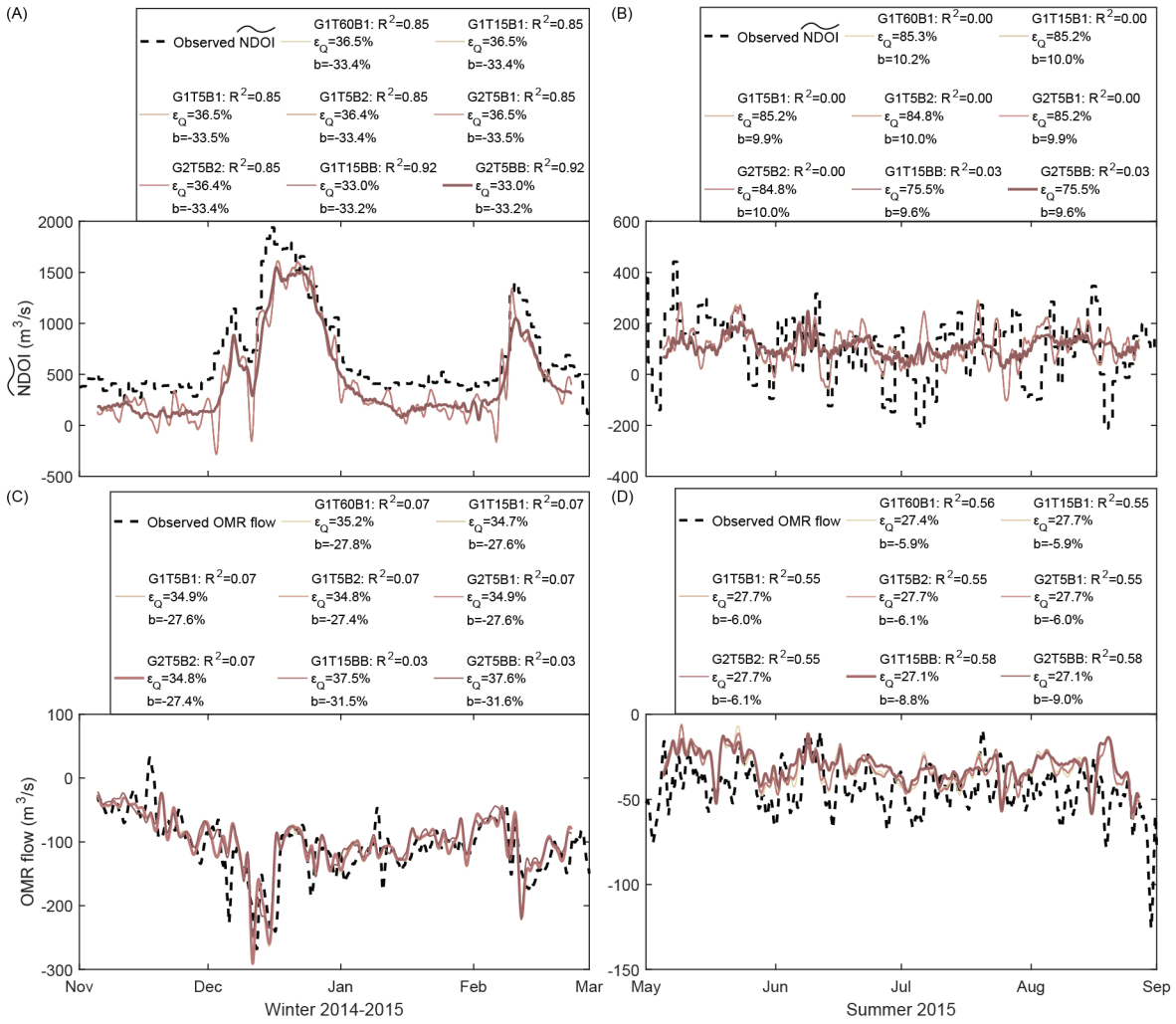

Figure 21 Estimated and modeled regulatory parameters in a wet and dry period: (**A**) and (**B**) Net Delta Outflow Index (NDOI), and (**C**) and (**D**) subtidal OMR flow. *Dashed black lines* indicates the observations of NDOI less the subtidal adjustments, $\widetilde{NDOI}$, in (**A**) and (**B**) and the subtidal OMR flows in (**C**) and (**D**). In each plot, we indicate R^2, RMS error, and bias for each model configuration. The prediction of regulatory parameters is generally poor, and significantly worse during periods with low inflow. The configuration with the Carquinez Strait domain extension and fine grid perform best in recovering the NDOI as well as OMR flows. In each figure, we indicate with a *thick line* the best-performing model configuration. Some lines are not visible because these model configurations produce results that are indistinguishable.

is evident that even with the many approximations in the model, DSM2 performs reasonably well. In the tidal reaches of the western Delta, it could even compete with more complex 3-D models such as UnTRIM (compare Figure 18 here with Figure 18 in MacWilliams et al. 2015).

5.5 Estimates of Regulatory Parameters

DSM2 is being used as a management aid for water operations in the Delta (Nam 2008, unreferenced, see "Notes"; Cavallo et al. 2015). Therefore, its ability to estimate regulatory parameters is of vital importance. Two important regulatory parameters that characterize the ecological health of the Delta and export pumping operations are, respectively, the NDOI, which measures the total outflow of the Delta (Monismith et al. 2002), and subtidal OMR flow, which measures the flow entrained toward the pumps (Kimmerer 2008).

https://doi.org/10.15447/sfews.2018v16iss2art6

In the computation of the $\widetilde{\text{NDOI}}$, Q_W typically contributed 5–20% of the flow, and contributed ±1–10% of Q_W (Figure 3G). During high inflows, all the model configurations reasonably predicted the trends in the $\widetilde{\text{NDOI}}$ (Figure 21A). However, in the period investigated, there was an almost 35% under-prediction of the $\widetilde{\text{NDOI}}$, and an error of about 35% in model results. Of all model configurations, the ones with the domain extension performed best. On the other hand, with decreasing freshwater inflow, the predictive power of the $\widetilde{\text{NDOI}}$ was significantly reduced (Figure 21B). During this period, none of the model configurations could predict the fortnightly filling and emptying of the Delta. However, given the poor precision in the NDOI during low outflows (Monismith 2016), it is unreasonable to expect good predictive power during such periods. In the wet period, the model configuration with fine bathymetry and $R \approx 1$ (G2T5B2) predicted the flow reversal in subtidal OMR flow with slightly lower bias (27.4%) and marginally higher R^2 (0.074) than other configurations, indicating that an improvement in bathymetric resolution with smaller time-step sizes in the central Delta could potentially improve model performance (Figure 21C). The error in model prediction and bias were, again, about 30%. Prediction of subtidal OMR flow improved slightly during low inflows, because of the relatively easy-to-simulate plug flow-like influence of the exports (Figure 21D).

Although DSM2 was able to predict the temporal patterns of key regulatory parameters during high inflow periods, its predictive power diminished during low inflow periods, partly from the unrepresented complex tidal physical processes that dominate the flow, and partly from poor precision in the data itself. However, the model did not accurately predict actual magnitudes of regulatory flows in *any* of the periods.

6. DISCUSSION

DSM2 performs well in predicting instantaneous hydrodynamic quantitates such as total water column depth, flow, and daily averaged electrical conductivity. However, predictions of tidal effects, subtidal flows, and regulatory flow parameters are less accurate because of various sources of error. In particular, flow splits and phasing of tides at critical junctions such as the DCC, the Head of Old River, and Threemile Slough are not predicted with high accuracy. When coupled with water quality and movement models such as Qual or PTM, these errors in predicting flow splits at important junctions can affect estimates of the routing proportions of scalars through these junctions.

We recommended and implemented several changes to model configurations. While none of these changes produced significantly different results overall, they nonetheless fundamentally changed the nature of the errors produced in the model. With rigorous calibration, the domain extension and finer grid and boundary condition resolution can enhance the performance of DSM2. We subsequently discuss the various sources of error in DSM2 and the performance of our proposals in Sections 6.1 and 6.2. In Section 6.2, we also discuss implementation of parameterizations of more complex physical processes than are currently represented in DSM2.

6.1 Errors in DSM2

Errors routinely appear in models because of (1) unresolved physical processes, (2) model representation, (3) numerical solution method, and (4) data availability and precision (Willmott 1981). The last source of unsystematic error can be very large, particularly during periods of very low freshwater inflow. While errors in the data cannot be addressed by a model, the first three sources of error must be addressed while balancing logistical issues such as computational speed overheads.

Of the instantaneous, subtidal, tidal harmonic, and subtidal adjustment quantities that we investigated in Section 5, the largest source of error [O(100%)] was in the subtidal and astronomical tidal harmonic component evaluations. Overtides and compound tides, and the subtidal adjustments to the NDOI, contributed about 10% of the error in computations. Even though the flows associated with subtidal adjustment are generally expected to be small in comparison with the tidal signal, they can sometimes become comparable in magnitude or even saturate the subtidal signal, particularly in dry periods (Figure 3G) (CDWR c2016; Monismith 2016). Hence, they should be taken into consideration

at all times. The Stokes' drift, because of its very small magnitude in comparison with subtidal and tidal flows, contributed only 1% toward the total error (Figures 14–16). This error distribution, along with the comparable magnitude of systematic and unsystematic errors (Figure 9), indicates that unmodeled physical processes are the dominant sources of error in DSM2.

Unresolved processes cause certain unavoidable errors in the model solution. For instance, during hind-cast simulations in which models such as DSM2 are driven by data, the models are, in effect, solving the incompressible 1-D momentum balance with boundary conditions that include the effects of subtidal adjustment as well. Hence, results from such models indirectly include subtidal adjustment flows as well. However, when used to forecast hydrodynamic conditions in estuaries with astronomical tides, such models will be unable to recover subtidal adjustments to the flow. This is not a model drawback per se, but rather a consequence of the nature of the calibration data sets. In addition, the subtle feedback between under-representation of complex estuarine tidal processes and calibration of the model to data that includes these processes (see Section 3.2) is a significant source of unavoidable unsystematic error. DSM2 has been calibrated with a Manning's n in each channel, and also by varying the channel cross-sectional geometries to best fit the observations (Nader–Tehrani 2001). In constraining the incomplete model to represent the complete set of physical processes in a calibration data set, various model elements such as the subgrid cross-sections and channel hydraulics have to become tuning parameters, and do not necessarily always reflect reality. These issues make diagnosing model errors and recommending improvements challenging. Errors resulting from unresolved physical processes cannot be minimized, therefore, without including some of these processes in the model.

On the other hand, certain processes cannot be resolved by a 1-D model at all. When freshwater inflows are low, tidal processes outlined in Section 3.1 and in Appendix A become very important. In such circumstances, unmodeled tidal processes contribute significantly to model error (compare the middle panels to the left panels in Figures 10–12). Another example is the estimation of salt flux in partially-mixed estuaries, which is complicated by the periodic nature of the stratification of such estuaries (see Section 3.1; Figures 4A and 4B; Simpson et al. 1990). Since DSM2 does not resolve the vertical structure of water density, it will not be able to resolve tidal variability in salt flux, but rather only its subtidal average. Moreover, it will be unable to resolve the component of the lateral salinity gradient between the shoals and channels that is attributable to the periodic stratification and suppression of vertical mixing.

Model representation—i.e., the specification of boundary conditions, grid size, and domain extent—is another source of error. Models such as DSM2 do not represent even the included physical processes as accurately as possible because of practical considerations such as manageable grids and domain extents. This drawback results in systematic errors that we can correct only by changing the model configuration. For instance, in DSM2, the abrupt end of the model grid at Martinez introduces a spurious reflection of the oceanward wave characteristic. This causes the systematic error in flow to increase here and, consequently, decay inland. But since the water column depth at Martinez is specified, the systematic error in water column depth is small here and increases landward. This results in an inverse correlation between systematic errors in the water column depth and the flow (Figure 9). On the other hand, systematic errors in hydrodynamic quantities should become uncorrelated if oceanward-propagating wave characteristics are allowed to radiate freely out of the domain (Figure 9F).

DSM2 is also unable to correctly resolve subtidal flows and tidal flow splits in regions with sudden bathymetric changes. In addition to the sudden bathymetric change at Stockton highlighted in Section 5.3.3, the natural sill in Carquinez Strait (Figures 7A–C) also decreases the tidal energy that propagates landward into the system compared to what the model predicts. Although bathymetric complexity is challenging for any model, 2-D and 3-D models can incorporate sudden shifts by resolving such features and by incorporating terrain-following coordinate systems, respectively (e.g., Fringer et al. 2006). In 1-D models, although we can make computational grids arbitrarily small, to

https://doi.org/10.15447/sfews.2018v16iss2art6

avoid large errors in solution propagation, we must also accordingly reduce time-step size (Ferziger and Periç 1997). In DSM2, increasing the grid resolution involves a significant recalibration effort, which is challenging. In DSM2, model representation errors are thus comparable in magnitude with unsystematic errors (Figures 9D–F and 9G–I).

A third source of error is the **numerical solution scheme**, which includes several linearizing approximations for the sake of practical considerations. These include simplifications of the friction term which are common in discretizations of the Saint-Vénant and shallow water equations in Equation 6 and allowances for smoothness of the temporal solution. Such approximations cause under-damping of tides and inaccuracies in the prediction of the water column depths. For example, in Figure 11, in the interior Delta locations the model over-predicts the tidal signal during the ebb phase of the tide (because of the constructive interaction of the reduced effect of bottom friction on both river and tidal flows) and under-predicts the tidal signal during the flood phase (because of the destructive interaction of reduced bottom friction effect on both river and tidal flows). Such under-damping occurs from various approximations. First, the shallow-water wave assumption causes the wave speed and water surface elevation of the tidal component of flow to be over-predicted (Chen 2005). Second, the semi-implicit Crank–Nicolson scheme damps harmonic components slowly (Ehle 1969), which results in stronger wave reflections landward in the model results. Accordingly, in the model results, the tidal wave at Martinez propagates almost as a standing wave inland past Chipps Island, rather than as a progressive wave. Third, the damping by friction is artificially small because of the large depths of the channels used to avoid the intermittent wetting and drying of the intertidal mudflats in Suisun Bay. Fourth, the stability of the model solution constrains the cross-sections to vary gradually, often with unrealistically steep side slopes (Smith and Enright 1995). This also decreases the frictional retardation of the tides and river flow. Fifth, the model ignores temporal variability in cross-sectional mixing caused by the subtidal adjustment component of flow in the western Delta. As a consequence, the model cannot reproduce the energetic flows and lower water surface elevations during the ebb phase of the tide, and the reduced mixing and increased water surface elevations during the flood phase of the tide (Simpson et al. 1990). In addition to these approximations, flows and water surface elevations are under-predicted as a consequence of the constant Manning's n values for each channel reach. Moreover, Hydro takes longer to respond to flow reversals. In reality, Manning's n does change with tide phase in the Delta, particularly in complex regions such as Threemile Slough (Fong et al. 2009).

Last, any model is only as effective as the **precision in the data** with which it is calibrated and validated. The uncharted water lateral withdrawals and agricultural runoffs together can account for about 10% of the total outflow from the Delta (Sridharan 2015). The unsystematic error from these data sources is large because of the unreliable information about these withdrawals on monthly time-scales. The DCDM is specifically being developed to address uncertainties in this data set. An example of significant uncertainty in the subtidal flow is in the NDOI, in which the strength of the tidal signal saturates the flow measurements because of the large salinity gradients in the western Delta (MacCready and Geyer 2010; Geyer and MacCready 2014). The precision in the NDOI estimates can be as large as 100% during low-outflow periods (Monismith 2016). These errors in the data cannot be attributed to model performance.

We discuss various ad hoc recommendations to address some of these issues below.

6.2 Recommendations to Improve DSM2 Performance

It may be possible to correct the errors listed in Section 6.1 by using sophisticated approaches like finite elements (Kolar et al. 1994; Dawson et al. 2006), or weighted stencils (Grotkop 1973; Dawson et al. 2006), accurate spatial discretization and temporal advection schemes (Garcia and Kahawita 1986; Louaked and Hanich 1998; Chua and Fringer 2011), and by modeling the different harmonic components explicitly (Levesque et al. 1979; Walters et al. 2013, Rayson et al. 2015). Such methods however, require a complete reworking of the underlying model.

Alternately, some of the schemes we outlined in Sections 1 and 4.3 could be adopted with recalibration to improve fidelity without greatly sacrificing speed and simplicity. For best results, temporal resolution of the tidal boundary condition and time-step size must be such that both the CFL condition and R should be O(1) (Sobey 2001). This would minimize error propagation into the domain from poorly-resolved boundary conditions. We could also extend the oceanward end of the domain to avoid the reflection of oceanward-propagating wave characteristics back into the domain at Martinez, and to allow for the water surface in the Delta to co-oscillate with long-term oscillations in the coastal ocean. In principle, the domain extension is equivalent to incorporating a "sponge layer" beyond the western end of the domain where the oceanward characteristics of waves are damped (Israeli 1981). Simulation quality has been improved significantly in the past with such domain extensions (e.g., Levesque et al. 1979; Sobey 2001; Dawson et al. 2006). In particular, Chua and Fringer (2011) and Holleman and Stacey (2014) used idealized versions of the Sacramento and San Joaquin rivers when they modeled the San Francisco Bay–Delta system. CDWR itself attempted to include an idealized version of the Bay, in which they treated the north Bay as a series of channels, the central Bay as a set of interconnected channels oriented to represent the observed circulation patterns and littoral reservoirs, and the south Bay as a reservoir (Ferreira and Sandhu 2016). However, that attempt was only marginally successful in reproducing the electrical conductivity at Martinez, and the extended grid is still being refined (Sandhu 2018, unreferenced, see "Notes").

Here, we added a representation of Carquinez Strait to the DSM2 grid, so that the 2-D and 3-D hydrodynamic complexities of the Bay could be circumvented while the oceanward characteristic of the tidal wave, and other evanescent overtidal and compound tidal waves, were still allowed to radiate for a few kilometers past Martinez. Even this small extension produced promising results. The behavior of the systematic error (Figure 9F versus Figures 9D–E) indicates that the domain extension allows tidal energy to radiate oceanward. The domain extension also resulted in minor improvements in the prediction of tidal and subtidal components of flow in the western Delta (Figures 15 and 16). In addition, the finely-resolved grid produced marginal improvements in the prediction of subtidal OMR flows (Figure 21). These outcomes suggest that these recommendations would likely improve model fidelity significantly if they were implemented with a thorough recalibration.

Subtidal adjustment flows and estuarine circulation processes cannot be represented in DSM2 and have to be parameterized. In particular, shoal–channel interactions and the wetting and drying of mudflats can be parameterized straightforwardly in DSM2. Shoal–channel systems and intertidal mudflats are currently represented as single channels with subgrid cross-sections that change rapidly with increasing elevation in DSM2. Such a representation (1) does not allow shoal–channel salinity differences and exchanges to be well represented, and (2) can result in instabilities that arise in the solution at cross-sections that have embayments or shoals because of a sudden decrease in conveyance with increasing water column depth.

Our idealized shoal–channel representation resulted in very low flow through the shoal while the tidal energy dynamics of the main channel and shoal were preserved (see "Prescriptions for Model Recommendations" on page 5 in Appendix A). It was very effective in qualitatively recovering the salinity structure during the flood and ebb phases of the tide at a station 7,500 m from the landward end of the domain and 2,500 m from the ocean end (Figure 22A). First, flow in the shoals was significantly slower than flow in the channel and was lagged by about 10 hours. Second, typical flood-phase salinities in the channel and shoals of about 14 psu and 7.5 psu, respectively, and typical ebb-phase salinities in the channel and shoals of about 8.5 psu and 7 psu, respectively, compared qualitatively with the cross-sectional distribution of salinity shown in flood and ebb snapshots in Figures 7 and 8 in Ralston and Stacey (2005). The asymmetry in salinity between the ebb and flood phases was due to the relatively small longitudinal dispersion; saline pulses effectively moved past the observation point without mixing relatively quickly during the flood phase. As salinity mixed over the tidal cycle, ebb salinity was lower over a longer duration. Quantitative discrepancies between our results and

https://doi.org/10.15447/sfews.2018v16iss2art6

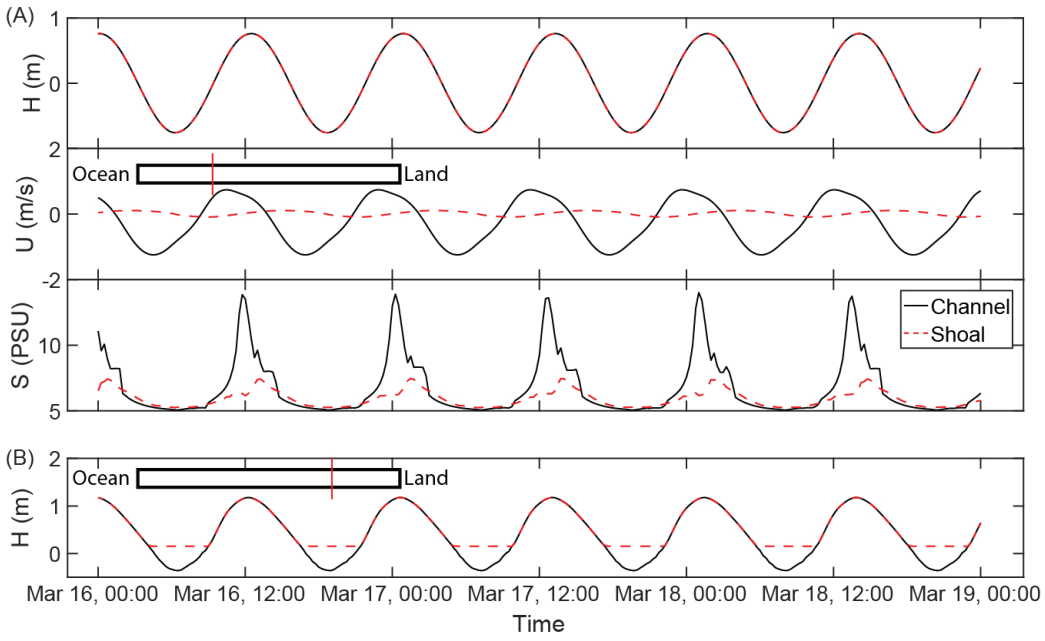

Figure 22 Results of the idealized shoal–channel problem: (**A**) shoal–channel exchange problem modeled after Ralston and Stacey (2005), and (**B**) wetting and drying simulation. The main-channel is 50 m wide, and the shoals are 375 m wide and are elevated 1 m above the main-channel bottom. The insets indicate the location of the station at which we plot the results in each case. In (a), $\eta_0 = 0.75$m, $Q_R = 28.3$ m^{3}s^{-1}, $n_{Channel} = 0.01$, and $n_{Shoal} = 0.1$. In (b), $\eta_0 = 1.5$m, $Q_R = 4.5$ m^{3}s^{-1}, $n_{Channel} = 0.02$, and $n_{Shoal} = 0.035$.

those of Ralston and Stacey (2005) likely result from minor differences in implementation of the landward boundary, as well as fundamental differences between a full 3-D circulation model and a 1-D model. In addition, we were also able to recover the intermittent drying of the shoals (Figure 22B). Because intertidal mudflats in the Delta are brackish, the small quantity of salt in the 3 cm of water left in the shoals during each ebb period is acceptable (Uncles and Peterson 1996). A parameterization like this one could stabilize the solution when conveyance increases suddenly with elevation (see "Derivations of Subtidal Adjustment Process Expressions" on page 3 Appendix A). More important, accurately representing the dynamics of shoal–channel systems is crucial in informing ecosystem restoration efforts that are often focused on the littoral regions around tidal channels and marshes (Luoma et al. 2015).

We subsequently describe certain recommendations we did not evaluate, because their implementation would require a significant recoding of the model and recalibration (and such an effort was beyond the scope of this work), but which we believe are nonetheless useful additions.

Of the various effects of wind-driven flows (see Section 3.1), only the net exchange flow from the water surface set-up can be incorporated into a 1-D model. Based on Monismith's (2016) analysis, we can approximate this flow using Equation 3. However, the relationship in Equation A-2.2 (see "Derivations of Subtidal Adjustment Process Expressions" on page 3 in Appendix A) between the water surface set-up and the wind shear at Pittsburg was derived only for the summer of 2015 (Monismith 2016). This is likely to dynamically change with changing hydrology and atmospheric conditions. Having noted this caveat, we could proceed by specifying this as a uniform boundary flow at Martinez given a forecast of U_W.

A model such as DSM2 cannot resolve density driven currents due to the lack of coupling between the Saint–Vénant and the transport equations. A simple fix to incorporate density-driven currents could be to normalize Q_S from Equation 4 by the flow in a particular channel as

$$Q_{S,i} = \frac{Q_i}{NDOI} Q_S \tag{14}$$

where, Q_i is the flow at a time-step in the i^{th} channel. $Q_{S,i}$ could then be added to the flow computed in each channel. This type of fix only adds an average gravitational circulation component of opposite sign to both tidal flood and ebb phase flows, and does not resolve the spatial and temporal structure of the circulation. However, as shown in Figure 22, such a correction produces somewhat reasonable results. When used to forecast the hydrodynamics of the Delta with predicted tidal water level and flow boundary conditions, parameterized boundary conditions according to Equations 4 and 14 due to the subtidal adjustment could be specified explicitly in DSM2 to improve fidelity.

Although the numerical solution scheme in DSM2 is as sophisticated as possible for the FourPt stencil (DeLong et al. 1997), some of the linearizations in the model could be adjusted with some effort. Incorporating a more accurate friction term involves changes to the FourPt scheme and invoking higher-order terms that are different for different harmonic components (e.g., see Sinha and Pingree [1997]). Alternately, the Manning's n values for each channel could be prescribed to vary temporally using a look-up table for each channel that could be calibrated as described below to the dominant M_2 tide. Equating the conveyance defined as (Jarrett 1984)

$$K = \frac{1.49 A R_H^{2/3}}{n} \tag{15}$$

with

$$K = \sqrt{\frac{gH}{rC_D}} A \tag{16}$$

where r is the frictional retardation and C_D is the drag coefficient, we can write

$$n = 0.024 \frac{R_H^{2/3}}{\sqrt{H}} \tag{17}$$

where, $R_H\left(\frac{\beta W + H + \eta}{\beta W + 2H + 2\eta}\right)(H + \eta)$ is given for the reasonable approximation of a trapezoidal channel cross-section with gentle side slopes, β, for the horizontal. From Equation 17, n could be averaged over multiple tidal cycles to give its ebb- and flood-phase values. Freidrichs and Aubrey (1994) showed that the drag coefficient varies by at least an order of magnitude over the tidal cycle, just as Fong et al. (2009) observed in the Delta. So this factor could be important in resolving harmonic components more accurately.

We have shown that, of the three types of controllable errors in a model such as DSM2, it is relatively straightforward to minimize errors from model representation, and that with creative employment of approximations from the literature, it is possible to incorporate key 3-D physical processes into the modeling framework itself. Reducing errors from numerical approximations requires additional coding effort. Although our recommendations did not significantly improve model results in their current form, we expect that incorporating them with proper calibration would prove useful both in improving model accuracy and enhancing its usefulness as a decision support tool.

7. CONCLUSIONS

In this paper, we evaluated the performance of DSM2, which is used to model flows in the Delta. We note that the model performs well for the type of flow it has been calibrated for: total flows and water column depths. We also note its predictions of tidal flows could be improved so that it can become a more reliable decision support tool. To evaluate the model's fidelity, we developed a comprehensive model-evaluation protocol with which we assessed aggregate model performance for different model configurations, analyzed various error sources, and evaluated predictions of different components of hydrodynamic quantities computed by the model. We recommended and evaluated several simple ad hoc schemes to improve model performance. Although these recommendations require thorough calibration to be useful, they nonetheless influenced systematic errors in the model results in an encouraging manner. It is a testament to the exhaustive and painstaking calibration that has been performed on the model (CH2M Hill 2009; CDWR c2011; Liu and Ateljevich 2011; Liu et al. 2012) that its standard configurations produce the best overall results.

https://doi.org/10.15447/sfews.2018v16iss2art6

DSM2 reproduces total tidal flows and water column depths accurately, and daily averaged electrical conductivities reasonably well, particularly when freshwater inflows are high. It is commendable that a 1-D model of such a complex system is able to reproduce general spatio-temporal patterns in subtidal hydrodynamics, the non-stationary nature of the tides, and the generation and propagation of overtides and compound tides with the fidelity we observed. We note that, in the Delta, DSM2 is likely to perform comparably with models such as SUNTANS without subgrid bathymetry (Chua and Fringer 2011), SCHISM (Chao et al. 2017), and DELFT-3D (Martyr–Koller et al. 2017) in resolving 1-D flow dynamics. In regions where the physical processes not captured by DSM2 become important, only 3-D models such as UnTRIM that include subgrid resolution (MacWilliams et al. 2015) are likely to outperform DSM2. This is attributable to the extensive calibration of DSM2, and demonstrates that simple models such as DSM2 still have an important role to play in our understanding of the general hydrologic patterns of engineered surface water systems. Except in locations where bathymetric changes are sudden, the model also reproduces subtidal flow components such as river flow, tidal modulation of the river flow, and Stokes' drift well. DSM2 is able to reproduce the NDOI with reasonable accuracy, and hence its extensive use to inform water management—at least for outflow allocations—is well justified.

On the other hand, DSM2 is unable to reproduce the harmonic components of tide and subtidal flows modified by tidal signal accurately in regions where bathymetry is complex, tidal and river flow influences are comparable, and flow pathways are complex because of channel junctions. As we discussed in Sections 6.1 and 6.2, for fidelity to improve significantly, incorporating a finer grid would require an additional calibration effort. In this sense, DSM2 is closer in spirit to a physical model than a numerical one.

DMS2 is only reasonably well suited for the management purposes for which it is most commonly used—i.e., modeling daily flows to inform water quality and pumping operation-related actions. This is because, although it is able to reproduce the NDOI reasonably well, it is not able to reproduce OMR flows well. In addition, as Qual has been calibrated to daily averaged electrical conductivities, and because gravitational circulation processes cannot be incorporated into DSM2, we cannot represent dynamically changing salinity fields at sub-daily time-scales, particularly in the tidal reaches of the Delta where stratification occurs. Although we did not report on PTM in this study, its most significant shortcoming is in its representation of channel junctions as fully randomizing mixers, which disrupts the chaotic nature of particle movements across several junctions (Sridharan 2015; Sridharan et al. 2018).

Reasons for the inaccuracies in DSM2 primarily include: (1) unmodeled physical processes, which are particularly exacerbated when freshwater inflows are low and tidal dynamics are important, (2) mismatched and coarse spatial resolution of the grid and temporal resolution of the tidal boundary condition, and mis-specification of the model domain, which smooth the propagation of tidal information through the domain and cause systematic errors to propagate through the domain, (3) approximations in the numerical implementation of the model that under-damp tidal movements, and (4) imprecise and incomplete data that is used to calibrate and validate the model.

Rather than totally redesign the model, we suggested several ad hoc schemes that could augment it. The most straightforward strategy is to improve temporal resolution of boundary conditions and include subgrid bathymetry, and interpolate this to a spatial resolution that supports a CFL condition and resolution criterion of about 1. A domain extension to allow free propagation of the oceanward tidal wave characteristic, and utilizing a conveyance method that does not produce negative conveyance when wetting and drying occurs, are also promising improvements. However, even these simple improvements require significant re-calibration efforts.

Although reducing unsystematic model errors may be impossible beyond a certain extent in DSM2, it may be possible to employ machine learning techniques to identify spatial and temporal patterns in errors such as those shown in Figures 10–17 and model them non-parametrically. These modeled errors could then be removed from the Hydro solution to produce a corrected solution at each time-step. The schemes suggested in Section 6.2 and above are equally

applicable to similar 1-D models as well, and in some cases may be applicable to 2-D models too.

When deploying the improvements suggested in this study, three issues must be considered. First, run-time increases almost 10-fold when the time step-size is reduced from 60 minutes to 5 minute. Second, improving the spatial resolution of the grid must be concordant with restricting the CFL condition and resolution criterion. Third, the availability and quality of observations limits our ability to validate the model.

Of these, data availability may be the most challenging open-ended problem in the Delta. For instance, the coarseness of uncharted water withdrawals is not a model drawback but reflects data limitations. In cases like this, it may not even be physically or legally viable to collect more accurate data (Monismith 2016). There is also significant uncertainty in the measurement of Delta outflow because the strength of the tidal signal saturates flow measurements in the western Delta. Spatial heterogeneity in data availability can also introduce spatial patterns in fidelity. For example, although numerous stations throughout the Delta resolve electrical conductivity spatially, only five out of twelve stations measure water level and flow in the western Delta, and those too, only in Suisun Marsh. Similarly, of the 29 monitoring stations in the OMR corridor, only 18 measure water level, and that too, sporadically in time (Figure 1). Electrical conductivity measurements in the central Delta are often imprecise as well (2018 in-person conversation between E. Ateljevich and V.K. Sridharan, unreferenced, see "Notes"). Modelers must be content in the knowledge that with improving field technologies and accumulated experience over time come improved models.

The model-evaluation protocol developed herein may be used as a basis for performing similar analyses for other hydrological regimes. The complicated flow-course topology in the Delta—with multiple branched interconnected channels—makes traditional aggregate performance-evaluation techniques challenging to apply. For example, Ganju et al. (2016) list two combined skill-assessment techniques developed by other authors; however, these metrics required that the data sets used to compare the model against were qualitatively similar and spread uniformly in space. Ideally, if both flow and water level observations are available at identical locations, total observed and predicted hydraulic heads can be compared. Unfortunately, this too is not the case in the Delta. To overcome these difficulties, we developed aggregate error and skill metrics unique to such distributed flow systems. In addition, although the target diagrams MacWilliams et al. (2015) uses are adequate to evaluate instantaneous flows, water column depths and salinities, we developed new target diagrams to evaluate the tidal components of hydrodynamic quantities.

We have comprehensively evaluated the DSM2 model, and investigated the reasons for its behavior. We have also outlined and tested several ad hoc recommendations based on experiences with similar models reported in the literature. We believe that with comprehensive recalibration, the implementation of these recommendations in *DSM2* is straightforward, and that they would add immense value to the modeling of—and management efforts in—systems such as the Delta.

ACKNOWLEDGEMENTS

The authors acknowledge the funding received from the United States Bureau of Reclamation, the National Marine Fisheries Service (NMFS), the California Department of Water Resources (CDWR), and the Leawell Fellowship for the Sustainable Built Environment at Stanford University. We also thank CDWR for permitting the use of their model for this study. We are grateful to the National Oceanic and Atmospheric Administration's Tides and Currents service, the Romburg Tiburon Center, and the Interagency Ecological Program for the use of their data to quantify the model's accuracy. We are grateful to Dr. David Ralston and Prof. Mark Stacey for permitting the use of their model configuration and results in studying the merits of some recommendations in this paper. The lead author also personally acknowledges Dr. Min Yu at CDWR for supplying the standard DSM2 model configuration and input files required to run the model; Dr. Lynn Dewitt at the Environmental Research Division of NMFS and Ms. Swetha Madhur Kumar at the University of California, Santa Cruz, for assisting

https://doi.org/10.15447/sfews.2018v16iss2art6

with data acquisition; Dr. Miles Daniels for his inputs into the presentation in this manuscript; and the NMFS for the use of their computing resources to perform the numerical simulations used in this study. The quality of this manuscript has been immensely improved by the insightful recommendations of Drs. Peter Dudley, Eric Danner, and Steven Lindley at NMFS; three anonymous reviewers; and the sagacious advice of the Editor-in-Chief, Dr. Samuel Luoma.

LIST OF SYMBOLS

A cross-sectional area (m^2)

ASB surface area of Suisun Bay (m^2)

c wave phase speed (ms^1)

C electrical conductivity ($Scm-^1$)

C_D channel bottom drag coefficient (–)

$C_{D,W}$ drag coefficient at the air–water interface (–)

CFL Courant–Freidrichs–Lewy condition (–)

C_0 reference specific conductance of water at 25° C (Scm^{-1})

Fr freshwater Froude number (–)

Fr_W water surface set-up Froude number (–)

f_M instantaneous value of a modeled tidal harmonic

f_0 instantaneous value of an observed tidal harmonic

g acceleration from gravity (ms^{-2})

H water column depth (m)

J_i constants in the conversion of salinity to electrical conductivity (–)

K conveyance (m^3s^{-1}),

k wavenumber (m^{-1})

K_x longitudinal shear flow dispersion coefficient (m^2s^{-1})

K_i constants in the conversion of electrical conductivity to salinity (–)

L_{SB} length of Suisun Bay (m)

l_i integral length scale of mixing (m)

n Gauckler–Manning coefficient ($sm^{-1/3}$)

M number of time-steps in 1 day (–)

M_{Mix} estuarine mixing number (–)

$M_{SS\Sigma}$ aggregate model skill score (–)

N_0 buoyancy frequency (s^{-1})

N_ϕ number of locations where the quantity ϕ is observed (–)

$N_{\phi,i}$ number of locations at which the quantity ϕ is observed and which are correlated with the observations at location i (–)

NDOI Net Delta Outflow Index (m^3s^{-1})

$\widetilde{\text{NDOI}}$ Net Delta Outflow Index including subtidal adjustment flows (m^3s^{-1})

Q total flow through a cross-section (m^3s^{-1})

p a particular model configuration

PE_ϕ potential error in model

q total lateral flows into or out of a channel (m^2s^{-1})

Q_{DSJ} flow in Dutch slough (m^3s^{-1})

Q_{NDOI} modeled Net Delta Outflow Index (m^3s^{-1})

Q_{OMR} flow in the OMR corridor (m^3s^{-1})

Q_R river flow (m^3s^{-1})

Q_S subtidal flow induced by gravitational circulation (m^3s^{-1})

Q_{SD} subtidal flow induced due to Stokes' drift (m^3s^{-1})

Q_{SJJ} flow at Jersey Point (m^3s^{-1})

Q_{SRV} flow at Rio Vista (m^3s^{-1})

Q_{TSL} flow in Threemile Slough (m^3s^{-1})

Q_W subtidal flow induced by wind-driven circulation (m^3s^{-1})

R^2 coefficient of determination (–)

r friction retardation (ms^{-1})

R_H hydraulic radius (m)

S_{Ocean} ocean salinity (psu^{-1})

SSP Surface Similarity Parameter (–)

T tidal period (s)

t time (s)

Δt time-step size (s)

Δt_{BC} boundary condition temporal resolution (s)

u speed of information propagation on a numerical grid (ms^{-1})

U mean cross-sectional streamwise velocity ($m\text{-}s^{-1}$)

U_W wind speed at 10 m above the water surface at Pittsburg (ms^{-1})
u_η streamwise tidal velocity at the water surface (ms^{-1})
u_* friction velocity (ms^{-1})
S salinity (psu)
W width in a cross-section at an elevation (m)
WP wetted perimeter (m)
x distance along a river (m)
Δx grid size (m)
X_2 location landward from the Golden Gate where the salinity is 2 psu (m)
Z elevation in a cross-section (m)
z vertical distance from channel bottom (m)
β cross-sectional side slope (–)
β_0 intercept in ordinary least squares fit between model results and observations
β_1 slope of ordinary least squares fit between model results and observations
γ expansivity of salt (psu^{-1})
ε_s systematic model error
ε_u unsystematic model error
ε_Σ aggregate model error
ε_ϕ cumulative RMS error in computation of
ζ_M modeled amplitude of a tidal harmonic
ζ_O observed amplitude of a tidal harmonic
η water surface elevation (m)
η_W water surface set-up anomaly from the wind (m)
ρ_0 reference density of water (Kgm^{-3})
ρ_A density of air (Kgm^{-3})
$\mu_{\varepsilon\phi,x}$ mean overall error across model configurations
$\sigma_{\varepsilon\phi,x}$ standard deviation in overall error across model configurations
τ_W shear stress at air-water interface (Nm^2)
ϕ any quantity
ϕ_M modeled value of a quantity
ϕ_O observed value of a quantity
φ phase (°)
ψ_M modeled Greenwich phase of a tidal harmonic component (°)
ψ_O observed Greenwich phase of a tidal harmonic component (°)
ω tidal frequency (s_ε^1)

REFERENCES

Anderson J, Mierzwa M. 2002. DSM2 tutorial, an introduction to the Delta Simulation Model II (DSM2). Sacramento (CA): California Department of Water Resources, Office of State Water Project Planning, Modeling Support Branch, Delta Modeling Section. Draft DSM2 Tutorial [Internet]. [cited 2017 April 6]; 175 p. Available from: *http://baydeltaoffice.water.ca.gov/modeling/deltamodeling/models/DSM2v6/DSM2tutorialv122502.pdf*

Atkinson T, Davis P. 2000. Longitudinal dispersion in natural channels: 1. Experimental results from the river Severn, U.K, Hydrol Earth Sys Sci [Internet]. [cited 2017 April 6];4:345-353. Available from: *https://hal-sde.archives-ouvertes.fr/hal-00304668/*

Barnard PL, Schoellhamer DH, Jaffe BE, McKee LJ. 2013. Sediment transport in the San Francisco Bay coastal system: an overview. Mar Geol [Internet]. [cited 2018 January 30];345:3-17. Available from: *https://www.sciencedirect.com/science/article/pii/S0025322713000376 https://doi.org/https://doi.org/10.1016/j.margeo.2013.04.005*

BDO: Bay Delta Office [Internet]. c2002. Sacramento (CA): DSM2 grid version 2.0; [updated 2013 November 1; cited 2017 April 6]. Available from: *http://baydeltaoffice.water.ca.gov/modeling/deltamodeling/models/DSM2v6/DSM2_Grid2.0.pdf*

BDO: Bay Delta Office [Internet]. c2018. Sacramento (CA): Temporary barriers operating schedule; [updated 2018 January 19; cited 2018 January 19]. Available from: *http://baydeltaoffice.water.ca.gov/sdb/tbp/web_pg/tempbsch.cfm*

https://doi.org/10.15447/sfews.2018v16iss2art6

Becherer J, Flöser G, Umlauf L, Burchard H. 2016. Estuarine circulation versus tidal pumping: Sediment transport in a well-mixed tidal inlet. J Geophys Res Oceans [Internet]. [cited 2018 February 1];121(8):6251-6270. Available from: *http://onlinelibrary.wiley.com/doi/10.1002/2016JC011640/full* *https://doi.org/10.1002/2016JC011640*

Bennett WA, Burau JR. 2015. Riders on the storm: selective tidal movements facilitate the spawning migration of threatened Delta Smelt in the San Francisco Estuary. Estuary Coast [Internet]. [cited 2018 Macrh 16];38(3):826-35. Available from: *https://link.springer.com/article/10.1007/s12237-014-9877-3* *https://doi.org/10.1007/s12237-014-9877-3*

Benjankar R, Tonina D, McKean J. 2015. One-dimensional and two-dimensional hydrodynamic modeling derived flow properties: impact on aquatic habitat quality predictions. Earth Surf Process Landforms [Internet]. [cited 2017 April 6];40(3):340-356. Available from: *http://onlinelibrary.wiley.com.oca.ucsc.edu/doi/10.1002/esp.3637/full* *https://doi.org/10.1002/esp.3637*

Brandes PL, McLain JS. 2000. Juvenile Chinook salmon abundance, distribution, and survival in the Sacramento-San Joaquin Estuary. Stockton (CA): California Department of Fish and Game. p. 1-100.

Brunner GW. 1995. HEC-RAS River Analysis System. Hydraulic Reference Manual. Version 1.0. Davis (CA): Hydrologic Engineering Center. Technical Report ADA311952 [Internet]. [cited 2017 April 6]; 143 p. Available from: *http://www.dtic.mil/cgi-bin/GetTRDoc?Location=U2&doc=GetTRDoc.pdf&AD=ADA311952*

Brunner GW. 2003. Dam and levee breaching with HEC-RAS. Proceedings of the World Water & Environmental Resources Congress 2003; 2003; p. 1-9. Available from: *http://ascelibrary.org.oca.ucsc.edu/doi/abs/10.1061/40685%282003%2949*

Brunner GW. 2016. HEC-RAS river analysis system: 2d Modeling User's Manual Version 5.0. Davis (CA): Hydrologic Engineering Center, United States Army Corps of Engineers [Internet]. [cited 2018 January 22]; 171 p. Available from: *http://www.hec.usace.army.mil/software/hec-ras/documentation/HEC-RAS%205.0%202D%20Modeling%20Users%20Manual.pdf*

Buchanan RA, Skalski JR, Brandes PL, Fuller A. 2013. Route use and survival of juvenile Chinook salmon through the San Joaquin River Delta. N Amer J Fish Mgmt [Internet]. [cited 2018 March 16];33(1):216-29. Available from: *http://onlinelibrary.wiley.com/doi/10.1080/02755947.2012.728178/full* *https://doi.org/10.1080/02755947.2012.728178*

Burke JF. [Internet]. c2012. lowess; [updated 2012 June 18; cited 2018 March 17]. Available from: *https://www.mathworks.com/matlabcentral/fileexchange/22470-lowess--locally-weighted-scatterplot-smoothing-for-linear-and-non-linear-data--enhanced-*

Buschman FA, Hoitink AJF, van der Vegt M, Hoekstra P. 2010. Subtidal flow division at a shallow tidal junction. Water Resour Res [Internet]. [cited 2017 April 6];46(12). Available from: *http://onlinelibrary.wiley.com.oca.ucsc.edu/doi/10.1029/2010WR009266/full* *https://doi.org/10.1029/2010WR009266*

Casulli V. 2009. A high-resolution wetting and drying algorithm for free-surface hydrodynamics. Int J Numer Meth Fluid [Internet]. [cited 2017 July 17];60(4):391-408. Available from: *http://onlinelibrary.wiley.com/doi/10.1002/fld.1896/full* *https://doi.org/10.1002/fld.1896*

Cavallo B, Gaskill P, Melgo J, Zeug SC. 2015. Predicting juvenile Chinook salmon routing in riverine and tidal channels of a freshwater estuary. Environ Biol Fish [Internet]. [cited 2017 April 6];90(6):1571-1582. Available from: *https://link-springer-com.oca.ucsc.edu/article/10.1007/s10641-015-0383-7* *https://doi.org/10.1007/s10641-015-0383-7*

CCWD: Contra Costa Water District [Internet]. c2018. Concord (CA): The source of your water; [cited 2018 March 30]. Available from: *https://www.ccwater.com/365/The-Source-of-Your-Water*

CDEC: California Data Exchange Center [Internet]. c2016. Sacramento (CA): USGS flow and stage data; [updated 2017 April 6; cited 2017 April 6]. Available from: *http://cdec.water.ca.gov/*

CH2M Hill. 2009. DSM2 recalibration. Sacramento (CA): Technical Report Prepared for the Department of Water Resources California [Internet]. [cited 2018 January 20]; 236 p. Available from: *http://baydeltaoffice.water.ca.gov/downloads/DSM2_Users_Group/BDCP/DSM2_Recalibration_102709_doc.pdf*

Chao Y, Farrara JD, Zhang H, Zhang YJ, Ateljevich E, Chai F, Davis CO, Dugdale R, Wilkerson F. 2017. Development, implementation, and validation of a modeling system for the San Francisco Bay and Estuary. Estuary Coast Shelf Sci [Internet]. [cited 2017 July 14];194:40-56. Available from: *http://www.sciencedirect.com/science/article/pii/S0272771416303924*
https://doi.org/10.1016/j.ecss.2017.06.005

Chen X. 2005. A comparison of hydrostatic and nonhydrostatic pressure components in seiche oscillations. Math Comp Model [Internet]. [cited 2017 April 6];41:887-902. Available from: *http://www.sciencedirect.com.oca.ucsc.edu/science/article/pii/S0895717705001512*
https://doi.org/10.1016/j.mcm.2004.08.005

Cleveland WS. 1979. Robust locally weighted regression and smoothing scatterplots. J Amer Stat Assoc [Internet]. [cited 2018 March 17];74(368):829-36. Available from: *https://amstat.tandfonline.com/doi/abs/10.1080/01621459.1979.10481038*
https://doi.org/10.1080/01621459.1979.10481038

Cloern JE. 2007. Habitat connectivity and ecosystem productivity: implications from a simple model. Amer Natural [Internet]. [cited 2017 April 6];169(1):E21-E33. Available from: *http://www.journals.uchicago.edu.oca.ucsc.edu/doi/abs/10.1086/510258*
https://doi.org/10.1086/510258

Curran PJ. 1988. The semivariogram in remote sensing: an introduction. Remote Sens Environ. 1988 [Internet]. [cited 2018 February 7];24(3):493-507. Available from: *https://www.sciencedirect.com/science/article/pii/0034425788900211*
https://doi.org/10.1016/0034-4257(88)90021-1

D'alpaos L, Defina A. 2007. Mathematical modeling of tidal hydrodynamics in shallow lagoons: a review of open issues and applications to the Venice lagoon. Comp Geosci [Internet], [cited 2017 April 6];33(4):476-496. Available from: *http://www.sciencedirect.com.oca.ucsc.edu/science/article/pii/S0098300406001476*
http://doi.org/10.1016/j.cageo.2006.07.009

Dawson C, Westerink JJ, Feyen JC, Pothina D. 2006. Continuous, discontinuous and coupled-discontinuous Galerkin finite element methods for the shallow water equations. Int J Numer Meth Fluid [Internet]. [cited 2017 April 6];52:63-88. Available from: *http://onlinelibrary.wiley.com.oca.ucsc.edu/doi/10.1002/fld.1156/full*
https://doi.org/10.1002/fld.1156

DeLong LL, Lewis L, Thompson DB, Lee JK. 1997. The computer program FourPt (Version 95.01): A model for simulating one-dimensional, unsteady, open-channel flow. Branch of Information Services: United States Geological Survey. Water-Resources Investigation Report 97-4016. [Internet]. [cited 2017 April 6]; 67 p. Available from: *https://pubs.er.usgs.gov/publication/wri974016*

de Brye B, de Brauwere A, Gourgue O, Kärnä T, Lambrechts J, Comblen R, Deleersnijder E. 2010. A finite-element multi-scale model of the Scheldt tributaries, river estuary and ROFI. Coast Engr [Internet]. [cited 2017 April 6];57(9):850-863. Available from: *http://www.sciencedirect.com.oca.ucsc.edu/science/article/pii/S0378383910000487*
http://doi.org/10.1016/j.coastaleng.2010.04.001

CDWR: California Department of Water Resources [Internet]. c2011. Sacramento (CA): 1998-2003 calibration and validation; [updated 2011 March 29; cited 2018 January 20]. Available from: *http://www.water.ca.gov/DSM2pwt/calibrate/index.cfm*

CDWR: California Department of Water Resources [Internet]. c2014. Sacramento (CA): DSM2 user group portal: DSM2 v8.1.2 calibration; [updated 2014 April 15; cited 2018 January 19]. Available from: *https://DSM2ug.water.ca.gov/library/-/document_library/view/163187*

CDWR: California Department of Water Resources [Internet]. c2016. Sacramento (CA): DAYFLOW program; [updated 2016 December 30; cited 2017 April 6]. Available from: *http://www.water.ca.gov/dayflow/output/Output.cfm*

CDWR: California Department of Water Resources [Internet]. c2017. Sacramento (CA): California cooperative snow surveys; [updated 2017 March 21; cited 2018 January 19]. Available from: *http://cdec.water.ca.gov/cgi-progs/iodir/WSIHIST*

https://doi.org/10.15447/sfews.2018v16iss2art6

CDWR: California Department of Water Resources [Internet]. c2018. Sacramento (CA): Suisun Marsh program: Suisun Marsh salinity control gate operation schedule; [updated 2018 January 19; cited 2018 January 19]. Available from: *http://www.water.ca.gov/suisun/dataReports/docs/histsmscgopnew.pdf*

Ehle B. 1969. On Padé approximations to the exponential function and A-stable methods for the numerical solution of initial value problems [Dissertation]. [Waterloo (Canada)]: University of Waterloo. p. 1-125.

Ferreira I, Sandhu N. 2016. DSM2 extension: a GIS based approach. In: Methodology for flow and salinity estimates in the Sacramento-San Joaquin Delta and Suisun Marsh. Sacramento (CA): California Department of Water Resources, Office of State Water Project Planning, Modeling Support Branch, Delta Modeling Section. 37th Annual Progress Report to the State Water Resources Control Board. p. 35-54.

Ferziger J, Perić M. 1997. Computational methods for Fluid Mechanics. 2nd Ed. Berlin (Germany): Springer. p. 1-403.

Feyrer F, Healey, MP. 2003. Fish community structure and environmental correlates in the highly altered southern Sacramento-San Joaquin Delta. Environ Biol Fish [Internet];66(2):123-132. [cited 2018 January 30]. Available from: *https://link.springer.com/article/10.1023/A:1023670404997*
https://doi.org/https://doi.org/10.1023/A:1023670404997

Fischer HB, List EJ, Koh RCY, Imberger J, Brooks NH. 1979. Mixing in inland and coastal waters. New York (NY): Academic Press. p. 1-483.

Fleenor W, Bennett W, Moyle P, Lund J. 2010. On developing prescriptions for freshwater flows to sustain desirable fishes in the Sacramento-San Joaquin Delta. Davis (CA): Delta Solutions, Center for Watershed Sciences, University of California, Davis. Report submitted to the State Water Resources Control Board regarding flow criteria for the Delta necessary to protect public trust resources [Internet]. [cited 2017 April 07]; 143 p. Available from: *https://pdfs.semanticscholar.org/9249/e519b0ea07b72146ce16e324d26ff25045b8.pdf?_ga=1.222758235.15681393.1491578629*

Fleenor WE, Bombardelli FA. 2013. Simplified 1-D hydrodynamic and salinity transport modeling of the Sacramento-San Joaquin Delta: sea level rise and water diversion effects. San Franc Estuary Watershed Sci [Internet]. [cited 2018 February 14];11:4. Available from: *https://escholarship.org/uc/item/3km0d0kt*

Fong DA, Monismith SG, Stacey MT, Burau JR. 2009. Turbulent stresses and secondary currents in a tidal-forced channel with significant curvature and asymmetric bed forms. J Hydraul Engr [Internet]. [cited 2017 April 7];135(3):198-208. Available from: *http://ascelibrary.org.oca.ucsc.edu/doi/abs/10.1061/(ASCE)0733-9429(2009)135:3(198)*
https://doi.org.oca.ucsc.edu/10.1061/(ASCE)0733-9429(2009)135:3(198)#sthash.4HqufeWd.dpuf

Freidrichs CT, Aubrey DG. 1994. Tidal propagation in strongly convergent channels. J Geophys Res [Interne]. [cited 2017 April 7];99(C2):3321-3336. Available from: *http://onlinelibrary.wiley.com/doi/10.1029/93JC03219/full*
https://doi.org/10.1029/93JC03219

Fringer OB, McWilliams J, Street R. 2006. A new hybrid model for coastal simulations. Oceanogr [Internet]. [cited 2017 April 07];19:64-77. Available from: *http://tos.org/oceanography/article/a-new-hybrid-model-for-coastal-simulations*
https://doi.org/10.5670/oceanog.2006.91

Galland J-C, Goutal N, Hervouet JM. 1991. TELEMAC: A new numerical model for solving shallow water equations. Adv Water Resour [Internet]. [cited 2018 January 22];14(3):138-148. Available from: *http://www.sciencedirect.com/science/article/pii/030917089190006A*
https://doi.org/10.1016/0309-1708(91)90006-A

Ganju NK, Brush MJ, Rashleigh B, Aretxabaleta AL, Del Barrio P, Grear JS, Harris LA, Lake SJ, McCardell G, O'Donnell J, Ralston DK. 2016. Progress and challenges in coupled hydrodynamic-ecological estuarine modeling. Estuary Coast [Internet]. [cited: 2018 February 7];39(2):311-32. Available from: *https://link.springer.com/article/10.1007/s12237-015-0011-y*
https://doi.org/10.1007/s12237-015-0011-y

Garcia R, Kahawita RA. 1986. Numerical solution of the St. Vénant equations with the MacCormack finite-difference scheme. Int J Numer Meth Fluids [Internet]. [cited 2017 April 7];6:259-274. Available from: *http://onlinelibrary.wiley.com.oca.ucsc.edu/doi/10.1002/fld.1650060502/full*
https://doi.org/10.1002/fld.1650060502

Geyer WR, MacCready P. 2014. The estuarine circulation. Annu Rev Fluid Mech [Internet]. [cited 2018 January 22];46:175-197. Available from: *http://www.annualreviews.org/doi/full/10.1146/annurev-fluid-010313-141302*
https://doi.org/10.1146/annurev-fluid-010313-141302

Geyer WR, Trowbridge JH, Bowen MM. 2000. The dynamics of a partially mixed estuary. J Phys Oceanogr [Internet]. [cited 2017 April 7];30:2035-2048. Available from: *http://journals.ametsoc.org.oca.ucsc.edu/doi/abs/10.1175/1520-0485(2000)030%3C2035:TDOAPM%3E2.0.CO%3B2*
https://doi.org/10.1175/1520-0485(2000)030<2035:TDOAPM>2.0.CO;2

Gourgue O, Comblen R, Lambrechts J, Kärnä T, Legat V, Deleersnijder E. 2009. A flux-limiting wetting-drying method for finite-element shallow-water models, with application to the Scheldt Estuary. Adv Water Resour [Internet]. [cited 2017 April 7];32(12):1726-1739. Available from: *http://www.sciencedirect.com/science/article/pii/S0309170809001493*
https://doi.org/10.1016/j.advwatres.2009.09.005

Gross ES, Koseff JR, Monismith, SG. 1999. Three-dimensional salinity simulations of south San Francisco Bay. J Hydraul Engr [Internet]. [cited 2018 January 22];125(11):1199-1209. Available from: *https://ascelibrary.org/doi/abs/10.1061/(ASCE)0733-9429(1999)125:11(1199)*
https://doi.org/10.1061/(ASCE)0733-9429(1999)125:11(1199)

Gross ES, MacWilliams M, Holleman CD, Hervier TA. 2010. POD-3D particle tracking model study. Sacramento (CA): Particle Tracking Model Testing and Applications Report Prepared for Interagency Ecological Program [Internet]. [cited 2018 March 9]; 109 p. Available from: *http://www.science.calwater.ca.gov/pdf/workshops/POD/GrossEtAl_POD3D_Particle_tracking_2010.pdf*

Grotkop G. 1973. Finite element analysis of long-period water waves. Comp Meth Appl Mech Engr [Internet]. [cited 2017 April 7];2:147-157. Available from: *http://www.sciencedirect.com/science/article/pii/0045782573900121*
https://doi.org/10.1016/0045-7825(73)90012-1

Guo L, van der Wegen M, Jay DA, Matte P, Wang, ZB, Roelvink D, He Q. 2015. River-tide dynamics: exploration of nonstationary and nonlinear tidal behavior in the Yangtze River estuary. J Geophys Res: Ocean [Internet]. [cited 2017 April 7];120:3499-3521. Available from: *http://onlinelibrary.wiley.com/doi/10.1002/2014JC010491/full*
https://doi.org/10.1002/2014JC010491

Harader S, Fernandez P, Burau J, Roy S, Larsen K, Li X, Orloff L, Ullrey R, Podger D, Holm L, McCarthy M. 2007. Conceptual model for salinity in the Central Valley and Sacramento-San Joaquin Delta. Sacramento (CA): CALFED Bay-Delta Program, Water Quality Program Report [Internet]. [cited 2018 January 21]; 65 p. Available from: *https://www.waterboards.ca.gov/rwqcb5/water_issues/drinking_water_policy/salinity_conceptual_model/salinity_conceptual_model_july2007_final.pdf*

Holleman RC, Stacey MT. 2014. Coupling of sea level rise, tidal amplification and inundation. J Phys Oceanogr [Internet]. [cited 2017 July 14];44:1439–1455 Available from: *http://journals.ametsoc.org/doi/full/10.1175/JPO-D-13-0214.1*
https://doi.org/10.1175/JPO-D-13-0214.1

Hsu E-C, Ateljevich E, Sandhu P. 2016. Delta salinity simulation with DSM2-GTM. In: Bay-Delta Office. 2016. Methodology for flow and salinity estimates in the Sacramento-San Joaquin Delta and Suisun Marsh. Sacramento (CA): California Department of Water Resources, Office of State Water Project Planning, Modeling Support Branch, Delta Modeling Section. 37th Annual Progress Report to the State Water Resources Control Board. p. 55-94.

Hunter NM, Bates PD, Horritt MS, Wilson MD. 2007. Simple spatially-distributed models for predicting flood inundation: a review. Geomorph [Internet]. [cited 2017 April 7];90(3-4):208-225. Available from: *http://www.sciencedirect.com/science/article/pii/S0169555X07001304*
https://doi.org/10.1016/j.geomorph.2006.10.021

Hutton P. 1995. Introduction. In: Methodology for flow and salinity estimates in the Sacramento-San Joaquin Delta and Suisun Marsh. Sacramento (CA): California Department of Water Resources, Office of State Water Project Planning, Modeling Support Branch, Delta Modeling Section. 16th Annual Progress Report to the State Water Resources Control Board. p. 6-9.

https://doi.org/10.15447/sfews.2018v16iss2art6

Israeli M. 1981. Approximation of radiation boundary conditions. J Comp Phys [Internet]. [cited 2017 April 7];41:115-135. Available from: *http://www.sciencedirect.com/science/article/pii/0021999181900826* *https://doi.org/10.1016/0021-9991(81)90082-6*

Jobson HE, Schoellhamer DH. 1993. Users manual for a branched Lagrangian transport model. Reston (VA): United States Geological Survey, Books and Open-File Reports 87-4163 [Internet]. cited 2018 January 18]; 86 p. Available from: *https://pubs.usgs.gov/wri/1987/4163/report.pdf*

Jarrett RD. 1984. Hydraulics of high-gradient streams. Journal of Hydraulic Engineering, [Internet]. [cited 2017 April 7];110(11):1519-1539. Available from: *http://ascelibrary.org/doi/abs/10.1061/(ASCE)0733-9429(1984)110:11(1519)* *https://doi.org/10.1061/(ASCE)0733-9429(1984)110:11(1519)#sthash.kPHpLA1v.dpuf*

Jassby AD, Kimmerer WJ, Monismith SG, Armor C, Cloern JE, Powell, TM, Schubel JR, Vendlinski TJ. 1995. Isohaline position as a habitat indicator for estuarine populations. Ecol Appl [Internet]. [cited 2017 April 7];5(1):272-289. Available from: *http://onlinelibrary.wiley.com/doi/10.2307/1942069/full* *https://doi.org/10.2307/1942069*

Jolliff JK, Kindle JC, Shulman I, Penta B, Friedrichs MA, Helber R, Arnone RA. 2009. Summary diagrams for coupled hydrodynamic-ecosystem model skill assessment. J Mar Sys [Internet]. [cited: 6 February 2018];76(1-2):64-82. Available from: *https://www.sciencedirect.com/science/article/pii/S0924796308001140* *https://doi.org/10.1016/j.jmarsys.2008.05.014*

Kadir T. 2006. Estimates for consumptive water demands in the Delta using DETAW. In: Bay-Delta Office. 2006. Methodology for flow and salinity estimates in the Sacramento-San Joaquin Delta and Suisun Marsh. Sacramento (CA): California Department of Water Resources. Annual Progress Report to the State Water Resources Control Board 27. p. 79-90.

Kimmerer WJ. 2004. Open water processes of the San Francisco Estuary: from physical forcing to biological responses. San Franc Estuary Watershed Sci [Internet]. [cited 2017 April 7];2(1). Available from: *http://escholarship.org/uc/item/9bp499mv* *https://doi.org/10.15447/sfews.2004v2iss1art1*

Kimmerer WJ. 2008. Losses of Sacramento River Chinook Salmon and Delta Smelt to entrainment in water diversions in the Sacramento-San Joaquin Delta. San Franc Estuary Watershed Sci [Internet]. [cited 2017 April 7];6(2). Available from: *http://escholarship.org/uc/item/7v92h6fs* *https://doi.org/10.15447/sfews.2008v6iss2art2*

Kimmerer WJ. 2011. Modeling Delta Smelt losses at the South Delta export facilities. San Franc Estuary Watershed Sci [Internet]. [cited 2018 February 23];9(1). Available from: *https://escholarship.org/uc/item/0rd2n5vb* *https://doi.org/10.15447/sfews.2011v9iss1art3*

Kimmerer WJ, Nobriga ML. 2008. Investigating particle transport and fate in the Sacramento-San Joaquin Delta using a particle tracking model. San Franc Estuary Watershed Sci [Internet]. [cited 2017 April 7];6(1). Available from: *https://escholarship.org/uc/item/547917gn#* *https://doi.org/10.15447/sfews.2008v6iss1art4*

Kolar RL, Westerink JJ, Kantekin ME, Blain CA. 1994. Aspects of nonlinear simulations using shallow-water models based on the wave continuity equation. Comp Fluid [Internet]. [cited 2017 April 7];23(3):523-538. Available from: *http://www.sciencedirect.com/science/article/pii/0045793094900175* *https://doi.org/10.1016/0045-7930(94)90017-5*

Kowalik Z, Proshutinsky AY. 1993. Diurnal tides in the Arctic Ocean. J Geophys Res [Internet]. [cited 2017 April 7];98(C9):16449-16468. Available from: *http://onlinelibrary.wiley.com/doi/10.1029/93JC01363/full* *https://doi.org/10.1029/93JC01363*

Kukulka T, Jay DA. 2003. Impacts of Columbia River discharges on salmonid habitat: a nonstationary fluvial tidal model. J Geophs Res [Internet]. [cited 2018 February 3];108(C9), 3293. Available from: *http://onlinelibrary.wiley.com/doi/10.1029/2003JC001829/full* *https://doi.org/10.1029/2003JC001829*

Kundu PK, Cohen IM. 2002. Fluid Mechanics. San Diego (CA): Academic Press. p. 1-730.

Lai Y. 2009. SRH-2D: Two-dimensional depth-averaged flow modeling with an unstructured hybrid mesh. Denver (CO): United States Bureau of Reclamation, Technical Service Center. Theory Paper [Internet]. [cited 2018 February 23]; 40 p. Available from: *https://www.usbr.gov/tsc/techreferences/computer%20software/models/srh2d/downloads/Theory_Paper-SRH2D-v2-2009.pdf*

Levesque L, Murty TS, El-Sabh MI. 1979. Numerical modeling of tidal propagation in the St. Lawrence estuary. Int Hydrogr Rev [Internet]. [cited 2017 April 7];2:117-132. Available from: *https://journals.lib.unb.ca/index.php/ihr/article/view/23645*

Liang L, Liu S, Suits R. 2011. South Delta temporary barrier hydrodynamic modeling. In: Bay-Delta Office. 2011. Methodology for flow and salinity estimates in the Sacramento-San Joaquin Delta and Suisun Marsh. Sacramento (CA): California Department of Water Resources, Office of State Water Project Planning, Modeling Support Branch, Delta Modeling Section. 32nd Annual Progress Report to the State Water Resources Control Board. p. 69-106.

Liu L, Ateljevich E. 2011. Improvements to the DSM2-Qual: part 1. In: Bay-Delta Office. 2011. Methodology for flow and salinity estimates in the Sacramento-San Joaquin Delta and Suisun Marsh. Sacramento (CA): California Department of Water Resources, Office of State Water Project Planning, Modeling Support Branch, Delta Modeling Section. 32nd Annual Progress Report to the State Water Resources Control Board. p. 19-40.

Liu L, Ateljevich E, Sandhu P. 2012. Improved geometry interpolation in DSM2-Hydro. In: Bay-Delta Office. 2012. Methodology for flow and salinity estimates in the Sacramento-San Joaquin Delta and Suisun Marsh. Sacramento (CA): California Department of Water Resources, Office of State Water Project Planning, Modeling Support Branch, Delta Modeling Section. 33rd Annual Progress Report to the State Water Resources Control Board. p. 31-42.

Liu L, Sandhu P. 2012. DSM2 version 8.1 recalibration. In: Bay-Delta Office. 2012. Methodology for flow and salinity estimates in the Sacramento-San Joaquin Delta and Suisun Marsh. Sacramento (CA): California Department of Water Resources, Office of State Water Project Planning, Modeling Support Branch, Delta Modeling Section. 33nd Annual Progress Report to the State Water Resources Control Board. p. 43-70.

Liu L, Sandhu P. 2013. DSM2 version 8.1 recalibration with NAVD88 datum. In: Bay-Delta Office. 2013. Methodology for flow and salinity estimates in the Sacramento-San Joaquin Delta and Suisun Marsh. Sacramento (CA): California Department of Water Resources, Office of State Water Project Planning, Modeling Support Branch, Delta Modeling Section. 34nd Annual Progress Report to the State Water Resources Control Board. p. 73-106.

Liu L, Sandhu P. 2014. DSM2 version 8.1 time step sensitivity test. In: Bay-Delta Office. 2013. Methodology for flow and salinity estimates in the Sacramento-San Joaquin Delta and Suisun Marsh. Sacramento (CA): California Department of Water Resources, Office of State Water Project Planning, Modeling Support Branch, Delta Modeling Section. 35nd Annual Progress Report to the State Water Resources Control Board. p. 35-52.

Longuet-Higgins M. 1969. On the transport of mass by time-varying ocean currents. Deep Sea Res [Internet]. [cited 2017 April 7];16:431-447. Available from: *http://www.sciencedirect.com/science/article/pii/001174716990031X*
https://doi.org/10.1016/0011-7471(69)90031-X

Louaked M, Hanich L. 1998. TVD scheme for the shallow water equations. J Hydraul Res [Internet]. [cited 2017 April 7];36(3):363-378. Available from: *http://www.tandfonline.com/doi/abs/10.1080/00221689809498624*
https://doi.org/10.1080/00221689809498624

Lucas LV, Cloern JE, Thompson JK, Monsen NE. 2002. Functional variability of habitats within the Sacramento–San Joaquin Delta: restoration implications. Ecol Appl [Internet]. [cited 2018 January 30];12(5):1528-47. Available from: *http://onlinelibrary.wiley.com/doi/10.1890/1051-0761(2002)012[1528:FVOHWT]2.0.CO;2/full*
https://doi.org/10.1890/1051-0761(2002)012[1528:FVOHWT]2.0.CO;2

Luoma SN, Dahm CN, Healey M, Moore JN. 2015. Challenges facing the Sacramento–San Joaquin Delta: complex, chaotic, or simply cantankerous? San Franc Estuary Watershed Sci [Internet]. [cited 2018 March 31];13(3). Available from: *https://escholarship.org/uc/item/3nd0r71d*
https://doi.org/10.15447/sfews.2015v13iss3art7

https://doi.org/10.15447/sfews.2018v16iss2art6

Ma Q, Chen F, Wang Y. 2011. Research on water pollution problem of Liangtanhe Basin based on MIKE 11 Ecolab model. Water Resour Power [Internet]. [cited 2018 January 20];29:33-36. Available from: *http://en.cnki.com.cn/Article_en/CJFDTOTAL-SDNY201111008.htm*

MacCready P. 1999. Estuarine adjustment to changes in river flow and tidal mixing. J Phys Oceanogr [Internet]. [cited 2018 March 14];29(4):708-726. Available from: *https://journals.ametsoc.org/doi/full/10.1175/1520-0485(1999)029%3C0708:EATCIR%3E2.0.CO%3B2 https://doi.org/10.1175/1520-0485(1999)029<0708:EATCIR>2.0.CO;2*

MacCready P. 2004. Toward a unified theory of tidally-averaged estuarine salinity structure. Estuary Coast. [Internet]. [cited 2018 February 14];27(4):561-70. Available from: *https://link.springer.com/article/10.1007/BF02907644 https://doi.org/https://doi.org/10.1007/BF02907644*

MacCready P, Geyer WR. 2010. Advances in estuarine physics. Annu Rev Mar Sci [Internet]. [cited: 2018 January 23];2:35-58. Available from: *http://www.annualreviews.org/doi/full/10.1146/annurev-marine-120308-081015 https://doi.org/https://doi.org/10.1146/annurev-marine-120308-081015*

MacWilliams ML, Bever AJ, Gross ES, Ketefian GS, Kimmerer WJ. 2015. Three-dimensional modeling of hydrodynamics and salinity in the San Francisco estuary: An evaluation of model accuracy, X2, and the low–salinity zone. San Franc Estuary Watershed Sci [Internet]. [cited 2017 July 14];13(1). Available from: *http://escholarship.org/uc/item/7x65r0tf https://doi.org/10.15447/sfews.2015v13iss1art2*

Martyr-Koller RC, Kernkamp HWJ, van Dam A, van der Wegen M, Lucas LV, Knowles N, Jaffe B, Fregoso TA. 2017. Application of an unstructured 3D finite volume numerical model to flows and salinity dynamics in the San Francisco Bay-Delta. Estuary Coast Shelf Sci [Internet]. [cited 2017 July 14];192:86-107. Available from: *http://www.sciencedirect.com/science/article/pii/S0272771416307120 https://doi.org/10.1016/j.ecss.2017.04.024*

The Mathworks Inc. 2016. Natick (MA): MATLAB and Statistics Toolbox Release 2016b.

Matte P, Jay DA, Zaron ED. 2013. Adaptation of classical tidal harmonic analysis to nonstationary tides, with applications to river tides. J Atmos Ocean Tech [Internet]. [cited 2017 April 7];30:569-589. Available from: *http://journals.ametsoc.org/doi/abs/10.1175/JTECH-D-12-00016.1 https://doi.org/10.1175/JTECH-D-12-00016.1*

Moftakhari HR, Jay DA, Talke SA, Kukulka T, Bromirski PD. 2013. A novel approach to flow estimation in tidal rivers. Water Resour Res [Internet]. [cited 2017 April 7];49(8):4817-4832. Available from: *http://onlinelibrary.wiley.com/doi/10.1002/wrcr.20363/full https://doi.org/10.1002/wrcr.20363*

Monismith SG. 2016. A note on Delta Outflow. San Franc Estuary Watershed Sci [Internet]. [cited 2017 April 7];14(3). Available from: *http://escholarship.org/uc/item/89k7b61m https://doi.org/10.15447/sfews_2016v14iss3art3*

Monismith SG, Hench JL, Fong DA, Nidzieko NJ, Fleenor WE, Doyle LP, Schadow SG. 2009. Thermal variability in a tidal river. Estuary Coasts [Internet]. [cited 2017 April 7];32:100-110. Available from: *https://link.springer.com/article/10.1007/s12237-008-9109-9 https://doi.org/10.1007/s12237-008-9109-9*

Monismith SG, Kimmerer W, Burau JR, Stacey MT. 2002. Structure and flow-induced variability of the subtidal salinity field in northern San Francisco Bay. J Phys Oceanogr [Internet]. [cited 2017 April 7];32(11):3003-3019. Available from: *http://journals.ametsoc.org/doi/abs/10.1175/1520-0485(2002)032%3C3003:SAFIVO%3E2.0.CO%3B2 https://doi.org/10.1175/1520-0485(2002)032<3003:SAFIVO>2.0.CO;2*

Monsen NE. 2000. A study of sub-tidal transport in Suisun Bay and the Sacramento-San Joaquin Delta, California [dissertation]. [Stanford (CA)]: Stanford University. p. 1-343.

Mount J, Twiss R. 2005. Subsidence, sea-level rise and seismicity in the Sacramento-San Joaquin Delta. San Franc Estuary Watershed Sci [Internet]. [cited 2018 January 30];3(1). Available from: *https://escholarship.org/uc/item/4k44725p https://doi.org/10.15447/sfews.2005v3iss1art7*

Nader-Tehrani P. 2001. DSM2 calibration and validation. In: Bay-Delta Office. 2001. Methodology for flow and salinity estimates in the Sacramento-San Joaquin Delta and Suisun Marsh. Sacramento (CA): California Department of Water Resources, Office of State Water Project Planning, Modeling Support Branch, Delta Modeling Section. 22nd Annual Progress Report to the State Water Resources Control Board. p. 16-23.

Nelson JM, Bennett JP, Wiele SM. 2003. Flow and Sediment Transport Modeling. In: Kondolph M, Piegay H. editors. 2003. Tools in Fluvial Geomorphology. Hoboken (NJ): Wiley and Sons. p. 539-576.

Newman KB, Brandes PL. 2010. Hierarchical modeling of juvenile Chinook salmon survival as a function of Sacramento–San Joaquin Delta water exports. N Amer J Fish Mgmt [Internet]. [cited 2018 March 16];30(1):157-69. Available from: *https://www.tandfonline.com/doi/abs/10.1577/M07-188.1*
https://doi.org/10.1577/M07-188.1

NGS: National Geodetic Survey [Internet]. c2004. Silver Spring (MD): VERTCON – North American vertical datum conversion. [updated 2017 May 16; cited 2018 January 25]. Available from: *https://www.ngs.noaa.gov/TOOLS/Vertcon/vertcon.html*

Nidzieko NJ. 2010. Tidal asymmetry in estuaries with mixed semidiurnal/diurnal tides. J Geophys Res: Ocean, [Internet]. [cited 2018 May 7];115(C8). Available from: *https://agupubs.onlinelibrary.wiley.com/doi/full/10.1029/2009JC005864*
https://doi.org/10.1029/2009JC005864

NOAA: National Oceanic and Atmospheric Administration. c2013. San Francisco Bay PORTSTM [Internet]. [updated 2013 October 15; cited 2018 January 27]. Available from: *https://tidesandcurrents.noaa.gov/stationhome.html?id=9415102*

NOAA-TC: National Oceanic and Atmospheric Administration – Tides and Currents [Internet]. c2013. Silver Spring (MD): Observed water levels at Martinez Amorco Pier, California; [updated 2018 January 21; cited 2018 January 21]. Available from: *https://tidesandcurrents.noaa.gov/stationhome.html?id=9415102*

Ohlson JA, Kim S. 2015. Linear valuation without OLS: the Theil-Sen estimation approach. Rev Acct Stu [Internet]. [cited 2018 February 17];20(1):395-435. Available from: *https://link.springer.com/article/10.1007/s11142-014-9300-0*
https://doi.org/10.1007/s11142-014-9300-0

Papanicolaou A, Elhakeem M, Krallis G, Prakash S, Edinger J. 2008. Sediment transport modeling review – current and future developments. J Hydraul Engr [Internet]. [cited 2017 April 7];134(1):1-14. Available from: *http://ascelibrary.org/doi/abs/10.1061/(ASCE)0733-9429(2008)134%3A1(1)*
https://doi.org/10.1061/(ASCE)0733-9429(2008)134:1(1)#sthash.LPe2rv0V.dpuf

Patro S, Chatterjee C, Singh R, Raghuwanshi NS. 2009. Hydrodynamic modeling of a large flood-prone river system in India with limited data. Hydrolog Process [Internet]. [cited 2017 July 17];23(19):2774-2791. Available from: *http://onlinelibrary.wiley.com/doi/10.1002/hyp.7375/full*
https://doi.org/10.1002/hyp.7375

Pawlowicz R, Beardsley B, Lentz S. 2002. Classical tidal harmonic analysis including error estimates in MATLAB using T_TIDE. Comp GeoSci [Internet]. [cited 2017 April 7];28(8):929-937. Available from: *http://www.sciencedirect.com/science/article/pii/S0098300402000134*

Perry RW, Skalski JR, Brandes PL, Sandstrom PT, Klimley AP, Ammann A, MacFarlane B. 2010. Estimating survival and migration route probabilities of juvenile Chinook salmon in the Sacramento–San Joaquin River Delta. N Amer J Fish Mgmt [Internet]. [cited 2018 Macrh 16]; 30(1):142-56. Available from: *http://onlinelibrary.wiley.com/doi/10.1577/M08-200.1/full*
https://doi.org/10.1577/M08-200.1

Perry RW, Brandes PL, Burau JR, Klimley AP, MacFarlane B, Michel C, Skalski JR. 2013. Sensitivity of survival to migration routes used by juvenile Chinook salmon to negotiate the Sacramento-San Joaquin River Delta. Environ Biol Fish [Internet]. [cited 2018 February 14];96(2-3):381-92. Available from: *https://link.springer.com/article/10.1007/s10641-012-9984-6*
https://doi.org/https://doi.org/10.1007/s10641-012-9984-6

https://doi.org/10.15447/sfews.2018v16iss2art6

Perry RW, Brandes PL, Burau JR, Sandstrom PT, Skalski JR. 2015. Effect of tides, river flow, and gate operations on entrainment of juvenile salmon into the interior Sacramento–San Joaquin River Delta. Trans Amer Fish Soc [Internet]. [cited 2018 February 14];144(3):445-55. Available from: *http://onlinelibrary.wiley.com.oca.ucsc.edu/doi/10.1080/00028487.2014.1001038/full*
https://doi.org/10.1080/00028487.2014.1001038

Ralston DK, Stacey MT. 2005. Longitudinal dispersion and lateral circulation in the intertidal zone. J Geophys Res: Oceans. [Internet]. [cited 2018 January 30];110(C7):C0715. Available from: *http://onlinelibrary.wiley.com.oca.ucsc.edu/doi/10.1029/2005JC002888/full*
https://doi.org/10.1029/2005JC002888

Ralston DK, Geyer WR, Lerczak JA. 2008. Subtidal salinity and velocity in the Hudson River estuary: Observations and modeling. J Phys Oceanogr [Internet]. [cited 2018 February 14];38(4):753-70. Available from: *https://journals.ametsoc.org/doi/abs/10.1175/2007JPO3808.1*
https://doi.org/10.1175/2007JPO3808.1

Rayson MD, Gross ES, Fringer OB. 2015. Modeling the tidal and sub-tidal hydrodynamics in a shallow, micro-tidal estuary. Ocean Mod [Internet]. [cited 2017 April 7];89:29-44. Available from: *http://www.sciencedirect.com/science/article/pii/S1463500315000207*
https://doi.org/10.1016/j.ocemod.2015.02.002

RMA: Resource Management Associates. 2005. Flooded islands pre-feasibility study: RMA Delta Model calibration report. Fairfield (CA): Report prepared for the California Department of Water Resources for submittal to California Bay–Delta Authority. 158 p. Available from: *http://www.water.ca.gov/frankstract/docs/%288%29RMA-Calibration%20Report.pdf*

RMA: Resource Management Associates. 2013. Lower Sacramento Bypass 2-D model calibration and validation. Sacramento (CA): Draft Technical Memorandum for Task Order No. T10502186-09053 OM. [Internet]. [cited 2018 January 22]; 109 p. Available from: *http://www.water.ca.gov/frankstract/docs/%288%29RMA-Calibration%20Report.pdf*

Ridderinkhof H, Zimmerman JT. 1992. Chaotic stirring in a tidal system. Sci [Internet]. [cited 2018 February 1];258(5085):1107-1111. Available from: *http://science.sciencemag.org/content/258/5085/1107*
https://doi.org/10.1126/science.258.5085.1107

Robson BJ, Hamilton DP, Webster IT, Chan T. 2008. Ten steps applied to development and evaluation of process-based biogeochemical models of estuaries. Environ Model Software [Internet]. [cited: 2018 January 22];23(4):369-384. Available from: *https://scholarsarchive.byu.edu/cgi/viewcontent.cgi?referer=https://scholar.google.com/&httpsredir=1&article=3340&context=iemssconference*

Rose KA, Kimmerer WJ, Edwards KP, Bennett WA. (2013). Individual-based modeling of Delta Smelt population dynamics in the upper San Francisco Estuary: II. Alternative baselines and good versus bad years. Trans Amer Fish Soc [Internet]. [cited 2018 January 20];145(5):1260-1272. Available from: *http://www.ingentaconnect.com/content/tandf/tafs/2013/00000142/00000005/art00009*
https://doi.org/10.1080/00028487.2013.799519

RTC: Romburg Tiburon Center [Internet]. c2017. Tiburon (CA): Carquinez strait buoy data; [updated 2017 October 30; cited 2017 October 30]. Available from: *https://coastwatch.pfeg.noaa.gov/erddap/tabledap/rtcctdCMAysi.mat?time%2Cdepth&time%3E=2009-01-01T00%3A00%3A00Z&time%3C=2016-01-01T00%3A00%3A00Z*

SFBDEP: San Francisco Bay-Delta Evaluation Program. 1998. Methodology for flow and salinity estimates in the Sacramento-San Joaquin Delta and Suisun Marsh. Sacramento (CA): Department of Water Resources. 19th Annual Progress Report [Internet]. [cited 2018 January 20]; 170 p. Available from: *http://baydeltaoffice.water.ca.gov/modeling/deltamodeling/delta/reports/annrpt/1998/1998.pdf*

Sassi MG, Hoitink AJF, de Brye B, Vermuelen B, and Deleersnijder E. 2011. Tidal impact on the division of river discharge over distributary channels in the Mahakam Delta. Ocean Dyn [Internet]. [cited 2017 April 7];61(12):2211-2228. Available from: *https://link.springer.com/article/10.1007/s10236-011-0473-9*
https://doi.org/10.1007/s10236-011-0473-9

Savenije HHG. 2005. Salinity and Tides in Alluvial Estuaries. New York: Elsevier. p. 1-194.

Savenije HHG, Toffolon M, Haas J, Veling EJM. 2008. Analytical description of tidal dynamics in convergent estuaries. J Geophys Res [Internet]. [cited 2017 June 19];113(C10):C10025. Available from: *http://onlinelibrary.wiley.com.oca.ucsc.edu/doi/10.1029/2007JC004408/full* *https://doi.org/10.1029/2007JC004408*

Schoellhamer DH. 2001. Influence of salinity, bottom topography, and tides on locations of estuarine turbidity maxima in northern San Francisco Bay. In: McAnally WH, Mehta AJ, editors. Coastal and estuarine fine sediment transport processes. Elsevier Science B.V. [cited 2018 May 8]; p. 343-357. Available from: *http://ca.water.usgs.gov/abstract/sfbay/elsevier0102.pdf*

SCWA: Solano County Water Agency [Internet]. c2018. Vacaville (CA): North Bay Aqueduct; [cited 2018 March 30]. Available from: *http://www.scwa2.com/water-supply/north-bay-aqueduct*

Sinha P, Pingree RD. 1997. The principal lunar semidiurnal tide and its harmonics: baseline solutions for M2 and M4 constituents on the Northwest European Continental Shelf. Cont Shelf Res [Internet]. [cited 2017 April 7];17(11):1321-1365. Available from: *https://www.infona.pl/resource/bwmeta1.element.elsevier-29b3e0b4-3be4-30cf-88ee-3cd8b72cb104*

Smith LH. 1987. A review of circulation and mixing studies of San Francisco Bay, California. Sacramento (CA): United States Geological Survey. Circular 1015 [Internet]. [cited 2017 April 7]; 46 p. Available from: *https://pubs.usgs.gov/circ/1987/1015/report.pdf*

Smith NP, Stoner AW. 1993. Computer simulations of larval transport through tidal channels: role of vertical migration. Estuary Coast Shelf Sci [Internet]. [cited 2017 April 7];37:43-58. Available from: *http://www.sciencedirect.com/science/article/pii/S0272771483710401* *https://doi.org/10.1006/ecss.1993.1040*

Smith T. 2014. Delta modeling for emergency drought barriers. In: Bay-Delta Office. 2014. Methodology for flow and salinity estimates in the Sacramento-San Joaquin Delta and Suisun Marsh. Sacramento (CA): California Department of Water Resources, Office of State Water Project Planning, Modeling Support Branch, Delta Modeling Section. 35th Annual Progress Report to the State Water Resources Control Board. p. 83-110.

Smith T, Enright C. 1995. Particle Tracking. In: Bay-Delta Office. 1995. In: Bay-Delta Office. 1995. Methodology for flow and salinity estimates in the Sacramento-San Joaquin Delta and Suisun Marsh. Sacramento (CA): California Department of Water Resources, Office of State Water Project Planning, Modeling Support Branch, Delta Modeling Section. 16th Annual Progress Report to the State Water Resources Control Board. p. 54-60.

Simpson J, Brown J, Matthews J, Allen G. 1990. Tidal straining, density currents, and stirring in the control of estuarine stratification. Estuary Coast [Internet]. [cited 2017 April 7];13:125-132. Available from: *https://link.springer.com/article/10.2307%2F1351581?LI=true* *https://doi.org/10.2307/1351581*

Sobey RJ. 2001. Evaluation of numerical models of flood and tide propagation in channels. J Hydraul Engr [Internet]. [cited 2017 April 7];127(10):805-824. Available from: *http://ascelibrary.org/doi/abs/10.1061/(ASCE)0733-9429(2001)127:10(805)* *https://doi.org/10.1061/(ASCE)0733-9429(2001)127:10(805)#sthash.IVMBUNz2.dpuf*

Sommer T, Harrell B, Nobriga M, Brown R, Kimmerer W, Schemel L. 2011. California's Yolo Bypass: evidence that flood control can be compatible with fisheries, wetlands, wildlife, and agriculture. Fisheries [Internet]. [cited 2018 February 23];26(8):6-16. Available from: *http://www.tandfonline.com/doi/abs/10.1577/1548-8446(2001)026%3C0006%3ACYB%3E2.0.CO%3B2* *https://doi.org/10.1577/1548-8446(2001)026<0006:CYB>2.0.CO;2*

Sridharan VK. 2015. Scalar transport in channel networks: development of a particle tracking model to study the movement of scalars in the Sacramento-San Joaquin Delta [dissertation]. [Stanford (CA)]: Stanford University. p. 1-413.

Sridharan VK, Monismith SG, Fong DA, Hench JL, 2018. One-dimensional particle tracking with streamline preserving junctions for flows in channel networks. J Hydraul Engr [Internet]. [cited 2018 February 1];144(2):04017063. Available from: *https://ascelibrary.org/doi/abs/10.1061/%28ASCE%29HY.1943-7900.0001399* *https://doi.org/10.1061/(ASCE)HY.1943-7900.0001399*

Taylor J. 1997. Introduction to error analysis, the study of uncertainties in physical measurements. 1997. Sausalito (CA): University Science Books. p. 1-327.

https://doi.org/10.15447/sfews.2018v16iss2art6

Tu M-Y. 2012. South Delta null zone study. In: Bay-Delta Office. 2012. Methodology for flow and salinity estimates in the Sacramento-San Joaquin Delta and Suisun Marsh. Sacramento (CA): California Department of Water Resources, Office of State Water Project Planning, Modeling Support Branch, Delta Modeling Section. 33nd Annual Progress Report to the State Water Resources Control Board. p. 71-92.

Uncles RJ, Peterson DH. 1996. The long-term salinity field in San Francisco Bay. Continent Shelf Res [Internet]. [cited 2018 January 24];16(15):2005-2039. Available from: *https://www.sciencedirect.com/science/article/pii/0278434396000325*
https://doi.org/10.1016/0278-4343(96)00032-5

USBR: United States Bureau of Reclamation [Internet]. c2018. Sacramento (CA): Central Valley operations: cross channel gate operations historical log; [updated 2018 January 4; cited 2018 January 19]. Available from: *https://www.usbr.gov/mp/cvo/vungvari/Ccgates.pdf*

Walters RA, Tarbotton MR, Hiles CE. 2013. Estimation of tidal power potential. Renew Ener [Internet]. [cited 2017 April 7];51:255-262. Available from: *http://www.sciencedirect.com/science/article/pii/S0960148112005988*
https://doi.org/10.1016/j.renene.2012.09.027

Warner JC, Geyer WR, Lerczak JA. 2005. Numerical modeling of an estuary: A comprehensive skill assessment. J Geophys Res: Oceans [Internet]. [cited 2018 March 9]; 110(C5). Available from: *http://onlinelibrary.wiley.com.oca.ucsc.edu/doi/10.1029/2004JC002691/full*
https://doi.org/10.1029/2004JC002691

Willmott CJ. 1981. On the validation of models. Phys Geograph [Internet]. [cited 2018 February 11];2(2):184-94. Available from: *http://www.tandfonline.com/doi/abs/10.1080/02723646.1981.10642213*
https://doi.org/10.1080/02723646.1981.10642213

Wolfram PJ, Fringer OB. 2013. Mitigating horizontal divergence 'checker-board' oscillations on unstructured triangular C-grids for nonlinear hydrostatic and nonhydrostatic flows. Ocean Mod [Internet]. [cited 2017 April 7];69:64-78. Available from: *http://www.sciencedirect.com/science/article/pii/S1463500313000929*
https://doi.org/10.1016/j.ocemod.2013.05.007

Wright SA, Schoellhamer DH. 2005. Estimating sediment budgets at the interface between rivers and estuaries with application to the Sacramento– San Joaquin River Delta. Water Resour Res [Internet]. [cited 2018 March 16];41(9):W09428. Available from: *http://onlinelibrary.wiley.com/doi/10.1029/2004WR003753/full*
https://doi.org/10.1029/2004WR003753

Wu W, Falconer R, Lin B. 2005. Modeling trace metal concentration distributions in estuarine waters. Estuary Coast Shelf Sci [Internet]. [cited 2017 April 7];64(4):699-709. Available from: *http://www.sciencedirect.com/science/article/pii/S0272771405001320*
https://doi.org/10.1016/j.ecss.2005.04.005

Zou R, Carter S, Shoemaker L, Parker A, Henry T. 2006. Integrated hydrodynamic and water quality modeling system to support nutrient total maximum daily load development for Wissahickon Creek, Pennsylvania. J Environ Engr [Internet]. [cited 2017 April 7];132(4):555-566. Available from: *http://ascelibrary.org/doi/abs/10.1061/(ASCE)0733-9372(2006)132:4(555)*
https://doi.org/10.1061/(ASCE)0733-9372(2006)132:4(555)#sthash.Bmsqryxc.dpuf

Zhong L, Li M. 2006. Tidal energy fluxes and dissipation in the Chesapeake Bay. Cont Shelf Res [Internet]. [cited 2017 April 7];26(6):752-770. Available from: *http://www.sciencedirect.com/science/article/pii/S0278434306000410*
https://doi.org/10.1016/j.csr.2006.02.006

Zhou Y. 2013. DSM2-PTM standard test suite design and automation. In: Bay-Delta Office. 2013. Methodology for flow and salinity estimates in the Sacramento-San Joaquin Delta and Suisun Marsh. Sacramento (CA): California Department of Water Resources, Office of State Water Project Planning, Modeling Support Branch, Delta Modeling Section. 34th Annual Progress Report to the State Water Resources Control Board. p. 141-151.

Zhou Z, Ye Q, Coco G. 2015. A one-dimensional biomorphodynamic model of tidal flats: sediment sorting, marsh distribution, and carbon accumulation under sea level rise. Adv Water Resour [Internet]. [cited 2017 April 7];93:288-302. Available from: *http://adsabs.harvard.edu/abs/2016AdWR...93..288Z*
https://doi.org/10.1016/j.advwatres.2015.10.011

NOTES

1. Ateljevich E. 2018. In-person conversation with VK. Sridharan on salinity data quality in San Francisco Bay-Delta at 9th Street Sacramento, CA.
2. Liang L. 2018. Estimating Delta Channel Depletion by DCD Model. Presented at: Delta Modeling Section Users Group Meeting; Sacramento, CA.
3. Nam K. 2008. Estimation of reduction of export using DSM2 PTM and PEI. Presented at: Fall DSM2 User Group Meeting, Sacramento, CA.
4. Nam K. 2018. SCHISM Frank's Tract restoration feasibility study. Presented at: Delta Modeling Section Users Group Meeting; Sacramento, CA.
5. Sandhu P. 2018. Delta modeling section general activities. Presented at: Delta Modeling Section Users Group Meeting; Sacramento, CA.
6. Sridharan VK. 2018. Matlab toolbox for automatic clean-up of coastal and estuarine tidal datasets. Presented at: Delta Modeling Section Users Group Meeting; Sacramento, CA.
7. Sridharan VK. 2018. Setup files for DSM2 model runs. FORTRAN input (.inp and .dss) files. Located at: 110 McAllister Way, Santa Cruz, CA 95060. Available from: *vamsikrishna.sridharan@ucsc.edu.*

https://doi.org/10.15447/sfews.2018v16iss2art6